NASA-CR-177083
19860019679

A Reproduced Copy

OF

NASA CR- 177,083

Reproduced for NASA

by the

NASA Scientific and Technical Information Facility

NF01704

FFNo 672 Aug 65

College of
Engineering
Iowa State University

N86-29151

RESPONSE OF HOT ELEMENT FLUSH WALL GAUGES

IN OSCILLATING LAMINAR FLOW

Timothy A. Giddings and William J. Cook

February 15, 1986

ISU-ERI-Ames-86435

Final Technical Report (Part 2 of 2 parts)[*] for Grant NCC 2-200
    entitled "Study of Turbulent Boundary Layers in Oscillating Flows"

Grant Period: June 1, 1986 to August 31, 1986

✓ William J. Cook, Principal Investigator

J. D. Murphy, Grant Technical Monitor, NASA Ames Research
    Center, Moffett Field, CA

[*]Part 1: Cook, W. J., "Turbulent Boundary Layers in
        Oscillating Flows: An Experimental and
        Computational Study, " ISU-ERI-Ames-86434,
        February, 1986.

engineering
research institute

iowa state university COLLEGE OF ENGINEERING, AMES, IOWA, 50011
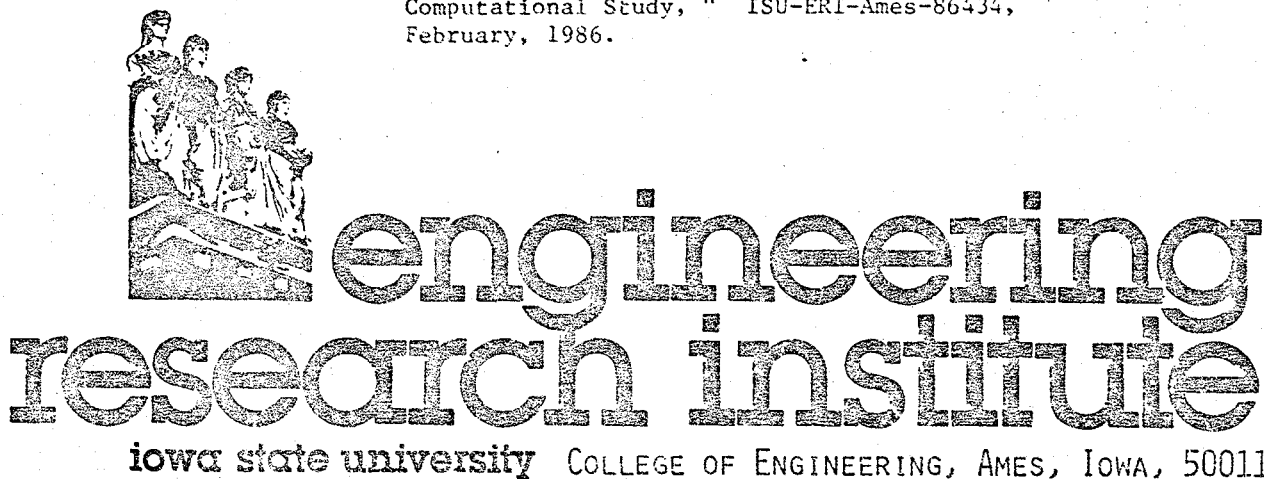
ABSTRACT

An investigation of the time-dependent response characteristics of flush-mounted hot element gauges used as instruments to measure wall shear stress in unsteady periodic air flows is reported. The study was initiated because anomalous results have been obtained from the gauges in oscillating turbulent flows for the phase relation of the wall shear stress variation, indicating possible gauge response problems. An experimental investigation was carried out for flat plate laminar oscillating flows characterized by a mean free stream velocity with a superposed sinusoidal variation. Laminar rather than turbulent flows were studied, because a numerical solution for the phase angle ϕ_τ between the free stream velocity and the wall shear stress variation that is known to be correct can be obtained. Gauges with elements of two types were mounted flush with the surface of the flat plate and tested over a wide range of reduced frequency $\bar{\omega} = \omega x/U_o$. The two element types were a thin platinum film deposited on a quartz substrate and a small diameter wire buried flush with the surface of a polystyrene substrate. The study focused on comparing ϕ_τ indicated by the hot element gauges with corresponding numerical predictions for ϕ_τ, since agreement would indicate that the hot element gauges faithfully follow the true wall shear stress variation.

An experimental study of velocity variation in the laminar oscillating flows generated was carried out by means of hot wire anemometry to verify that the boundary layer flows behaved as predicted by the numerical method. Good agreement was obtained. Hot element gauges were tested with the long dimension of the element perpendicular to the flow for a range of operating resistance ratio, ORR, defined as the ratio of hot element resistance during operation to its resistance at room temperature. In the range $1 < ORR \leq 1.15$, measured values for ϕ_τ were found to depend on $\bar{\omega}$, ORR, and the type of element. For $1.15 < ORR \leq 1.30$ there was no significant influence of ORR. Comparisons of ϕ_τ measured at ORR = 1.30 with the corresponding predicted ϕ_τ revealed that for the platinum film gauges, the experimental variation of the wall shear stress lagged the predicted variation by values ranging from $6\pm$ degrees at $\bar{\omega} = 0.2$ to 16 ± 3 degrees at $\bar{\omega} = 2.4$. (Predicted values for ϕ_τ ranged from zero at $\bar{\omega} = 0$ to near 40 degrees at $\bar{\omega} = 2.4$.) The flush wire gauges were studied for $0.14 \leq \bar{\omega} < 0.9$. Similar comparisons showed that the experimental wall shear stress lagged the predicted value by 14 ± 4 degrees in the noted $\bar{\omega}$ range. Thus, the conclusion is reached that the hot element gauges do not faithfully follow the wall shear stress variation in laminar oscillating flows. There is a significant time lag in the variation indicated by the gauges that depends on $\bar{\omega}$ and the gauge type. The results of this study strongly suggest that time lag in gauge response will also occur for turbulent oscillating flows.

TABLE OF CONTENTS

NOMENCLATURE

b_1 rate of decrease of freestream velocity with distance from leading edge, Equation (8)

f frequency, Hz

ORR   operating resistance ratio = R/R_f

p static pressure

Re_x Reynolds number based on x, $U_o x/\nu$

t time

u x component of boundary layer velocity

U freestream velocity

$\tilde{U}$ variation of the freestream velocity, Equation (1)

v y component of boundary layer velocity

x distance measured from the plate leading edge parallel to the flow direction

y distance measured perpendicular to the plate surface

β pressure gradient parameter for laminar steady flow, Equation (10)

δ boundary layer thickness

δ^* boundary layer displacement thickness

η dimensionless normal distance from the plate surface, $y\sqrt{U_o/\nu x}$

ν kinematic viscosity

ξ dimensionless pressure gradient term, $b_1 x/U_o$, Equation (8)

ρ density

τ surface shear stress

ϕ phase angle

$\Delta\phi_\tau$ difference between two shear stress phase angles

ω angular frequency, rad/s

$\bar{\omega}$ Strouhal number, $\omega x/U_o$

Subscripts:

o   mean value

1   variation

e   experimental quantity

n   numerical quantity

u   velocity quantity

τ shear stress quantity

I. INTRODUCTION

The capability of understanding and predicting the boundary layer behavior in response to an oscillating or periodic flow is important in a number of areas of fluid mechanics. Two of these areas are turbomachinery flow and flow over helicopter rotor blades. A complete boundary layer description would include the time-dependent velocity variation in the boundary layer and the time-dependent wall shear stress variation as functions of position on the surface. Flows in the areas mentioned are very complex and as a result several unsteady boundary layer studies have been conducted that deal with incompressible oscillating flows over plane surfaces as a first step in developing an understanding of their behavior.

A typical description of the freestream flow for such studies is expressed as

$$U(x,t) = U_o(x) + \tilde{U}(x,t)$$
$$= U_o(x) + U_1(x) \cos \omega t$$

(1)

where $U_o(x)$ is the average velocity, $\tilde{U}(x,t)$ is the fluctuating velocity, $U_1(x)$ is the half amplitude of the velocity variation, and ω is the angular frequency of oscillation.

The time-dependent freestream velocity generates an unsteady pressure gradient which, at a given x, varies sinusoidally. When U_o and U_1 in Equation (1) are independent of x, the pressure gradient leads the freestream velocity variation by a phase angle of $\pi/2$ [1,2,3]. The

phase relationship between the freestream velocity variation and the unsteady pressure gradient for this case is shown in Figure 1 with the freestream velocity variation and the pressure gradient represented by rotating vectors. Since the unsteady pressure gradient does not coincide with the freestream velocity, a phase difference is created between the freestream velocity and the slower velocity in the boundary layer. Lighthill [3] has shown for laminar boundary layers that this pressure gradient produces a velocity phase lead relative to the freestream velocity in the inner part of the boundary layer and a phase lag in the outer part of the boundary layer. The ensemble averaged velocity (defined as the average of instantaneous velocity values at the same point in the cycle over a specified number of cycles) in the boundary layer at a specified x location is given by

$$u(y,t) = u_o(y) + u_1(y) \cos [\omega t + \phi_u(y)] \tag{2}$$

where y is the distance perpendicular to the wall, $u_o(y)$ is the mean velocity, $u_1(y)$ is the half amplitude of the velocity variation, and $\phi_u(y)$ is the velocity phase angle relative to the freestream velocity. A positive ϕ_u corresponds to a phase lead. This is illustrated in Figure 2 which shows at fixed values of x and y the velocity variation in the freestream, Equation (1), and in the boundary layer, Equation (2). The velocity variation in the boundary layer shown in Figure 2 leads that in the freestream, but at other values of y, the boundary layer velocity variation may lag that in the freestream.
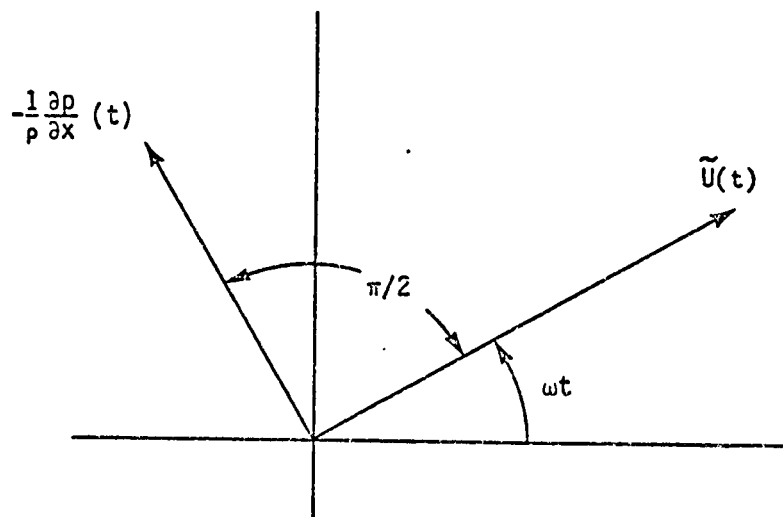
FIGURE 1. Phase relationship between the unsteady pressure gradient and the freestream velocity variation in Equation (1) with U_o and U_1 independent of x
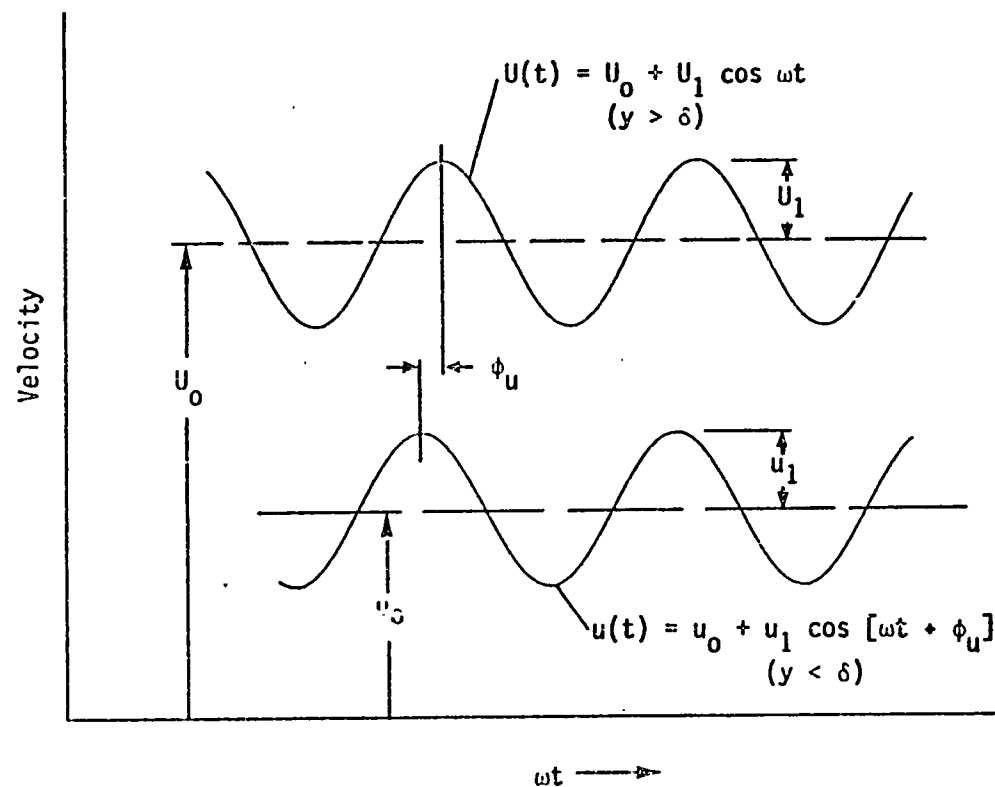
FIGURE 2. Description of the velocity variation in the freestream and in the boundary layer

As noted in Equation 2, the boundary layer quantities u_o, u_1, and ϕ_u vary with y. In turbulent flows, the behavior of u_o, u_1, and ϕ_u are fairly well-understood for most of the boundary layer. However, there is uncertainty about the boundary layer behavior near the wall, particularly with regard to the phase angle ϕ_u. While the velocity phase angle in the outer part of the boundary layer can be experimentally measured, accurate measurement of the phase angle very near the wall is quite difficult by means of conventional hot wire and laser (LDV) systems because of physical limitations related to probe size.

In turbulent flow, direct theoretical prediction of the phase angle is very difficult, so numerical and other techniques must be employed. Cousteix et al. [4] have attacked this problem using a small perturbation development with complex notation for solving the turbulent flow very near the wall. With this method, they claim to have described the behavior of the velocity phase angle near the wall for turbulent flow. A sketch of their results is presented in Figure 3. It is evident from Figure 3 that in turbulent flow the velocity phase angle appears to exhibit a unique and interesting behavior near the wall.

One approach to obtaining more information on ϕ_u at small values of y is to measure the phase angle for the wall shear stress variation. The wall shear stress variation is given by

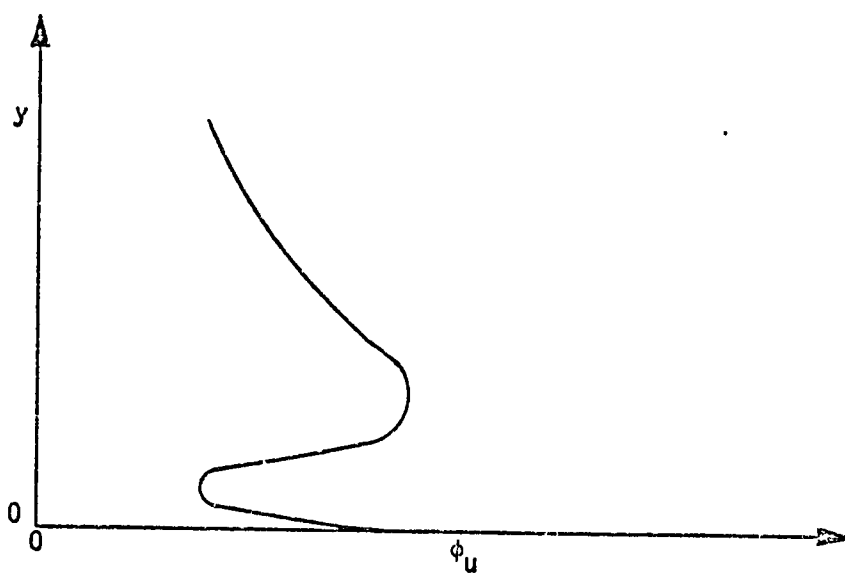$$\tau_w(x,t) = \tau_o(x) + \tau_1(x) \cos [\omega t + \phi_\tau(x)] \tag{3}$$

FIGURE 3. Behavior of ϕ_u near the wall in turbulent flow as calculated by Cousteix et al. [4]

where $\tau_0(x)$ is the mean shear stress, $\tau_1(x)$ is the half amplitude of the shear stress, and $\phi_\tau(x)$ is the shear stress phase angle. Lighthill [3] has stated that the wall shear stress phase angle ϕ_τ is equal to the velocity phase angle at the wall ($\lim_{y \to 0} \phi_u = \phi_\tau$). Thus, a measurement to obtain ϕ_τ would yield valuable information about ϕ_u.

However, measurement of the wall snear stress and subsequent evaluation of ϕ_τ is by no means simple at the present time. Surface shear stress measurements in steady flows can be made with a fair degree of accuracy using shear stress balances. Acharya et al. [5] provide a discussion of the present state of the art in the development of these instruments. However, due to long response times such instruments are generally not suitable for measurements in time-dependent flows. One instrument that has been considered for time-dependent wall shear stress measurement is the hot element gauge. Figure 4 describes a typical hot element gauge. It consists of a metallic element deposited on the substrate surface or buried flush with the surface. The substrate is an electrical insulator and ideally a thermal insulator. The metallic element is heated electrically by an external circuit and the response of the gauge is recorded by monitoring the external circuit. The external circuit is a constant temperature anemometer unit which is generally used to operate hot wire probes for velocity measurements. The substrate surface is mounted flush with the surface on which the boundary layer is developed. The operation of the gauge is based on the concept that the heat removed from the gauge by the flowing fluid is

related to the local wall shear stress. For steady flow with uniform shear (i.e., a linear velocity profile), there is a linear relationship between the heat transfer from the gauge and the one-third power of the local wall shear stress. In equation form, this relationship can be expressed as

$$q \sim [\tau_w/(\alpha x)]^{1/3} \qquad (4)$$

where q is the heat loss by the gauge and α is the fluid thermal diffusivity. This relationship was determined analytically by Kalumuck [6] using an order of magnitude analysis; by Ling [7] using a similarity analysis; and by Bellhouse and Schultz [8] using an integral analysis of the boundary layer. The heat transferred away from the gauge is equal to the power needed to maintain the gauge temperature and is monitored for shear stress measurements. Calibration is accomplished by placing the gauge in a flow where the shear stress is known and monitoring the power consumption for the gauge while varying the known shear stress. This sounds simple but even for steady laminar flow calibration must be performed under conditions similar to those encountered during actual use. A study to develop a comprehensive three-dimensional theory of hot film gauges in steady laminar flow has been performed by Kalumuck [6].

Since these gauges are small, easy to install and operate, and appear to have adequate response, they seem to offer an attractive possibility for measuring wall shear stress in unsteady flows. In fact, hot element gauges mounted flush with surfaces on which unsteady
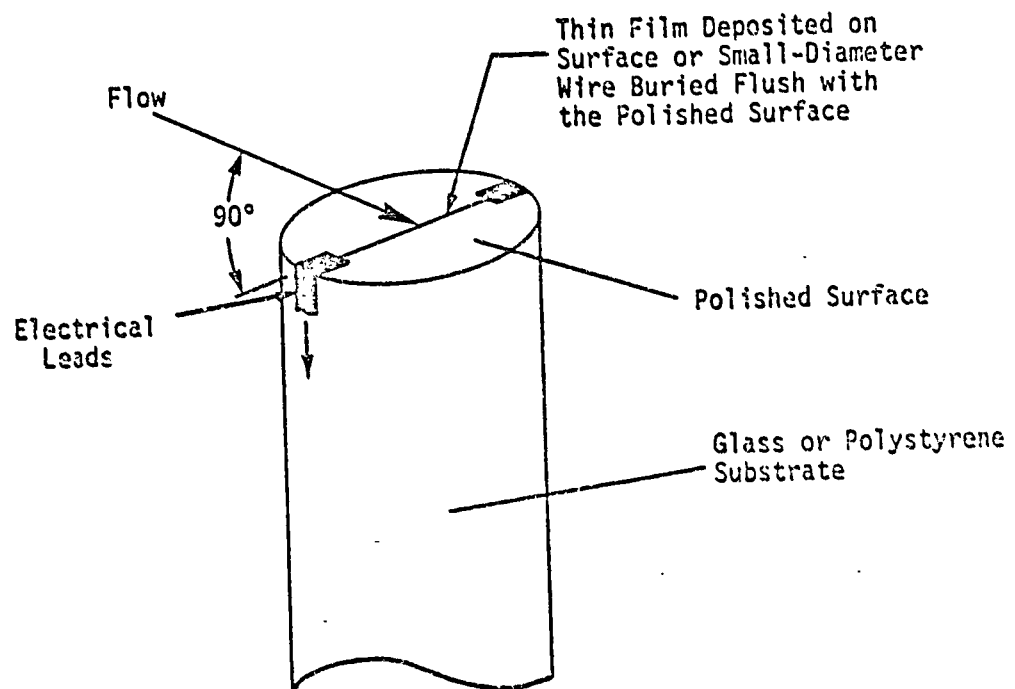
Thin Film Deposited on Surface or Small-Diameter Wire Buried Flush with the Polished Surface

Flow

90°

Electrical Leads

Polished Surface

Glass or Polystyrene Substrate

FIGURE 4. Description of a hot element gauge

boundary layers were developed have been used in at least three attempts

to measure ϕ_τ in turbulent flows. One study was conducted by Kobashi

and Hayakawa [9]. They studied turbulent boundary layers generated on a

flat plate which was oscillated sinusoidally parallel to a constant-

velocity freestream flow of air. Their results for ϕ_τ measurements

using hot film gauges show that the wall shear stress lags the

freestream velocity variation for the range of frequencies covered. The

value of ϕ_τ also decreased for an increasing reduced frequency

parameter, $\omega\bar{\delta}^*/U_o$ where $\bar{\delta}^*$ is the average displacement thickness. These

results differ with experimental and numerical studies for turbulent

flow reported so far in the literature [12,13].

In another study, Ramaprian and Tu [10] used flush mounted hot film

gauges to measure the wall phase angle in periodic turbulent pipe flow

of water. For the two frequencies at which data were available, the

measured wall phase angle lagged behind their numerical predictions and

an estimation of ϕ_τ obtained by the extrapolation of ϕ_u to the wall by a

significant margin. Figure 5 shows the numerical predictions and the

experimentally measured phase angles from Ramaprian and Tu. It is clear

that for the two cases in Figure 5, ϕ_τ values measured by hot film

gauges differ considerably from both their numerically predicted results

and results related to extrapolation of ϕ_u.

The third study is one conducted by Cook and Owen [11]. They

generated an oscillating turbulent boundary layer on the wall of a

constant cross sectional area test section open to the atmosphere. A
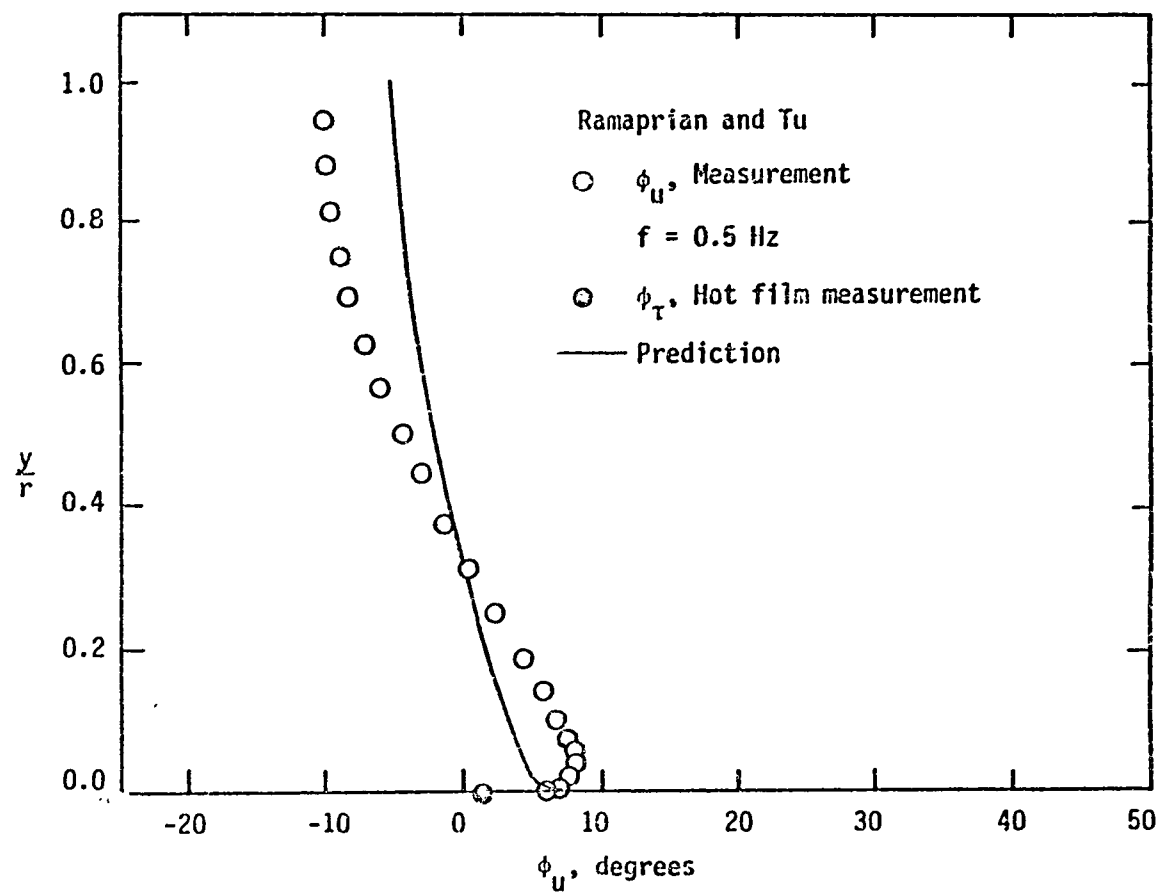
FIGURE 5. Phase angle results from Ramaprian and Tu [10]
(r is the radius of the pipe)
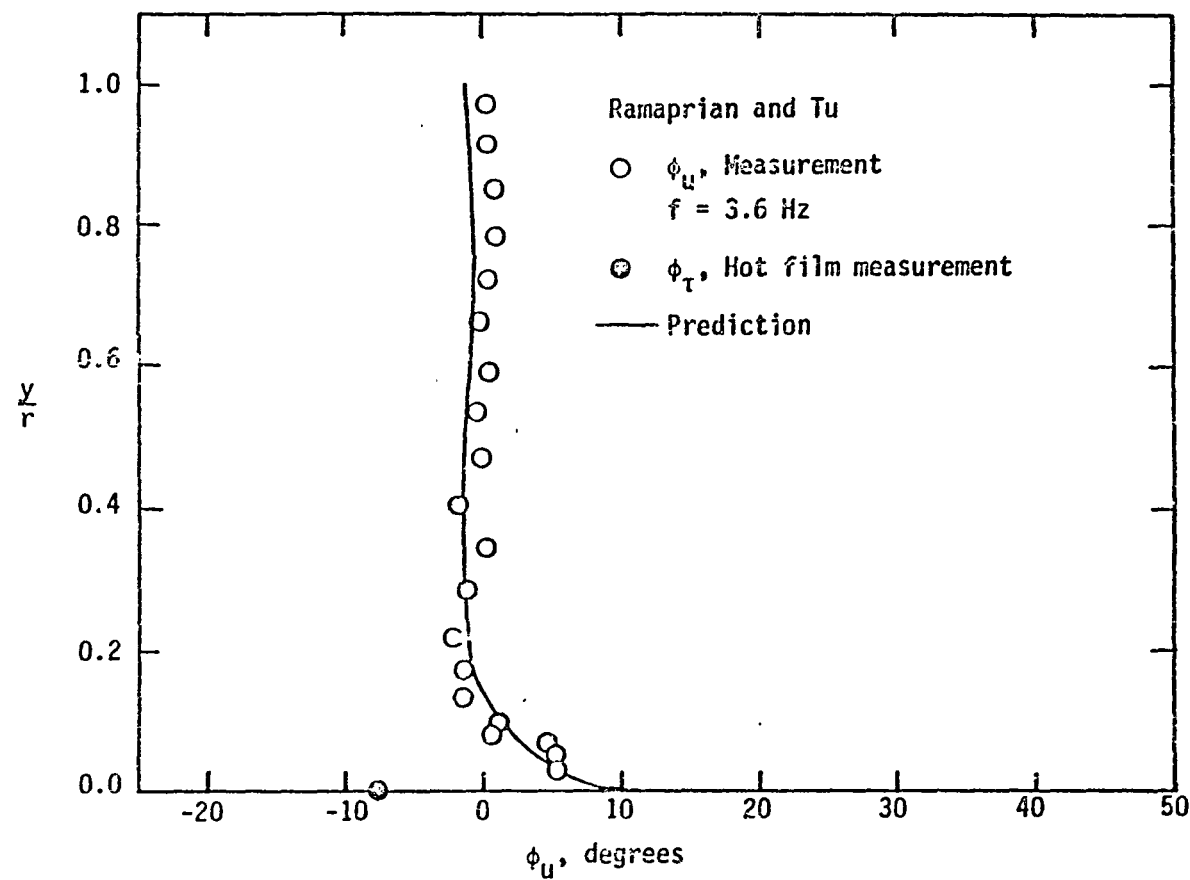
(b)   f = 3.6 Hz

FIGURE 5.   (Continued)

platinum film gauge was mounted flush with the wall of the test section at a fixed axial position. The wall phase angle was measured relative to the freestream and compared to numerical results produced from a computer code developed by Murphy and Prenter [12]. A graph of some measured wall phase angles is given in Figure 6 along with the corresponding predicted results. It is evident that a difference exists between the experimental measurements and the numerical predictions.

From the previous examples, it is evident that there is a discrepancy between ϕ_τ measured with the hot element gauges and the numerical predictions or the estimation of ϕ_τ obtained by extrapolating ϕ_u to the wall. Hence, it appears that the hot element gauges do not measure ϕ_τ correctly. However, it can not be said with certainty that the hot element gauges do not measure the correct phase angle, because neither the numerically computed ϕ_τ or the ϕ_τ obtained by extrapolation of ϕ_u to the wall are known to be correct for turbulent flows. Extrapolation of ϕ_u to the wall is particularly difficult if ϕ_u varies near the wall in the manner suggested by Cousteix et al. [4], Figure 3.

Examination of the processes taking place as the gauge responds to variations in the flow provides additional reasons for questioning the dynamic response of hot element gauges. The operation of a gauge is based on the process of heat transfer. As noted in Equation (4), for steady flow the heat transfer rate is proportional to the one-third power of the wall shear stress. In unsteady flows, heat transfer is still related to shear stress but possibly not in the form of Equation
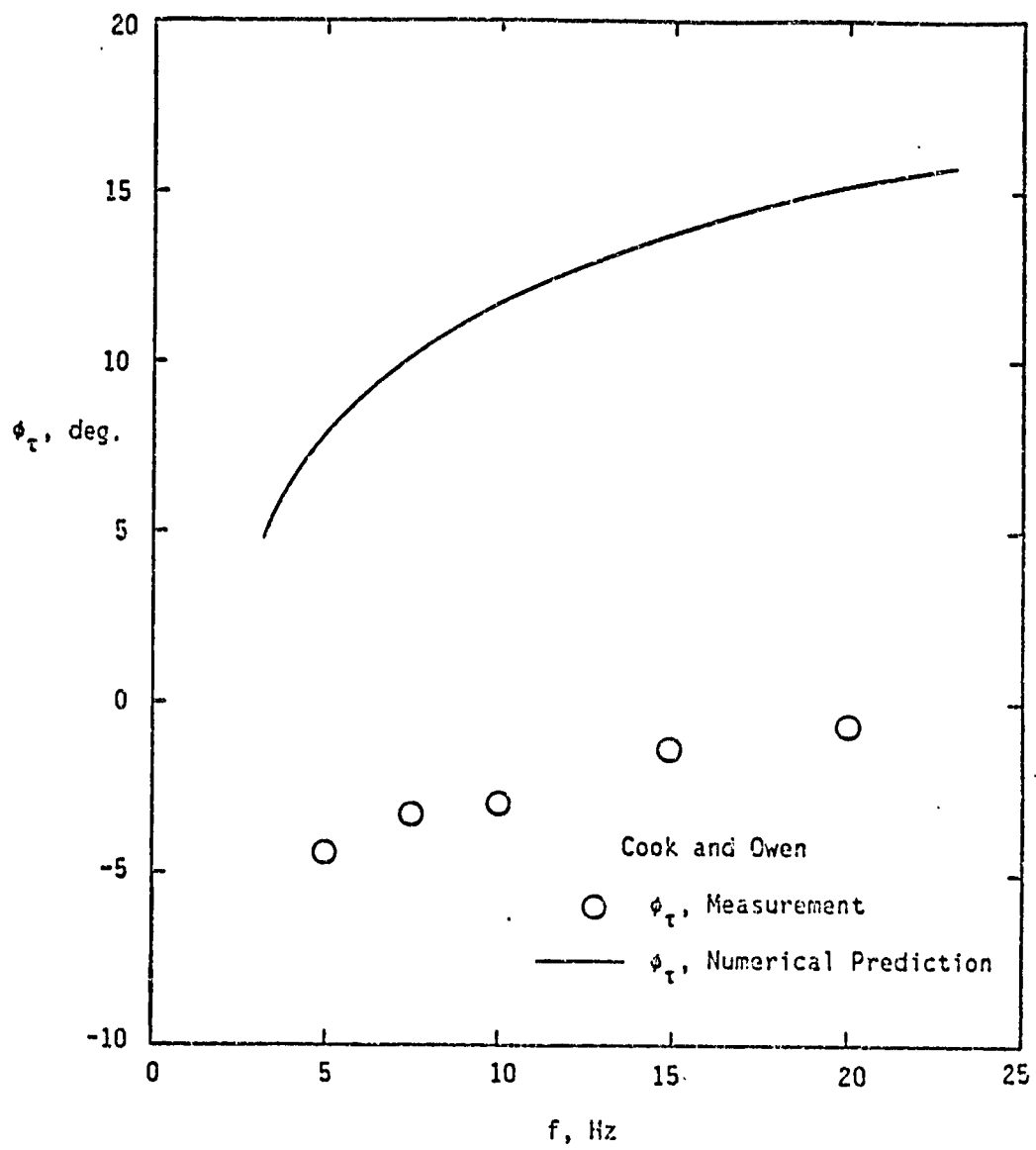
FIGURE 6. Wall phase angle measurements for a turbulent oscillating
flow by Cook and Owen [11]

(4). Ideally all the heat generated by the hot element should be
transferred to the fluid immediately above the element, but in actual
use the substrate surrounding the element is a thermal conductor. If
the metallic film or wire was perfectly insulated from the substrate it
would respond rapidly to fluctuations in the flow since it is very thin
and consequently has almost no thermal storage capacity. However, the
hot element does not act independently of its surroundings. It is
affected by unsteady heat conduction in the substrate which has a much
greater thermal storage capacity than does the hot element. This large
thermal storage capacity may produce a time lag and limit the response
of the system. Heat conduction upstream of the element causes a thermal
boundary layer to develop before the fluid reaches the element. Heat
may also be transferred from the boundary layer to the substrate
downstream of the element. As a result of all these factors, the
convective heat transfer and the conductive heat transfer are
interrelated and can not be uncoupled. The result is a very complex
multi-dimensional heat transfer problem that involves unsteady
conduction and convection.

Dewey and Huber [14] present a review of several studies related to
some of the theoretical aspects of the response of hot element gauges in
unsteady flows. They also describe a theoretical model they have
developed for the hot element gauge that includes the unsteady features
of its operation, but final solutions to predict the gauge performance
are not presented. Their discussion also suggests problems with the
dynamic response of hot element gauges in unsteady flows.

It would be useful to test the performance of hot element gauges in an oscillating flow for which unsteady aspects are known with a high degree of certainty. Laminar oscillating flow offers this feature. Accurate means are available for predicting the behavior of laminar oscillating flow, including ϕ_u vs y and the value of ϕ_τ. Therefore, this study deals with the testing of flush mounted hot element gauges in oscillating laminar flow. Efforts have been focused on measuring ϕ_τ and comparing these results to predicted values. This approach to analyzing the performance of the shear stress gauges subjects them to a crucial test. If the gauges do not yield the correct values for ϕ_τ in oscillating laminar flow then it can be concluded that the gauges fail to perform dynamically, i.e., they fail to follow the shear stress variation faithfully. Failure to perform properly in laminar oscillating flows would cast serious doubt on the usefulness of the gauges for measurements of ϕ_τ in unsteady turbulent flows.

One study in the literature has dealt with the use of hot element gauges in unsteady laminar flow. Bellhouse and Schultz [15] calibrated several hot film gauges in oscillating laminar flow for measuring fluctuating shear stress, but their work did not involve measuring the wall phase angle to determine if the gauges correctly follow the shear stress variations.

II. REVIEW OF OSCILLATING LAMINAR FLOW

As discussed in the Introduction, this study deals with oscillating

laminar flow. This section gives a general over view of the

fundamentals involved and some of the analytical, numerical, and

experimental work done in this area.

A. Lighthill's Solution to the Boundary Layer Equations

The boundary layer equations for incompressible unsteady laminar flow

over a flat plate are

$$\frac{\partial u}{\partial t} + u \frac{\partial u}{\partial x} + v \frac{\partial u}{\partial y} = - \frac{1}{\rho} \frac{\partial p}{\partial x} + \nu \frac{\partial^2 u}{\partial y^2} \tag{5}$$

$$\frac{\partial u}{\partial x} + \frac{\partial v}{\partial y} = 0 \tag{6}$$

where x is measured from the leading edge.

Lighthill [3] undertook the first analytical study for this type of

unsteady boundary layer. He considered small oscillations about a

steady mean velocity and represented the velocities by the following

equations

$$u = u_o(x,y) + \varepsilon u_1(x,y) \ e^{i\omega t}$$
$$v = v_o(x,y) + \varepsilon v_1(x,y) \ e^{i\omega t} \tag{7}$$
$$U = U_o(x) + \varepsilon U_1(x) \ e^{i\omega t}$$

The oscillating freestream velocity given in Equation (7) produces

the unsteady pressure gradient which is the driving force in oscillating

flow. Lighthill considered only this case for which the pressure gradient leads the freestream velocity by $\pi/2$. This is the case illustrated in Figure 1. There are other cases where the unsteady pressure gradient has different phase relationship with respect to the freestream velocity.

As would be expected, the unsteady pressure gradient plays a vital role in determining the behavior of the boundary layer. As previously noted, Lighthill has shown that this pressure gradient produces a velocity phase lead relative to the freestream velocity in the inner part of the boundary layer and a phase lag in the outer part of the boundary layer. Lighthill states that the phase difference in the boundary layer is related to the magnitudes of the inertia and the pressure gradient forces. In the inner part of the boundary layer, the pressure gradient forces dominate producing a phase lead, while in the outer part of the boundary layer the inertia forces are largest and a phase lag results. Lighthill's solution applies to laminar oscillating flows for which U_1/U_o is not large.

Lighthill's approximate method of solution to Equation (5) and Equation (6) restricted considerations to the low and high frequency limits. For the low frequency limit, the boundary layer equations were simplified and then solved by a Kármán-Pohlhausen method. The phase angle and fluctuating velocity profiles were found to depend on the reduced frequency parameter, $\bar{\omega} = \omega x/U_o$ where x is the axial distance from the leading edge of the flat plate. The reduced frequency is also

known as the Strouhal number and is the characteristic frequency

parameter in oscillating flow. Lighthill's low frequency solution for

ϕ_τ for laminar oscillating boundary layer flow over a flat plate with

$dU_o/dx = 0$ is shown in Figure 7. At large frequencies, the unsteady

boundary layer equations reduce to the equation for 'shear waves'.

Thus, at large frequencies, the boundary layer behaves as if it were

subjected to a freestream which oscillates about a zero mean velocity.

Lin [16] also observed this characteristic of high frequency oscillating

flow. For this high frequency limit, ϕ_τ is independent of frequency and

reaches a constant value of 45 degrees. Lighthill's high frequency

solution is also shown in Figure 7.

B. Numerical Solution to the Boundary Layer Equations for ϕ_τ

Several numerical computer codes have been developed to solve the

unsteady boundary layer equations for both laminar and turbulent flows.

Murphy and Prenter [12] have developed a hybrid finite-element finite-

difference scheme which is second-order accurate in "x" and "t" and

fourth-order accurate in "y". Murphy and Prenter compared their results

for ϕ_τ to the computational procedure of Cebeci and Carr [17] and

Lighthill's low and high frequency asymptotic solutions [3]. These

results are given in Figure 7. As can be seen from Figure 7, there is

good agreement between the various studies. This demonstrates that

accurate prediction of ϕ_τ is possible in oscillating laminar flow. The

computer codes have the advantage over the method by Lighthill in that

they can predict ϕ_τ over the full range of reduced frequencies.
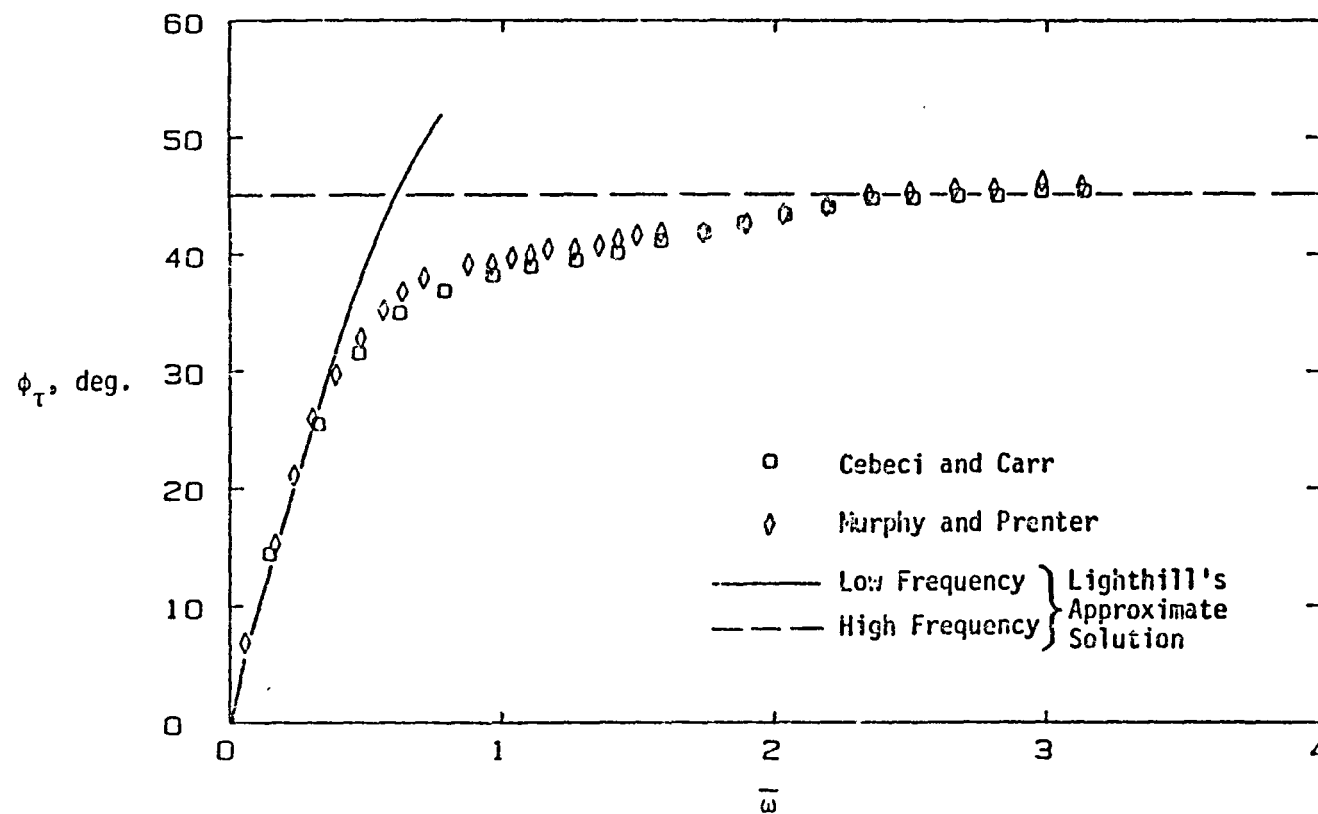
FIGURE 7. Prediction of ϕ_τ for oscillating laminar flow over a flat
plate with a zero mean pressure gradient [12]

One aspect of solving Equation (5) and Equation (6) for laminar oscillating flow is that the solution is independent of the magnitude of U_1/U_o as long as the amplitude is not large.

C. Hill and Stenning Study of Oscillating Laminar Flow

An experimental and analytical study of oscillating laminar boundary layers was conducted by Hill and Stenning [18] for flows with both zero and adverse pressure gradients.

A laminar boundary layer was produced on the wall of the test section in a simple open-circuit suction-type wind tunnel. A hot wire anemometer was used for flow velocity measurements. A sliding throttle valve located in the downstream portion of the test section created the freestream oscillations. The governing equations for the flows developed are given by Equation (5) and Equation (6) with a freestream velocity

$$U = U_o(1 - \xi) + U_1 \cos \omega t \tag{8}$$

where $\xi = b_1 x/U_o$ is the dimensionless pressure gradient term with b_1 equal to the rate of decrease of freestream velocity with distance from the leading edge. Calculation of ξ was carried out by applying Equation (5) in the freestream

$$-\frac{1}{\rho}\frac{\partial p}{\partial x} = \frac{\partial U}{\partial t} + U\frac{\partial U}{\partial x} \tag{9}$$

Two values of the dimensionless pressure gradient term were studied; $\xi =$ 0 and $\xi = 0.10$. These two cases correspond to Blasius flow and Howarth flow respectively. The Howarth flow case represents a flow that is close to separation, where separation occurs at $\xi = 0.12$. When $\xi = 0$, Equation (8) reduces to Equation (1) given in the Introduction. The results reviewed here from Hill and Stenning will concentrate on $\xi = 0$ since this type of flow is similar to the one considered in the current study. Velocity variations, U_1/U_o, of the order 0.1 were used in their study which was performed over the reduced frequency range $0 < \bar{\omega} < 10$. Their results show that the boundary layer behavior can be grouped into three classes depending on $\bar{\omega}$. These classes are low, intermediate, and high reduced frequencies. The range of $\bar{\omega}$ in each group depends to some extent on the magnitude of the steady pressure gradient. For $\xi = 0$, the low frequency range is $0 < \bar{\omega} < 0.6$, and in this range Lighthill's low frequency theory was used to predict the boundary layer behavior. The high frequency range corresponds to large values of $\bar{\omega}$. In the high frequency range, the shear wave theory should give a good description for both the phase angle and the amplitude of the boundary oscillations. Since the theory existing at the time of their study did not adequately predict the boundary layer behavior in the intermediate frequency range, Hill and Stenning developed a theoretical solution to cover the range between the low and high frequencies.

Examples of experimental results of Hill and Stenning for three quantities related to oscillating flow, u_o/U_o, u_1/U_1, and ϕ_u, are

presented in Figure 8. Figure 8(a) compares their experimental results
for u_o/U_o in oscillating flow to u/U in steady flow, both for $\xi = 0$.
The velocity ratio for both cases are plotted against $\eta = y\sqrt{U_o/\nu x}$. The
Blasius theoretical solution is also shown for comparison. For the
oscillating flow u_o/U_o profile, $\bar{w} = 0.555$ which was the only $\bar{w}$ for which
u_o/U_o data were available in reference [18]. The results presented in
Figure 8(a) show a small difference between the two experimental
profiles at the outer edge of the boundary layer. This difference could
be caused by a favorable pressure gradient present only during steady
flow operation, unsteady effects, or experimental error. However, Hill
and Stenning state that the mean velocity profile in oscillating flow is
unaffected by the velocity fluctuations. Karlsson [13] observed in his
experimental study of zero pressure gradient laminar oscillating flows
that in oscillating flow the mean velocity profile was not affected by
oscillations as long as the fluctuating velocity was not extremely large
compared to the mean velocity. Hence, it is generally accepted that the
u_o/U_o profile remains essentially the same for all $\bar{w}$ [13,18].

Another interesting characteristic of oscillating flow involves the
fluctuating velocity in the boundary layer. In the outer part of the
boundary layer u_1 has a magnitude larger than U_1. This is called the
overshoot and is associated with all frequencies in oscillating flow.
Figure 8(b) shows theoretical and experimental u_1/U_1 vs η profiles
obtained by Hill and Stenning for $\xi = 0$ and $\bar{w} = 1.47$, which is in the
intermediate frequency range. The intermediate frequency theory
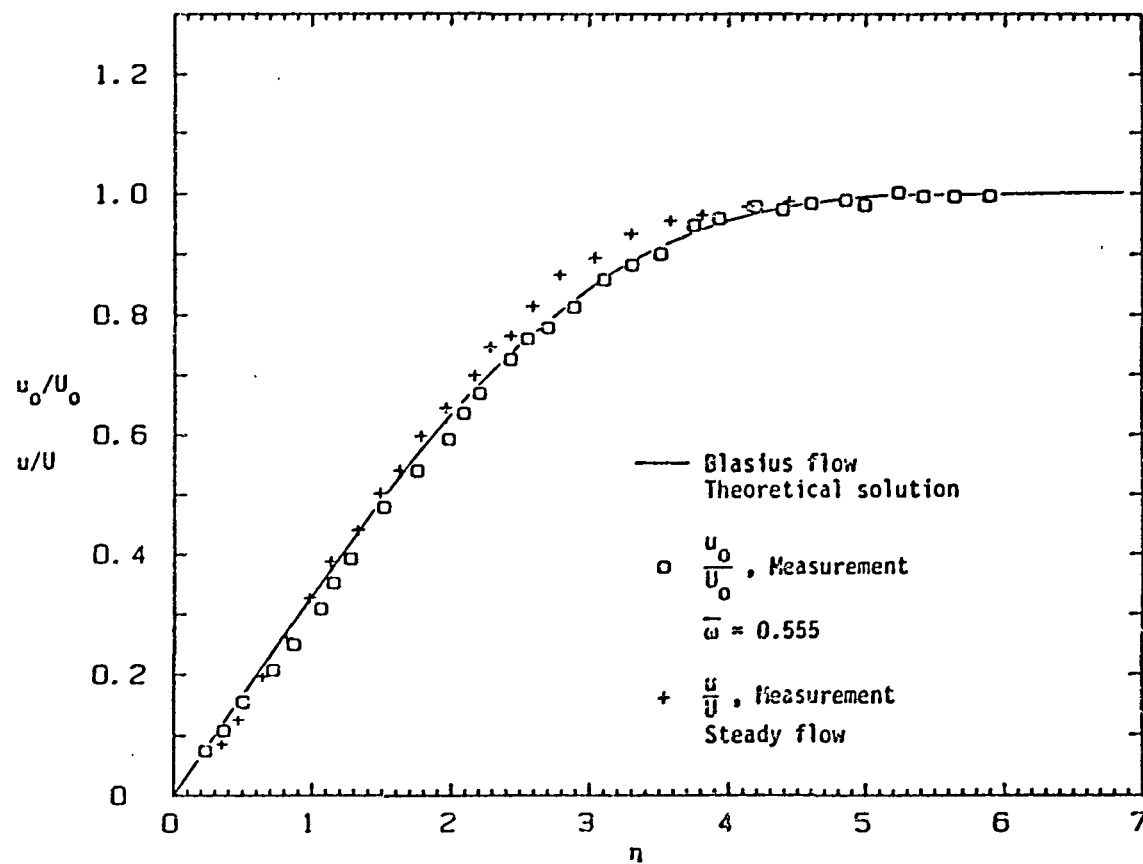
(a) Comparison of mean velocity profiles for oscillating flow and steady flow

FIGURE 8. Experimental boundary layer results from Hill and Stenning for oscillating laminar flow [18]

(b) u_1/U_1

FIGURE 8. (Continued)

Intermediate frequency
Theoretical solution
$\bar{\omega} = 1.48$

$\square$ ϕ_u, Measurement
$\bar{\omega} = 1.48$

$\oplus$ ϕ_T, from Figure 7 at $\bar{\omega} = 1.48$

— — — Extrapolation of experimental results

ϕ_u, deg

η
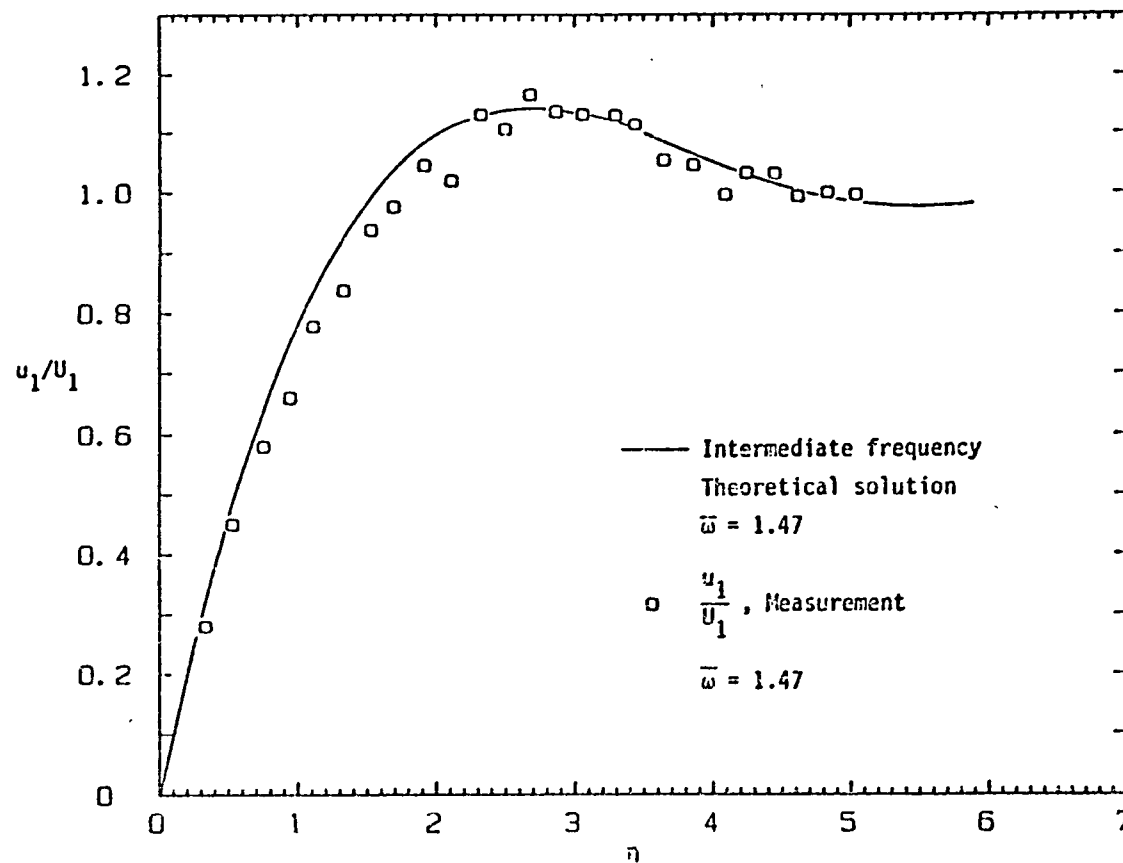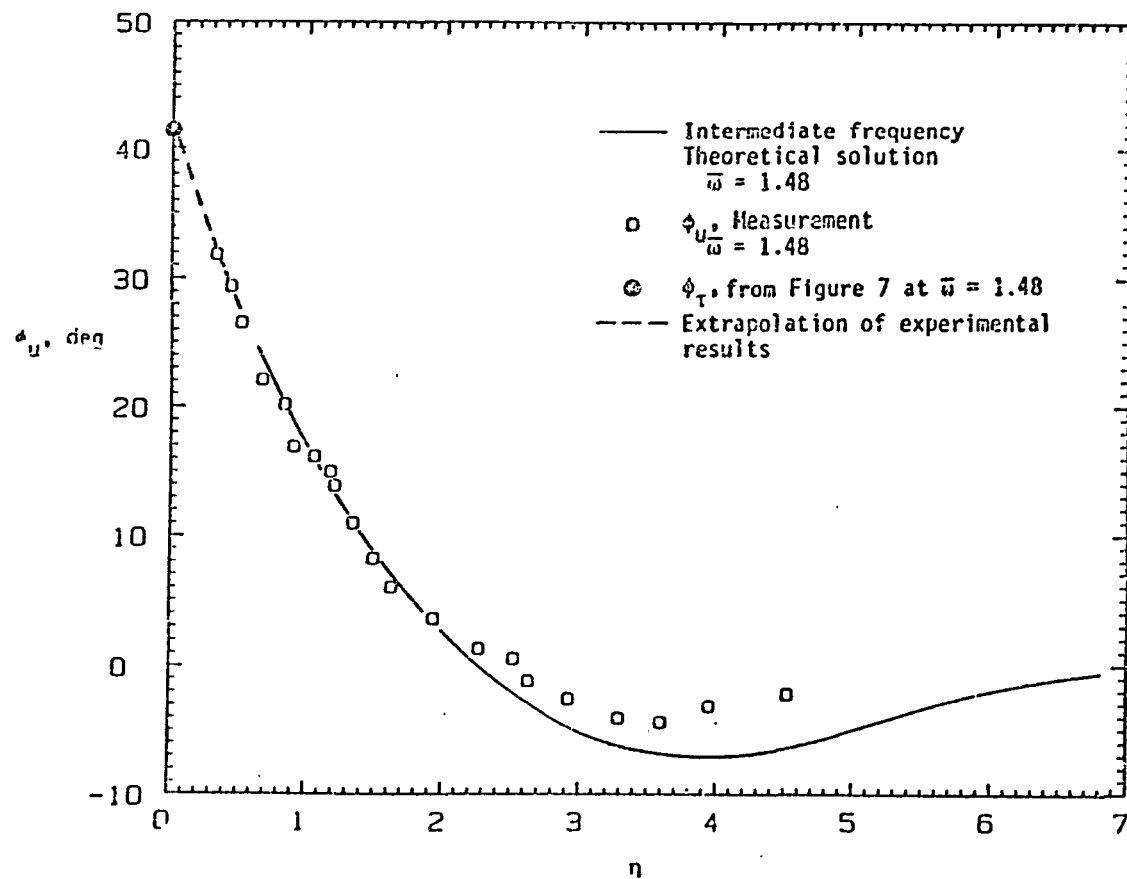
(c) ϕ_u

FIGURE 8. (Continued)

provides a good description of the actual boundary layer behavior for this case. Figure 8(c) illustrates the behavior of ϕ_u in the boundary layer for $\bar{\omega} = 1.48$. The experimental results presented in Figure 8(c) confirm the theory provided originally by Lighthill which states that the velocity in the inner part of the boundary layer leads the freestream velocity and the velocity in the outer part of the boundary layer lags the freestream velocity.

Hill and Stenning did not measure ϕ_τ, but it is possible to obtain an estimation by extrapolating the experimental ϕ_u data to the wall in Figure 8(c). Using this method, $\phi_\tau = 42°$. From Figure 7, the numerical prediction of ϕ_τ at $\bar{\omega} = 1.48$ is approximately $41.5°$ and has been placed on Figure 8(c) as the solid circular symbol. This comparison results in good agreement between the numerical prediction and the experimental estimation of ϕ_τ and indicates that for this case the numerical prediction of ϕ_τ from Figure 7 is correct.

The results of the Hill and Stenning study provide confidence that oscillating flow laminar boundary layers can be generated that behave according to theory. The next three chapters describe how oscillating flow laminar boundary layers were generated and measured in the present study. Also presented is a comparison of experimental results with numerical predictions.

III. FACILITY DESCRIPTION

The unsteady boundary layer flow facility in the Iowa State
University Mechanical Engineering Department was utilized in this study.
A diagram of the flow facility is shown in Figure 9 and descriptive
details are given in Table 1. For more information about the facility
see Cook [1,2]. The upstream end of the square constant cross-sectional
area test section is attached to the round-to-square entrance section.
The entrance section is open to the atmosphere. Located at the
downstream end of the test section is the converging-diverging nozzle
and an oscillating wedge that makes up the wave-generating mechanism.
Downstream of the nozzle is a large vacuum tank. To generate flow, a
mylar diaphragm is first placed between the nozzle exit and the tank.
The tank is then evacuated. Rupturing the diaphragm causes atmospheric
air to flow through the test section and the nozzle to choke. The test
flow is terminated when the nozzle discharge region pressure has
increased to the point where the nozzle unchokes. When the wedge in th
wave-generating device is fixed steady subsonic flow will be produced in
the test section. Duration of steady flow is primarily determined by
tank volume and the net throat cross sectional area.

The wave-generating device is used to create the velocity
fluctuations. It consists of a scotch yoke mechanism which oscillates
the wedge along the nozzle axial centerline and produces a sinusoidal
variation in freestream velocity when the input shaft is rotated at a
constant speed. When the wedge is in the fully downstream position, the
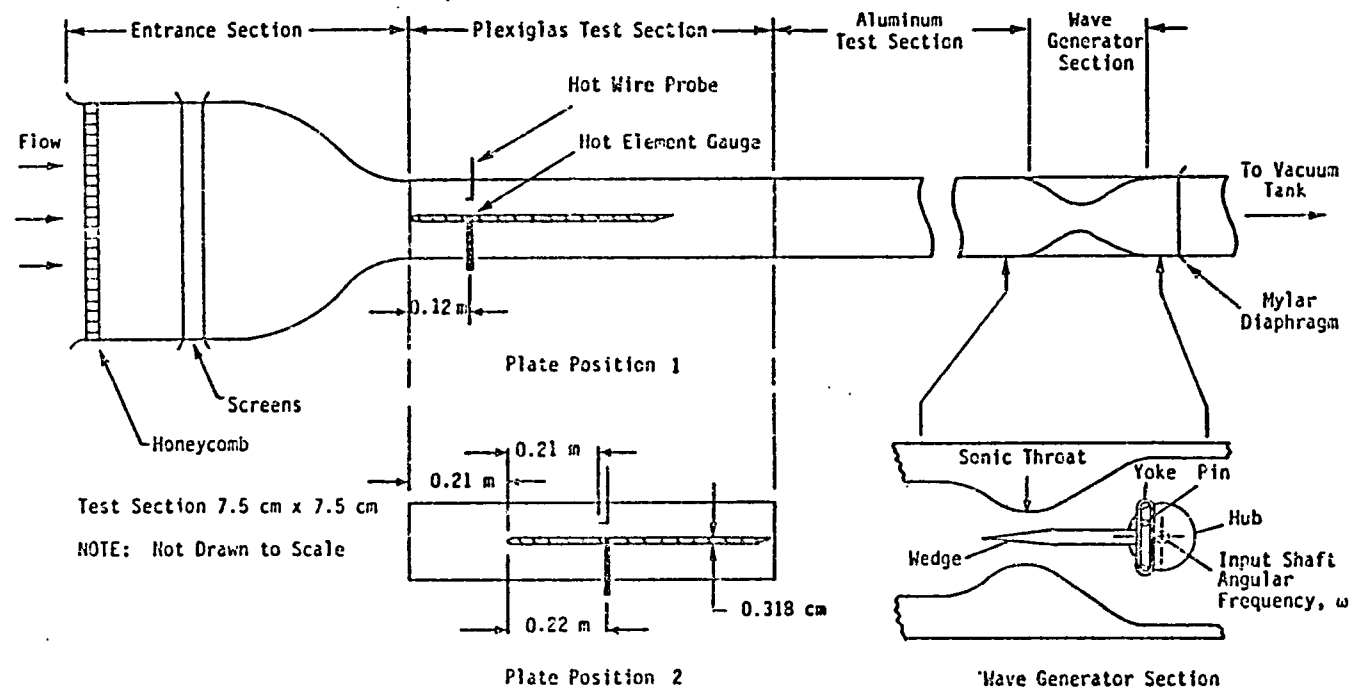
FIGURE 9. Diagram of the oscillating flow facility and test section configurations

TABLE 1. Description of the facility

Plexiglas Test Section	
Length	76.2 cm
Width	7.5 cm
Height	7.5 cm
Entrance Section	
Honeycomb Cell Depth	4 cm
Screen Solidity Ratio/Per Screen	0.3
Contraction Ratio	12.4:1
Tank Volume	2 m^3

wedge tip extends upstream of the plane of minimum cross-sectional area of the nozzle. Changing the wedge position changes the effective sonic throat area, thereby changing the mass flow rate. Proper shaping of the wedge produces a sinusoidal variation in the freestream flow superposed on a constant mean velocity when the nozzle is choked. A sinusoidal freestream velocity is obtained over a wide range of frequencies. The frequency for the present study was infinitely adjustable between approximately 2 Hz to 30 Hz.

Two low speed flows were produced in the test section with freestream velocities of about 11 m/s and 17 m/s. The two freestream flow conditions were created by two wave generator section configurations which are described in Table 2. For this study, three combinations of the plate positions (Figure 9) and wave generator section configurations (Table 2) are used. These three combinations

are described in Table 3 and will be referred to as test configurations TC I, TC II, and TC III. Table 4 tabulates test configurations in relation to the experimental cases studied and will be referred to in later chapters.

TABLE 2. Description of the wave generator section configurations

Wave Generator Section Configuration	Stroke,cm	Wedge half Angle,deg.	Nominal Choked-flow Run Time,sec.	U_o,m/s	U_1/U_o [a]
A	0.6350	7.0	10	16.7	0.13
B	0.6350	7.0	15	11.7	0.19

[a]At low frequencies.

TABLE 3. Description of the test configurations

Test Configuration	Wave Generator Section Configuration	Plate Position	x, m	Re_x [a]	β
TC I	A (Table 2)	1 (Fig. 9)	0.12	1.34×10^5	0.10
TC II	A (Table 2)	2 (Fig. 9)	0.22	2.45×10^5	0.10
TC III	B (Table 2)	2 (Fig. 9)	0.22	1.72×10^5	0.16

[a]Based on U_o.

TABLE 4. Experimental boundary layer surveys

CASE DESIGNATION PREFIX
  A - Wave Generator Section Configuration A, Table 2
  B - Wave generator Section Configuration B, Table 2
  C - Steady Flow

CASE	TEST CONFIGURATION	f,Hz	$\frac{a}{\omega}^a$
A1	TC I	10.00	0.45
A2	TC II	3.00	0.25
A3	TC II	5.58	0.44
A4	TC II	10.00	0.78
A5	TC II	15.00	1.18
A6	TC II	20.00	1.59
B1	TC III	3.00	0.34
B2	TC III	10.00	1.19
B3	TC III	20.00	2.38
C1	TC I		
C2	TC II		

$^a\frac{}{\omega}$ is based on the measured value
of U_o (Appendix A).

A flat steel plate with an elliptical leading edge and a sharp trailing edge was installed along the centerline in the upstream part of the test section. The plate surface and leading edge was polished to an RMS finish of 15 µ inches in order to ensure laminar flow. Holes were drilled in the plate at distances of $x = 0.12$ m for plate position 1 and $x = 0.22$ m for plate position 2. This permitted the hot element gauges to be installed through the bottom of the test section and flush with the top surface of the plate. When a hot element gauge was not installed in a probe location, the hole was filled with wax to minimize flow disturbances. The hot element and hot wire probes were placed centrally with respect to the side walls of the test section. The hot wire probe shown in Figure 9 was used to measure the velocity variation in the boundary layer. All measurements for the boundary layer analysis and wall phase angles were made above the plate.

IV. DATA AQUISITION SYSTEM FOR VELOCITY MEASUREMENTS

Two basic instrumentation setups were used for this study; one for measuring freestream and boundary layer velocities by means of a hot wire anemometer and another for measuring the wall phase angle using the hot element gauge. The former will be described in this section.

A diagram of the instrumentation used to measure velocities is given in Figure 10. Velocities in the test section were measured by a constant temperature hot wire system. A single channel anemometer maintained a Disa P14 hot wire probe at a constant temperature with an operating resistance ratio (ORR) of 1.8. The ORR is defined as R/R_f where R_f is the resistance of the hot wire at the fluid temperature and R is the operating resistance of the hot wire. The term over heat ratio (OHR) is often used when describing the operation of hot wire anemometers, where OHR = $(R - R_f)/R_f$. The ORR and the OHR are related by the equation ORR = OHR + 1. The signal out of the anemometer was linearized and then sent through a low pass filter set at 10 kHz to eliminate the high frequency electrical noise. An A/D voltmeter was then used to convert the filtered signal from analog to digital form for computer processing. This basic procedure for measuring velocities was used for both steady and oscillating flows.

Calibration of hot wire probes was done outside the test section using a TSI model 1125 air flow calibrator and standard calibration techniques.

External trigger,
one per cycle

DISA Type 55D01
Anemometer
Main Unit

DISA Type
55D10
Linearizer

DISA Type
55D25
Auxiliary
Unit
(Filter)

Hewlett
Packard 3437A
A/D
Voltmeter

Commodore
Computer
System,
Machine
Language
Programmed

Oscilloscope

Probe positioning
mechanism

Test section
wall

DISA P14 Single-wire probe

Flow

Flat plate
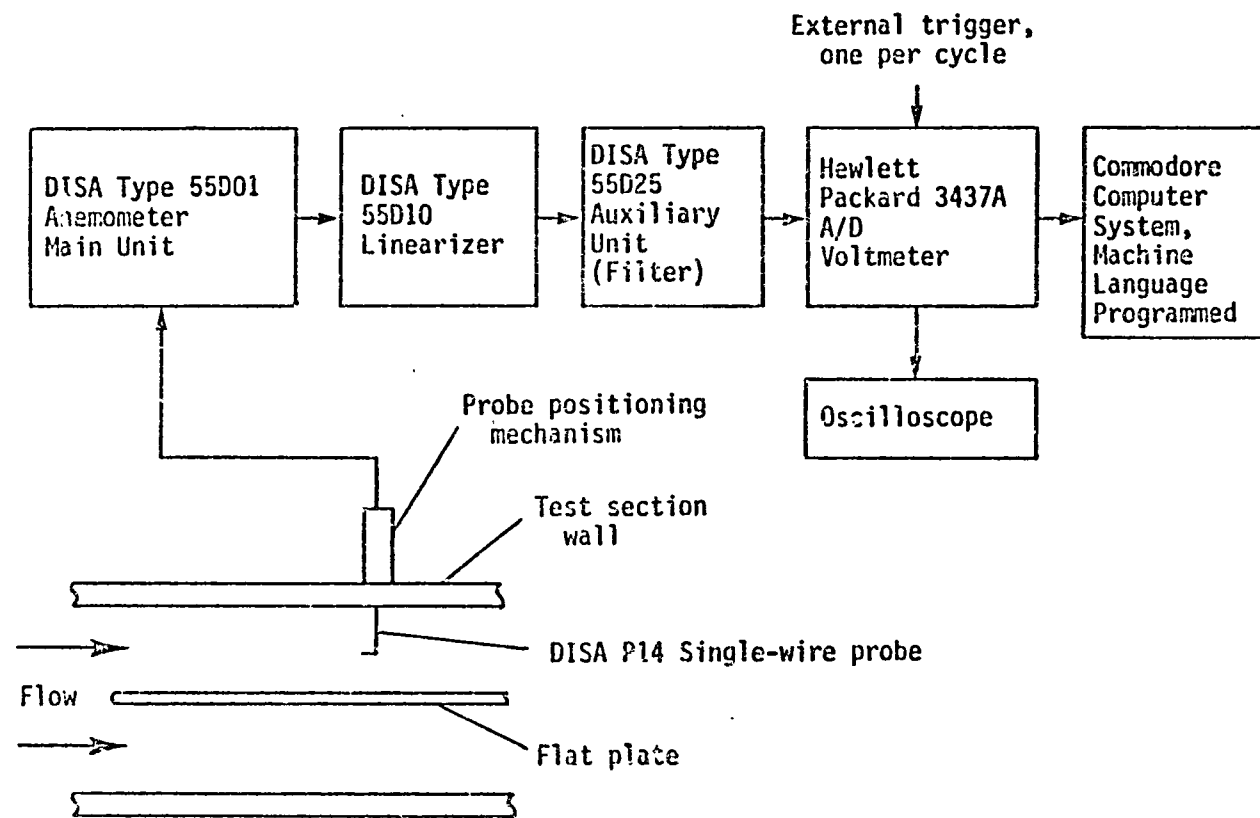
FIGURE 10. Data acquisition system for velocity measurements

To traverse the boundary layer, a hot wire probe positioning mechanism built around a micrometer enabled the probe distance from the p.ate to be adjusted.

A. Steady Flow

When steady flow velocities were being measured the wedge in the wave generator section, Figure 9, was locked at midstroke. Velocities in the boundary layer surveys were then measured by taking 500 voltage readings over a 1.5 second time interval at each y location selected. Using this information and a previous hot wire calibration, the average velocity and RMS velocity were evaluated by the computer for each data point in the survey.

B. Oscillating Flow

Oscillating flow required the wedge to be driven at a known and constant frequency. A variable speed electric motor and a flywheel provided the constant speed while an EPU counter in conjunction with an optical pickup monitored the speed. The error in speed was estimated to be ± 0.5 percent.

The sampling was initiated by a once-per-revolution trigger sent to the voltmeter (Figure 10). This signal was initiated by a magnetic pickup in association with a steel part connected to the wave-generator drive shaft. Before the signal was sent to the voltmeter, it was conditioned and amplified to provide an appropriate trigger signal. Hot

wire voltage readings were taken at 20 equally spaced time intervals over the period of each cycle of oscillation at a given y location. Each of these 20 voltages per cycle was ensemble averaged over a number of cycles. The total number of cycles was determined by the run time of the facility and the period of oscillation. For frequencies of 7 Hz and less, the voltages were ensemble averaged over 10 cycles while the remaining frequencies were ensemble averaged over 50 cycles. The 20 ensemble averaged voltages were converted to velocities by use of the calibration for the hot wire. The RMS velocity variation at each of the 20 points was also obtained. A cosine wave was then fitted to the 20 ensemble averaged velocity values to yield an expression for the velocity variation of the form

$$u(t) = u_o + u_1 \cos [\omega t + \phi_u]$$

Figure 11(a) shows typical oscilloscope records of hot wire signals obtained with the probe in the freestream and in the boundary layer. It is evident from Figure 11(a) that even in the boundary layer the hot wire signals are relatively clean. The RMS velocities varied from approximately 0.05 m/s to 0.09 m/s. This corresponds to approximately 0.4 percent of the mean velocity. These oscilloscope records illustrate that a laminar boundary layer is present in the test section. The values of Re_x in Table 3 also indicate that a laminar boundary was present. These values range between 1.34×10^5 and 2.45×10^5. Transition from laminar flow to turbulent flow over a smooth flat plate occurs in steady flow at $Re_x \cong 3 \times 10^6$ [19].

Figure 11(b) displays the results of a comparison between the 20 ensemble averaged velocity values and the cosine wave fit for the given y locations in the freestream and in the boundary layer. It is evident from the figure that in each case the ensemble averaged velocity values lie very close to the fitted cosine wave; hence, the ensemble averaged velocity variation in the test section was essentially sinusoidal. The frequency for the results in Figure 11 was 10 Hz. These results are typical of those obtained at all frequencies.
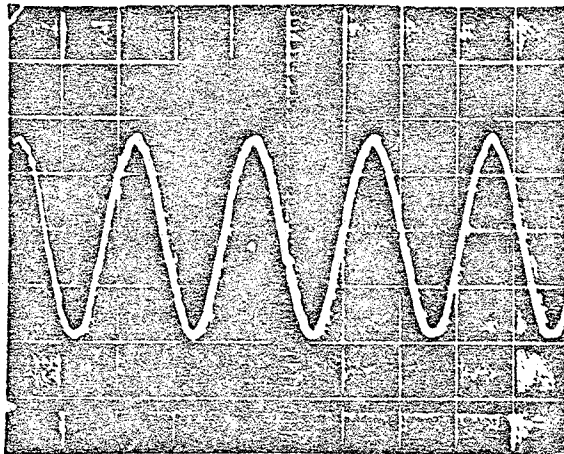
TC II
f = 10 Hz
y = 19.736 mm
(y > δ)
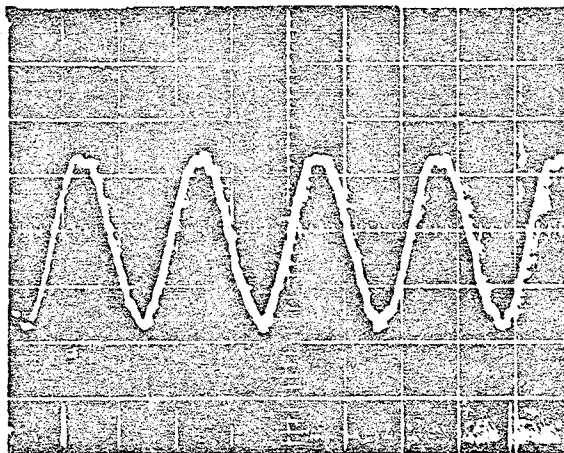
TC II
f = 10 Hz
η = 1.26
(y = 0.559 mm)
(y < δ)

(a) Oscilloscope records of hot wire signals in the freestream
     and in the boundary layer

FIGURE 11. Typical experimental results for oscillating laminar boundary
            layer flows
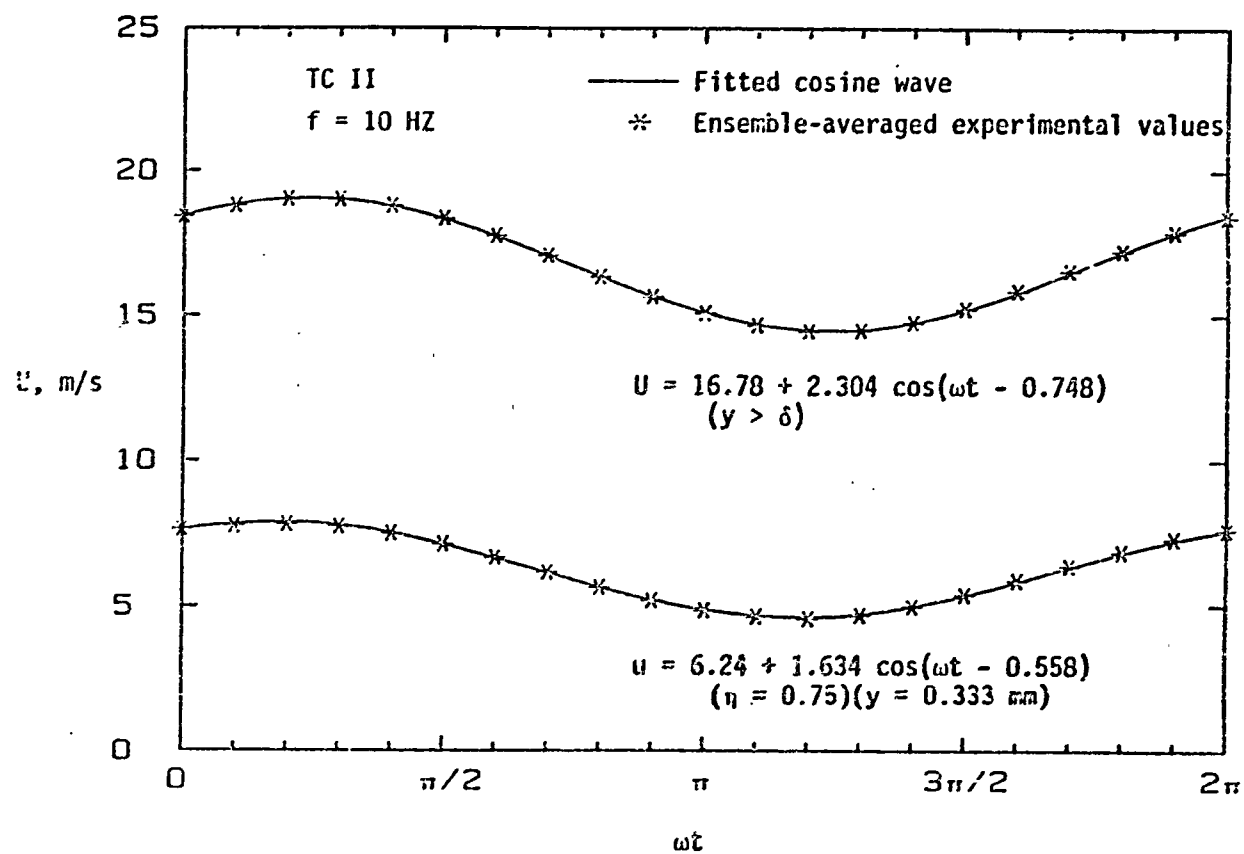
(b) Cosine wave fit to the velocity in the freestream and in the
boundary layer (angles are in radians)

FIGURE 11. (Continued)

V. RESULTS OF THE BOUNDARY LAYER STUDY

Generating a laminar boundary layer and predicting the behavior required considerable work and effort. The experimental work for this study was conducted at Iowa State University and the numerical predictions were supplied by Dr. John Murphy of the NASA Ames Research Center. The numerical method used was that of Murphy and Prenter [12].

A major objective of the boundary layer study was to ensure that the boundary layer behavior observed experimentally and the corresponding numerically predicted behavior were in reasonable agreement. If such agreement exists then the numerically predicted ϕ_τ values can be compared with corresponding ϕ_τ values measured by means of the hot element gauges. This chapter is devoted to comparison of experimental and predicted boundary layer behavior.

A. Comparison of the Experimental Boundary Layer Results With Numerical Predictions

Boundary layer behavior was studied for both steady and for oscillating flow at various frequencies, two axial locations, and two mean freestream velocities. The steady flow and oscillating flow experimental and numerically-determined velocity profiles will be presented in dimensionless terms in the form of u_o/U_o and u_1/U_1 vs $\eta = y\sqrt{U_o/\nu x}$. The velocity phase angle ϕ_u, is also plotted against η. The experimental cases studied are listed in Table 4.

The first attempts to numerically predict the boundary layer behavior assumed that a zero mean pressure gradient existed in the test section for oscillating flows. Since the mean velocity profile u_0/U_0 for oscillating flows is generally accepted to be the same as the corresponding steady flow velocity profile, the theoretical variation in u_0/U_0 with η is the Blasius profile. Using experimental case A6 (Table 4) as an example, the experimental u_0/U_0 velocity profile is compared in Figure 12 with the Blasius profile.

Before proceeding further with the comparison of the experimental results with the numerical predictions it is important to consider the uncertainty in the measurements. The largest source of error in the velocity profile is in y, the distance of the hot wire from the plate. A fixed error in y is reflected in a fixed error in η ($\eta = y\sqrt{U_0/\nu x}$). It was found that a conventional hot wire probe with straight wire support prongs inserted perpendicular to the plate surface did not properly measure the velocity in the boundary layer so it was necessary to use probes with right angle bends in the wire support prongs (Disa P14 probes: see Figure 9). Further, it was important that the axis of the prongs near the wire be aligned parallel with the flow direction. When the wire support prongs touched the plate surface, the hot wire itself was above the plate surface. This occurred because the ends of the support prongs near the wire are tapered. As a result, accurate measurement of the distance from the wire to the plate was difficult. A means was required to determine the hot wire position. The method used

involved attaching a thin block of known thickness to the plate near the
probe axial position and inserting the plate in the test section. Then
by looking through the test section wall with a low power magnifier, the
micrometer dial reading corresponding to the hot wire position when it
was aligned with the block surface was determined. The plate was then
removed from the test section and the block removed. The plate was then
reinstalled and secured in position. This procedure resulted in some
uncertainty for the micrometer reading corresponding to $y = 0$ for the
hot wire. This error is difficult to estimate but based on experience
with the measurement system the value of ± 0.10 mm seems the largest
possible value. The bars in Figure 12 indicate the range of η for case
A6 corresponding to the uncertainty in y of ± 0.10 mm.

It is evident from Figure 12 that an error in determining the $y = 0$
probe position reflects in an error in the experimental boundary layer
velocity profiles. When the experimental oscillating flow u_o/U_o
velocity profiles and the steady flow velocity profiles were plotted
against η it was observed that the extrapolated profiles did not pass
through zero. This was interpreted to be due to an error in y.
Therefore, the profiles were adjusted to correct this error. This
correction required a change in y of 0.075 mm to 0.10 mm. The
experimental results in Figure 12 and subsequent figures reflect this
correction. The experimental data points in Figure 12 lie close to the
curve drawn through them. The absence of large scatter around the curve
lends confidence to the experimental velocity profile. This is
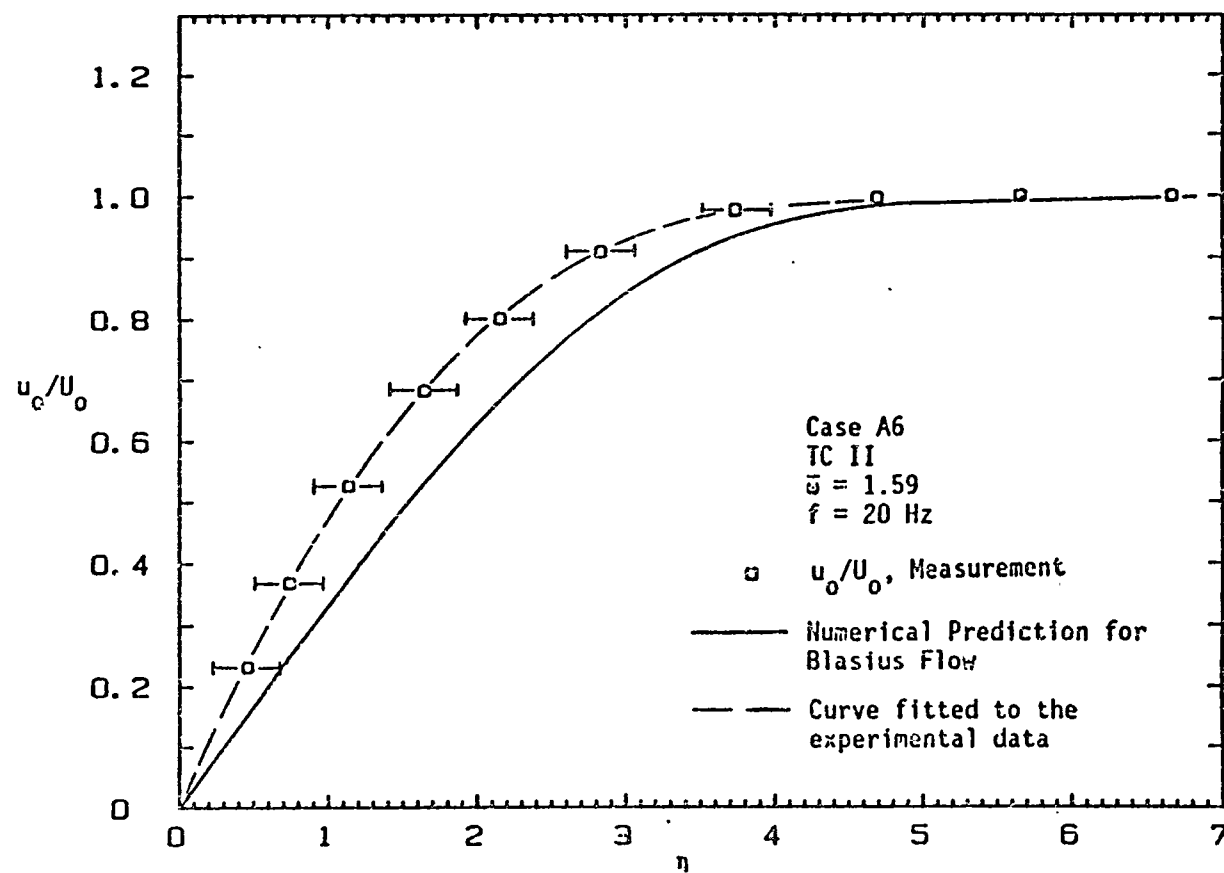
FIGURE 12. Comparison of the experimental oscillating flow u_o/U_o results from case A6 to the Blasius flow numerical prediction

The figure shows a plot with axes u_o/U_o (vertical) and η (horizontal, 0 to 7), with labels:

Case A6
TC II
$\bar{\omega} = 1.59$
$f = 20$ Hz

□ u_o/U_o, Measurement

——— Numerical Prediction for Blasius Flow

— — Curve fitted to the experimental data

consistent with an uncertainty analysis presented in Appendix C which
indicates that uncertainties in x, y (exclusive of the removed fixed
error), and U produce an uncertainty region in the experimental results
in Figure 12 that is about the symbol size. These characteristics are
typical of all of the the u_o/U_o data obtained in the experiments
conducted in this study.

One noticeable fact about Figure 12 is that the experimental
boundary layer profile has larger values of velocity at a given η than
does the numerically predicted velocity profile. This was true for all
of the cases studied. The reason for this was traced to the favorable
pressure gradient created by the growth of the boundary layer
displacement thickness in the constant cross-sectional area test
section.

A method of evaluating the pressure gradient was required for
correct numerical prediction of the boundary layer behavior. This
involved determining the pressure gradient for steady flow. This
pressure gradient was then assumed to be the mean pressure gradient for
oscillating flows. The Falkner-Skan equation [20] for the variation
with x of the freestream velocity in laminar steady flow with a pressure
gradient was used. This equation is

$$U(x) = K \, x^{\beta/(2-\beta)} \tag{10}$$

where K is a constant and β represents the strength of the pressure
gradient. The pressure gradient corresponding to the velocity
expression in Equation (10) is

$$\frac{dp}{dx} = -\rho \ K^2 \ \frac{\beta}{2-\beta} \ x^{(3\beta-2)/(2-\beta)} \qquad (10a)$$

If β is a positive number then a favorable pressure gradient is present and a negative β represents an adverse pressure gradient. The case of β = 0 corresponds to Blasius flow.

To estimate the value of β in the test section, the concept of δ^* and conservation of mass will be utilized. Since this is only an estimation, several assumptions will be made. These assumptions are listed below.

1. The equation for δ^* in Blasius flow can be applied. The expression for δ^* is given as [20],

$$\delta^* = 1.721x/\sqrt{Re_x} \qquad (11)$$

where $Re_x = U(0)x/\nu$. $U(0)$ was taken as 16 m/s which is the approximate velocity at the test section inlet for wave generator section configuration A, Table 2.

2. The origin of the boundary layer on the test section walls begins at the test section inlet and not in the entrance region.

3. The flow is incompressible.

Based on these assumptions, calculations were made for steady flow in test configuration TC II. Under these conditions, the freestream velocity was calculated to be 17.2 m/s at x = 0.22 m. This change in the freestream velocity is caused by a favorable pressure gradient with β = 0.098 as predicted by Equation (10).

It has been shown in the previous paragraph that a favorable steady pressure gradient should exist in the test section and the Falkner-Skan equation is a method of estimating it. The task now is to determine the value of β for the flow in each of the three test configurations. The mean pressure gradient for oscillating flows alters the shape of the mean velocity profile (it also affects the u_1/U_1 and ϕ_u profiles) so determining the correct β was accomplished by matching the experimental and numerical u_o/U_o velocity profiles. This simply means that β was varied in the numerical predictions until the predicted u_o/U_o profile provided a good representation for the experimental results. Extremely precise evaluation of β is not necessary since a small error in β will not drastically alter results predicted by the numerical code. This matching procedure is shown in Figure 13(a), (b) and (c) for the three test configurations TC I, TC II, and TC III, respectively. For TC I (Figure 13(a)) and TC II (Figure 13(b)), the value of β which best represents the experimental results is $\beta = 0.10$. The value of β which best represents the experimental results for TC III (Figure 13(c)) is 0.16. Interpolation was required for TC I and TC III since a limited number of numerical solutions were available. The values of β used to describe the mean pressure gradient for the three test configurations are tabulated in Table 3.

Now that values to describe the mean pressure gradient have been determined, the experimental results for the boundary layer survey cases given in Table 4 can be compared to the numerical predictions. The

Case A1
TC I
$\bar{u} = 0.45$
f = 10 Hz

o u_o/U_o, Measurement

————   β = 0   ⎫
—·—·—   β = 0.06 ⎬ Numerical
—— ——   β = 0.12 ⎭ Predictions
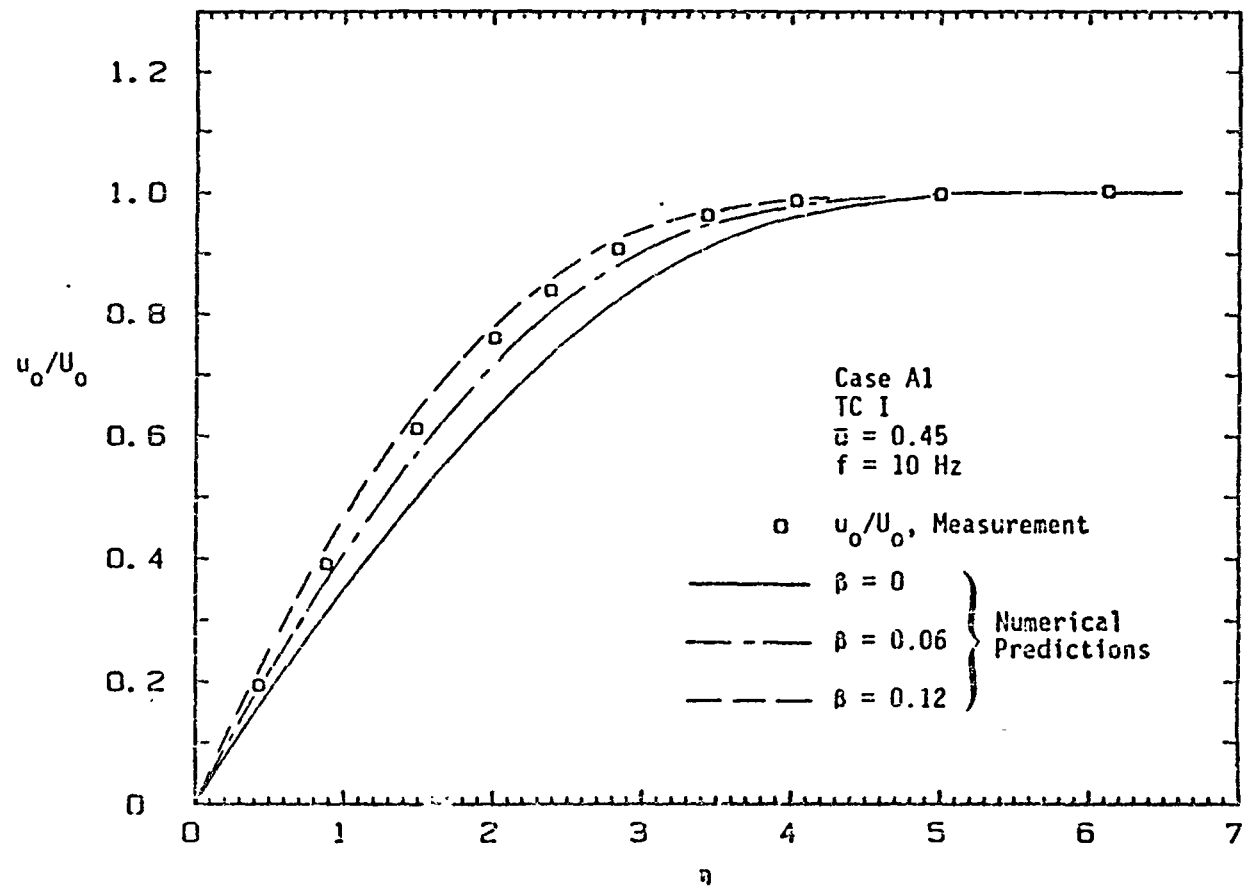
(a)   TC I

FIGURE 13.   Determination of the values of β which best represents the mean pressure gradients
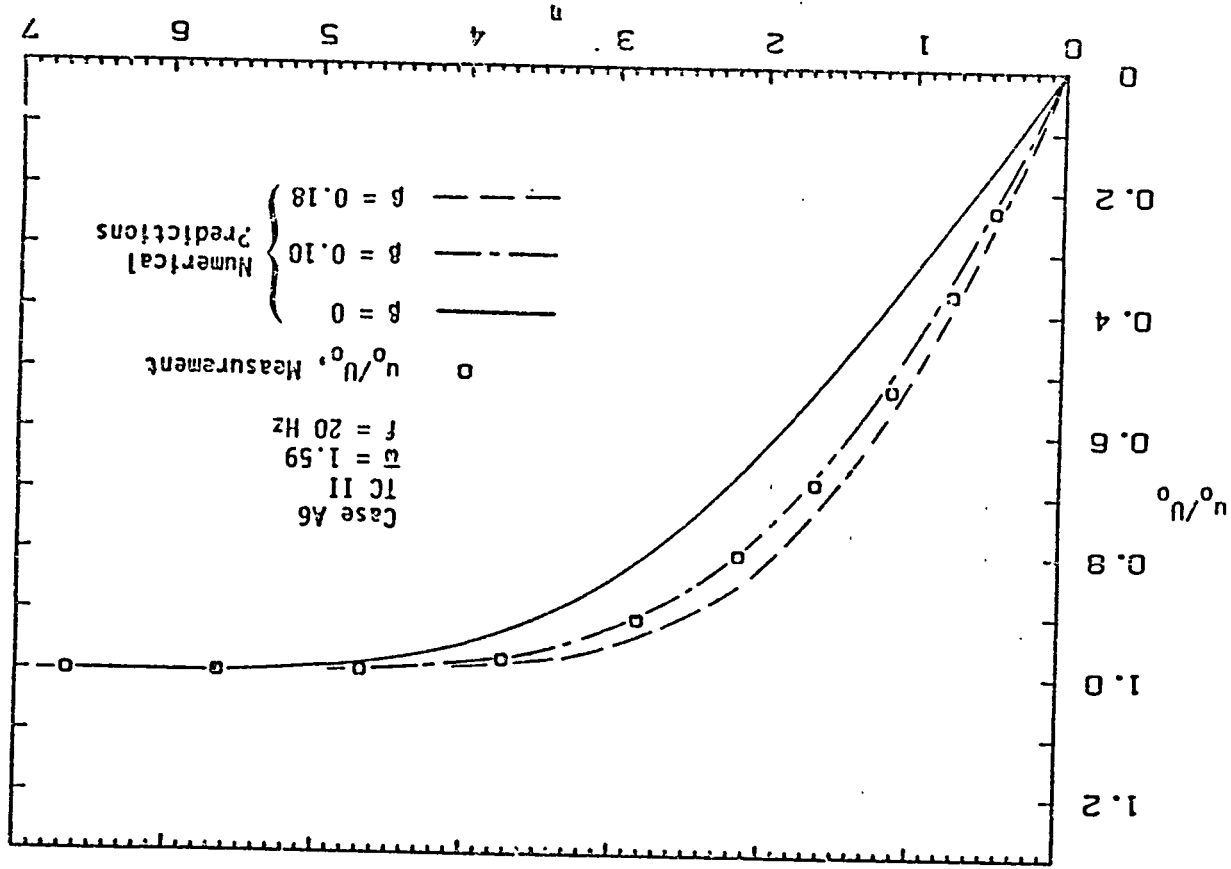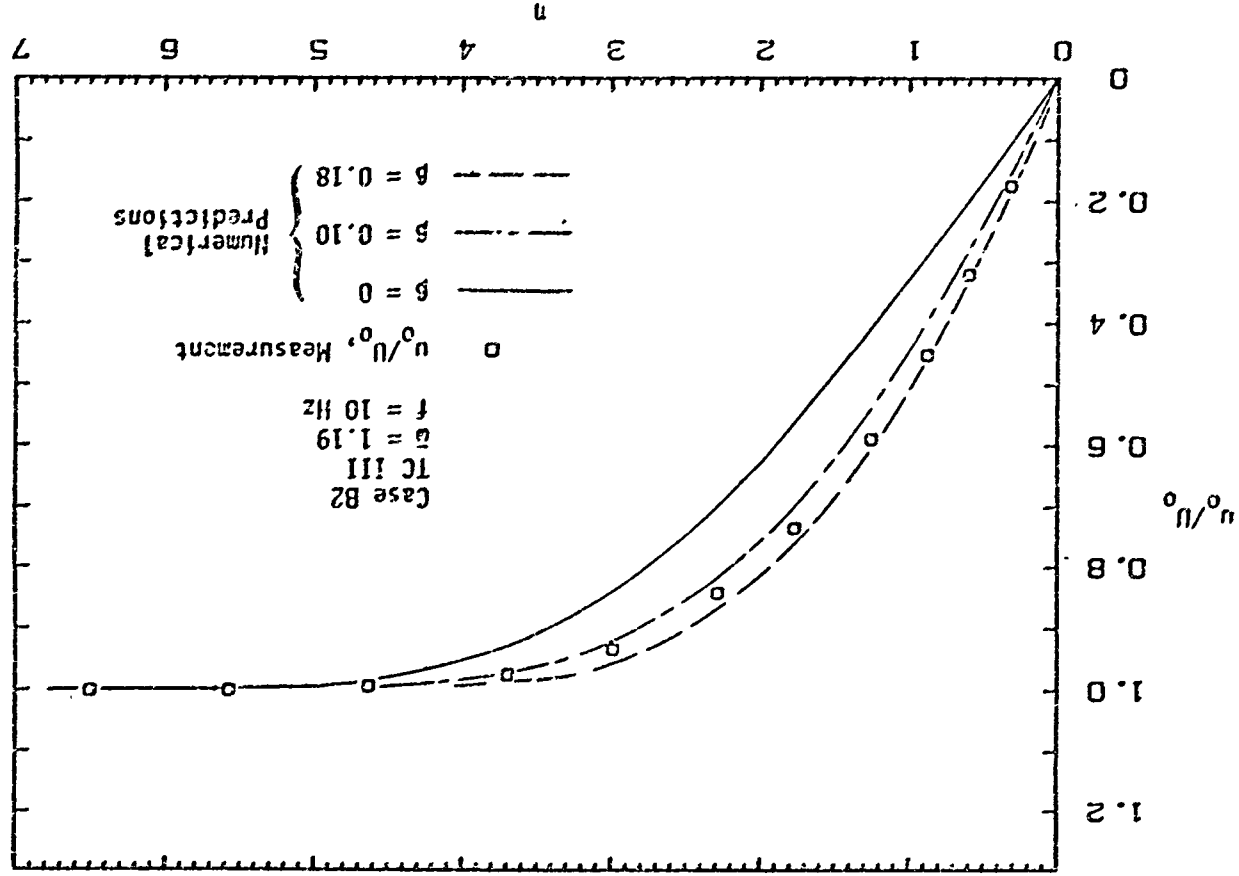
experimental results u_o/U_o, u_1/U_1, and ϕ_u vs η for the cases are given in Figure 14(a) through Figure 14(i) and are tabulated in Appendix A. Also plotted in these figures (with two exceptions) are the numerical solutions for the value of β which best represents the boundary layer behavior. The first exception is for case A1 (Figure 14(a)). The numerical predictions for $\beta = 0.12$ have been plotted since numerical results for this case were not available for $\beta = 0.10$. The second exception is for cases B1, B2, and B3 (Figure 14(g), (h), and (i)). Numerical solutions for $\beta = 0.16$ were not available so the numerical solution with the nearest available value of β ($\beta = 0.10$ or $\beta = 0.1S$) were plotted for comparison. Even though the numerical results in Figure 14(a), (g), (h), and (i) are not for the correct value of β, they give a good estimation of the predicted boundary layer behavior.

Measured values for the freestream mean velocity U_o and the freestream half-amplitude of velocity oscillations U_1 are listed in Appendix A for each case. The ratio U_1/U_c ranged between 0.134 and 0.220.

Comparison of the experimental u_o/U_o velocity profiles with the corresponding numerical solutions at appropriate values of β, shows that a good match for the complete profile was obtained for all the cases studied. As previously noted, one characteristic of oscillating flow, as described by previous studies [13,18], is that the mean velocity profile in oscillating flow matches the steady flow profile. Upon comparing the experimental oscillating flow results with the
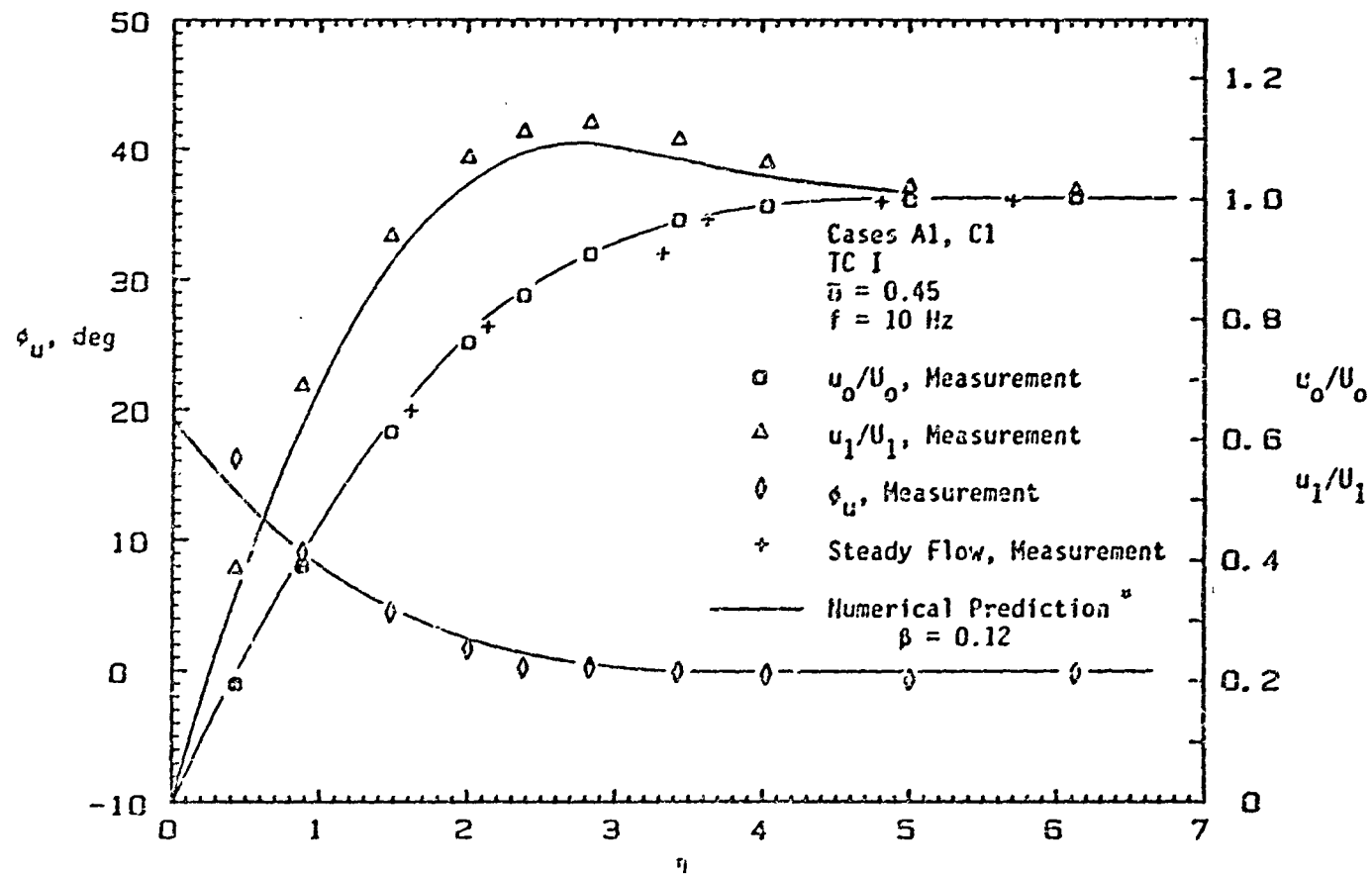
(a) Cases A1, C1 (* Required $\beta = 0.10$. $\beta = 0.12$ numerical prediction is the nearest available)

FIGURE 14. Results of the boundary layer surveys
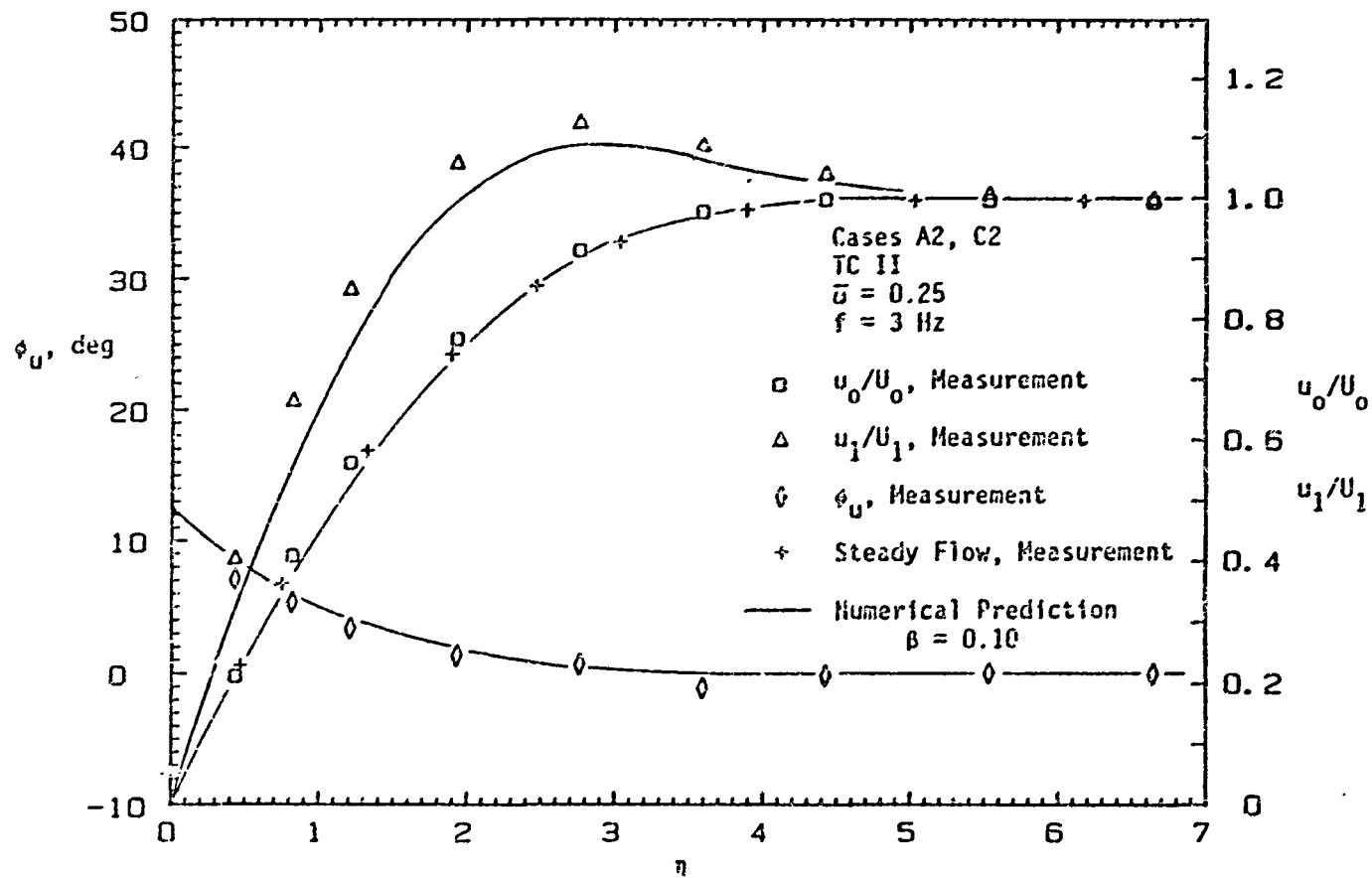
(b) Cases A2, C2

Figure 14. (Continued)
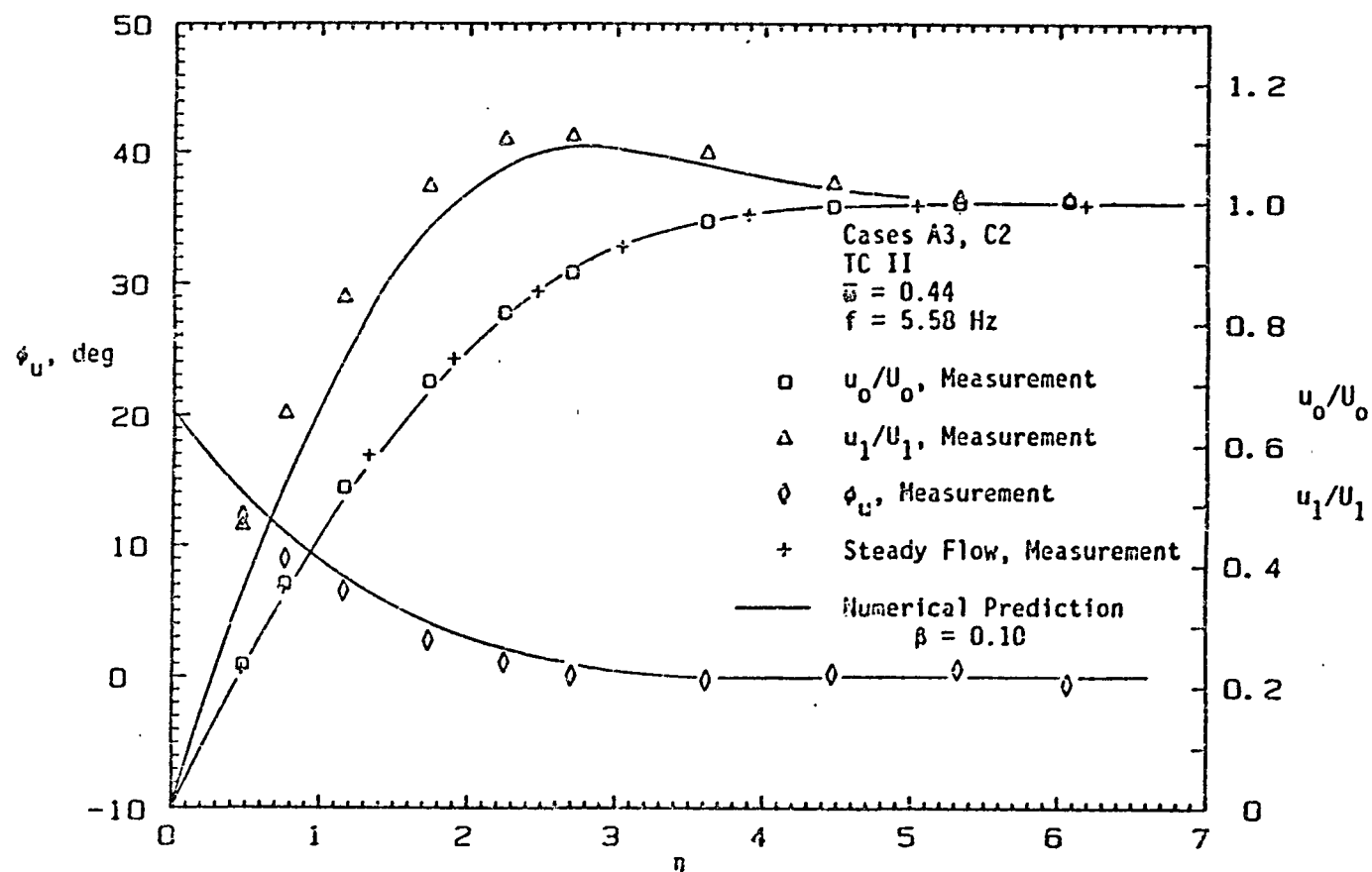
(c) Cases A3, C2

FIGURE 14. (Continued)
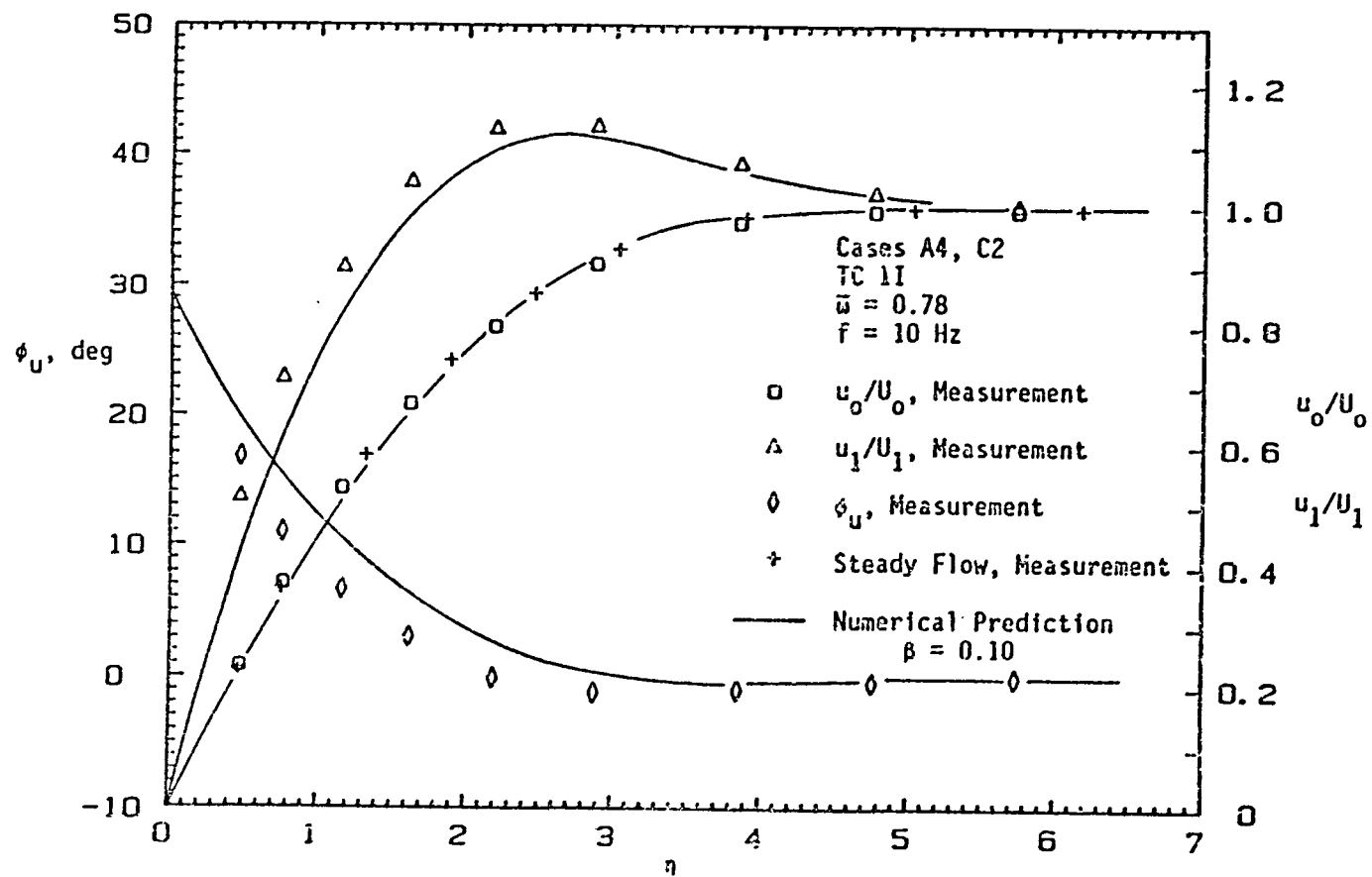
(d) Cases A4, C2

FIGURE 14. (Continued)

Cases A5, C2
TC II
$\bar{\omega} = 1.18$
$f = 15$ Hz

□ u_o/U_o, Measurement

△ u_1/U_1, Measurement

◊ ϕ_u, Measurement

+   Steady Flow, Measurement

——   Numerical Prediction
$\beta = 0.10$
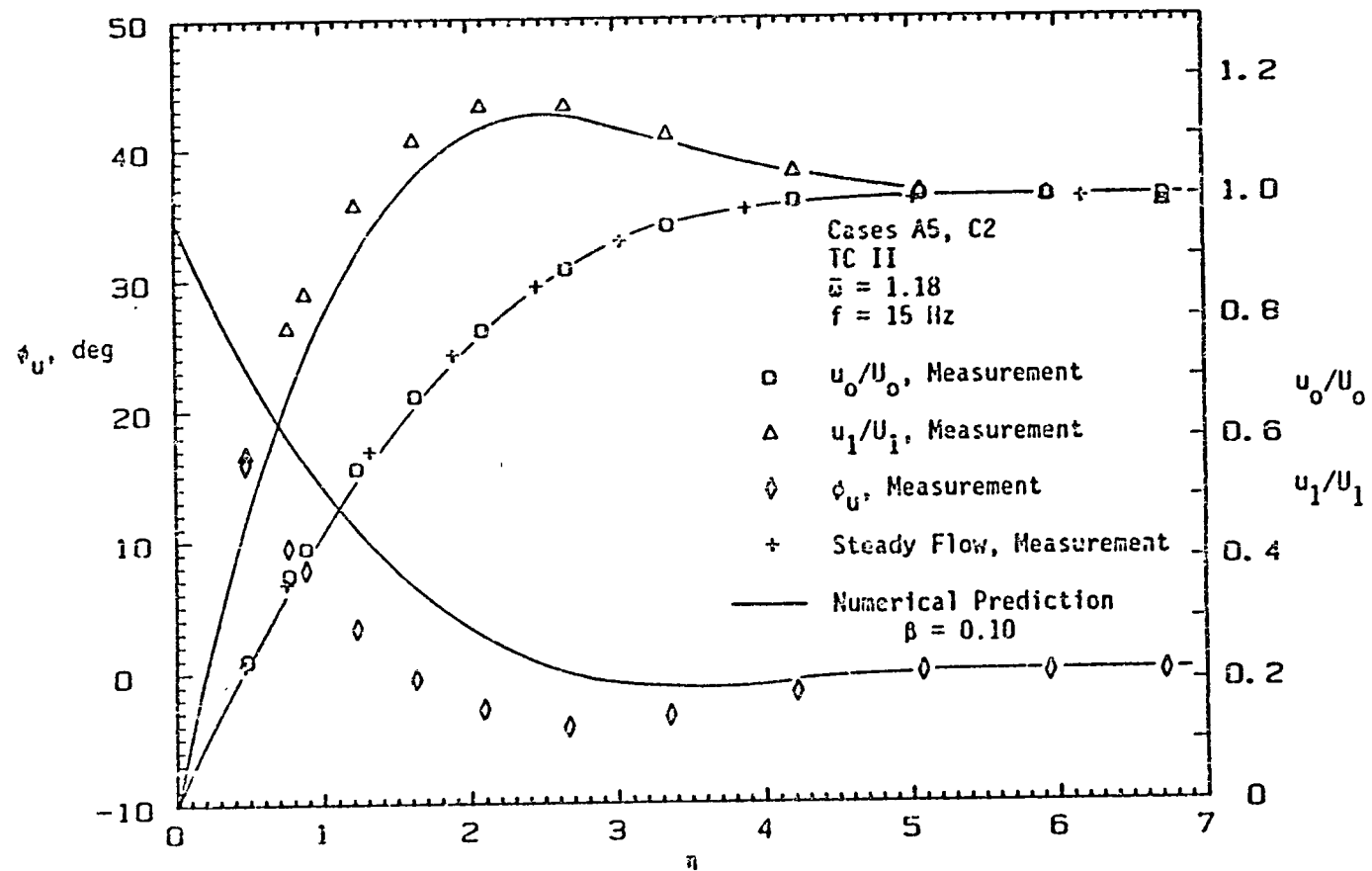
(e)   Cases A5, C2

FIGURE 14.   (Continued)
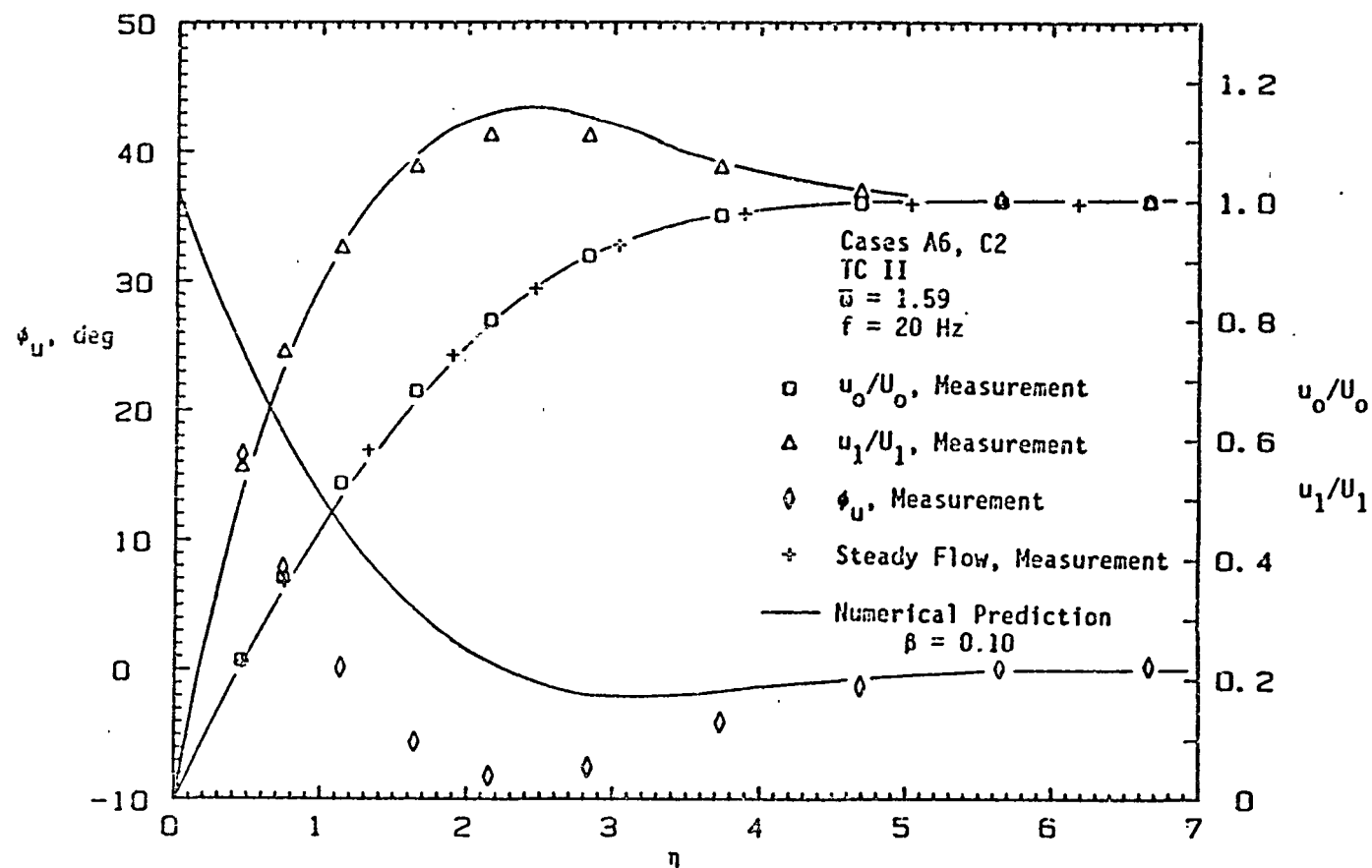
(f)   Cases A6, C2

FIGURE 14.   (Continued)
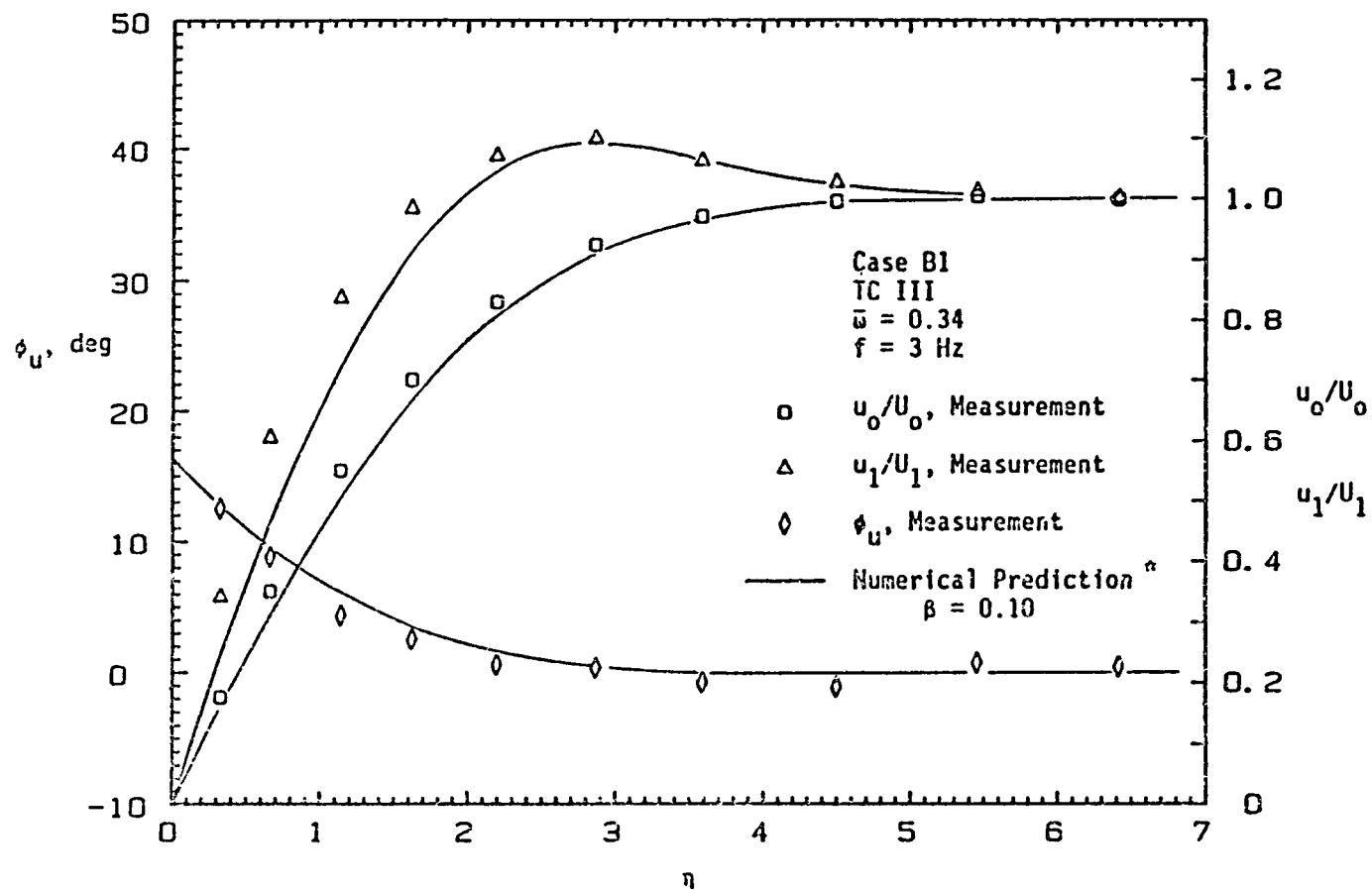
(g) Case B1 (* Required β = 0.16. β = 0.10 numerical prediction is
the nearest available)

FIGURE 14. (Continued)
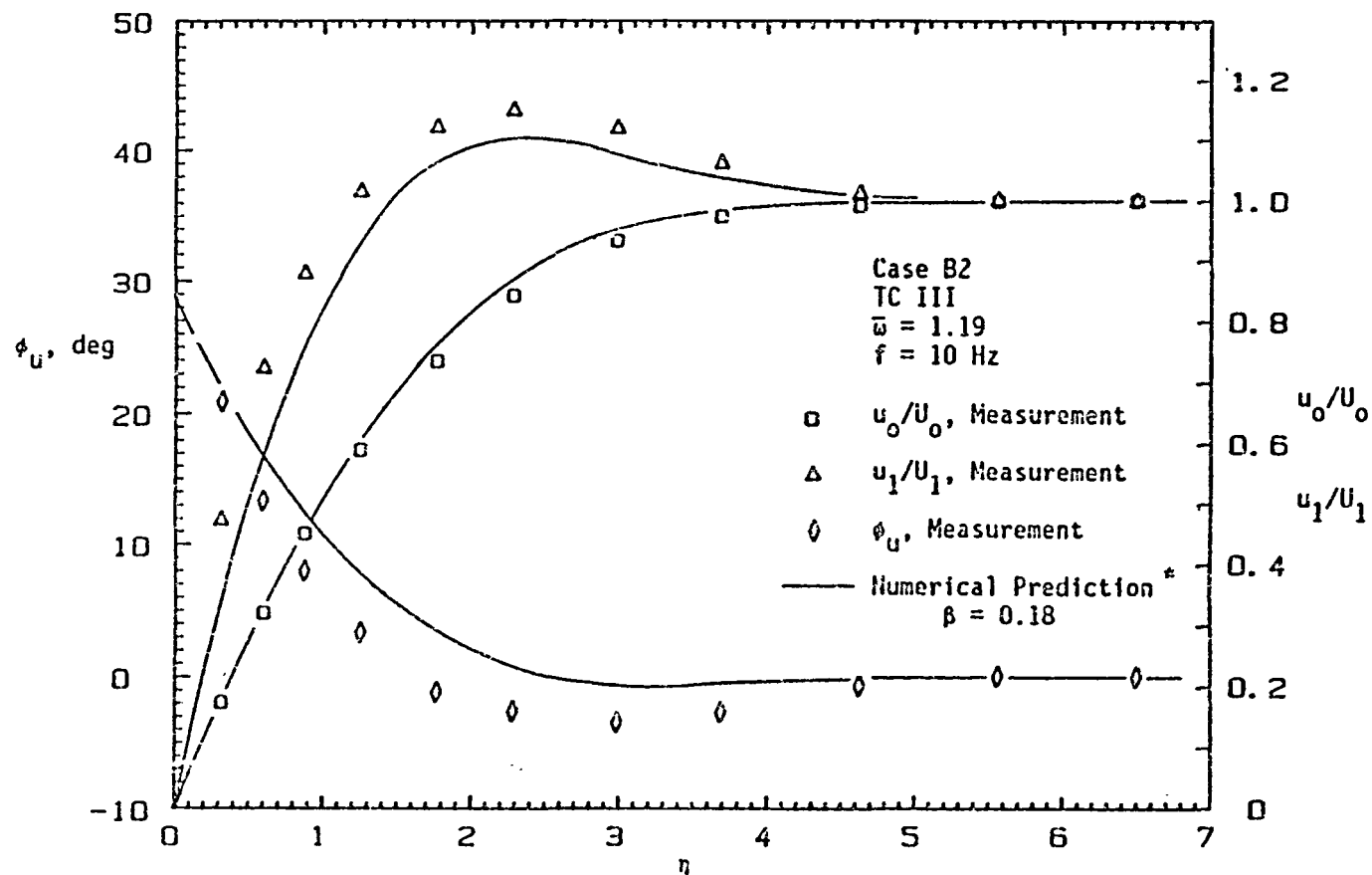
(h) Case B2 (* Required β = 0.16. β = 0.18 numerical prediction is the nearest available)
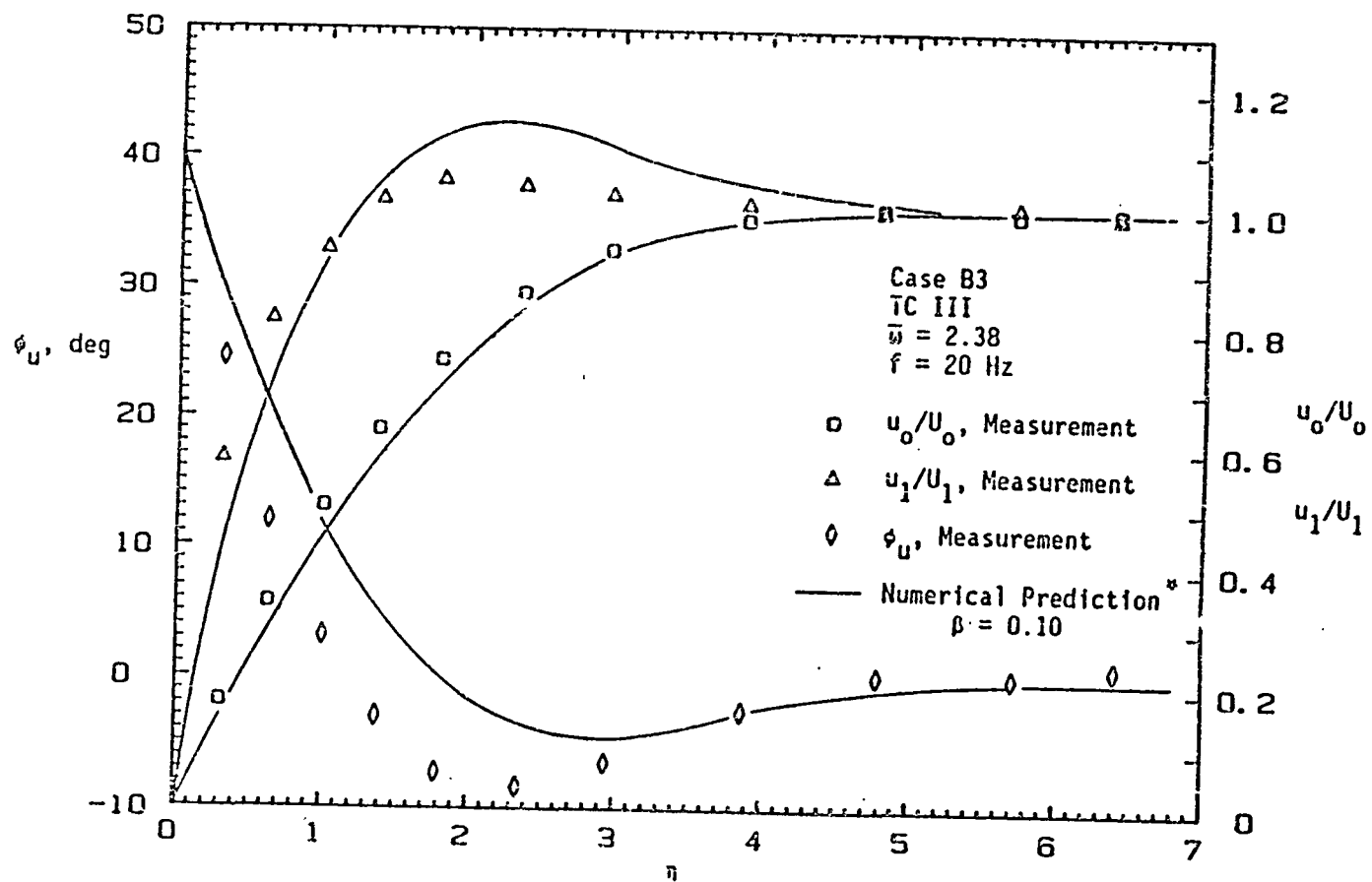
FIGURE 14. (Continued)

(i) Case B3 (* Required β = 0.16. β = 0.10 numerical prediction is the nearest available)

FIGURE 14. (Continued)

experimental steady flow results in Figure 14(a) through Figure 14(f), this characteristic was confirmed for the cases studied. Thus, the u_o/U_o profile is unaffected by the fluctuating velocity.

When the u_1/U_1 experimental profiles are compared to the numerical solutions a small difference is noted for most of the cases. For a given η, the experimental results exhibit larger values of u_1/U_1 than do the numerical solutions but the profile shapes are similar.

At low values of $\bar{\omega}$ (cases A1, A2, A3, B1), there is good agreement between the experimental and numerical results for ϕ_u over the entire boundary layer. At higher values of $\bar{\omega}$, the experimental results show that a larger velocity phase lag is present in the boundary layer than the numerical method predicts. There is some uncertainty in the ϕ_u measurements; it is estimated to be ± 1 degree. This uncertainty is slightly larger than symbol size in Figure 14.

The major question concerning the experimental ϕ_u data is related to the wall phase angle, since the objective for modeling the boundary layer behavior was to ensure within reasonable bounds that the predicted ϕ_τ was the same as the ϕ_τ actually present in the flows. Using the fact that the limit of ϕ_u as y approaches zero is equal to ϕ_τ, the numerical predictions of ϕ_τ in Figure 14(a) through Figure 14(i) are simply ϕ_u at $\eta = 0$. An estimation of ϕ_τ for the experimental results can be obtained by extrapolating the experimental ϕ_u data to the wall. Although there is some uncertainty in the values obtained, it is evident that for each case such an extrapolation yields a value of ϕ_τ close to the numerically

predicted value. Thus, the conclusion is reached that the numerically predicted values for ϕ_τ are reasonably accurate representations of ϕ_τ actually present in the flows.

B. Numerical Prediction of ϕ_τ

The purpose of this section is to determine the numerical prediction of ϕ_τ vs $\bar{\omega}$ for the two values of β corresponding to the three test configurations in Table 3. These results can then be used for comparison with the experimental measurements for ϕ_τ in a later chapter.

As previously mentioned, during the process of matching the experimental and numerical u_o/U_o velocity profiles, a series of numerical solutions at various values of β and $\bar{\omega}$ were obtained for the experimental cases studied in Table 4. The ratio U_1/U_o for the numerical computations for each case was determined from the experimental values of U_1 and U_o listed in Appendix A. Values for ϕ_τ from the series of numerical solutions are listed in Table 5. These results in the form of ϕ_τ vs β at constant $\bar{\omega}$ are plotted in Figure 15. Curves drawn through the data points in Figure 15 allow the prediction of ϕ_τ vs $\bar{\omega}$ for any value of β covered by the data. Curves of ϕ_τ vs $\bar{\omega}$ for the three test configurations can now be obtained. The curve of $\beta = 0$ will also be obtained for comparison. For the pressure gradient of $\beta = 0$ and $\beta = 0.10$, the values of ϕ_τ can be obtained from Figure 15 or taken directly from the Table 5, but for $\beta = 0.16$ the values of ϕ_τ must be obtained from the curves in Figure 15. These results have been

plotted in Figure 16. It is evident from Figure 15 and Figure 16 that a favorable mean pressure gradient decreases the wall phase angle for a given $\bar{\omega}$ over the range of β covered.

Now that the numerical predictions of ϕ_τ have been obtained, the remaining chapters will concentrate on measuring ϕ_τ with hot element gauges and comparing the experimental results to the numerical predictions.

TABLE 5. Numerical predictions of ϕ_τ in degrees for various values of β

EXPERIMENTAL CASE MODELED	TEST CONFIG.	$\bar{\omega}^2$[a]	β				
			0.0	0.06	0.10	0.12	0.18
A1	TC I	0.45	32.5	24.1		19.1	15.8
A2	TC II	0.24	22.7	14.8	12.5	11.7	9.9
A3	TC II	0.44	31.3	24.1	20.2		
A4	TC II	0.79	40.0	32.9	29.2		
A5	TC II	1.19	41.0	37.0	34.6		
A6	TC II	1.58	43.1	39.1	37.0	36.2	33.4
B1	TC III	0.34	28.4	19.5	16.2		
B2	TC III	1.13	40.3		33.6		28.9
B3	TC III	2.26	45.8		39.8		

[a]These values of $\bar{\omega}$ are based on nominal velocity values listed in Table 2. Thus, the $\bar{\omega}$ values differ slightly from the corresponding values listed in Table 4.
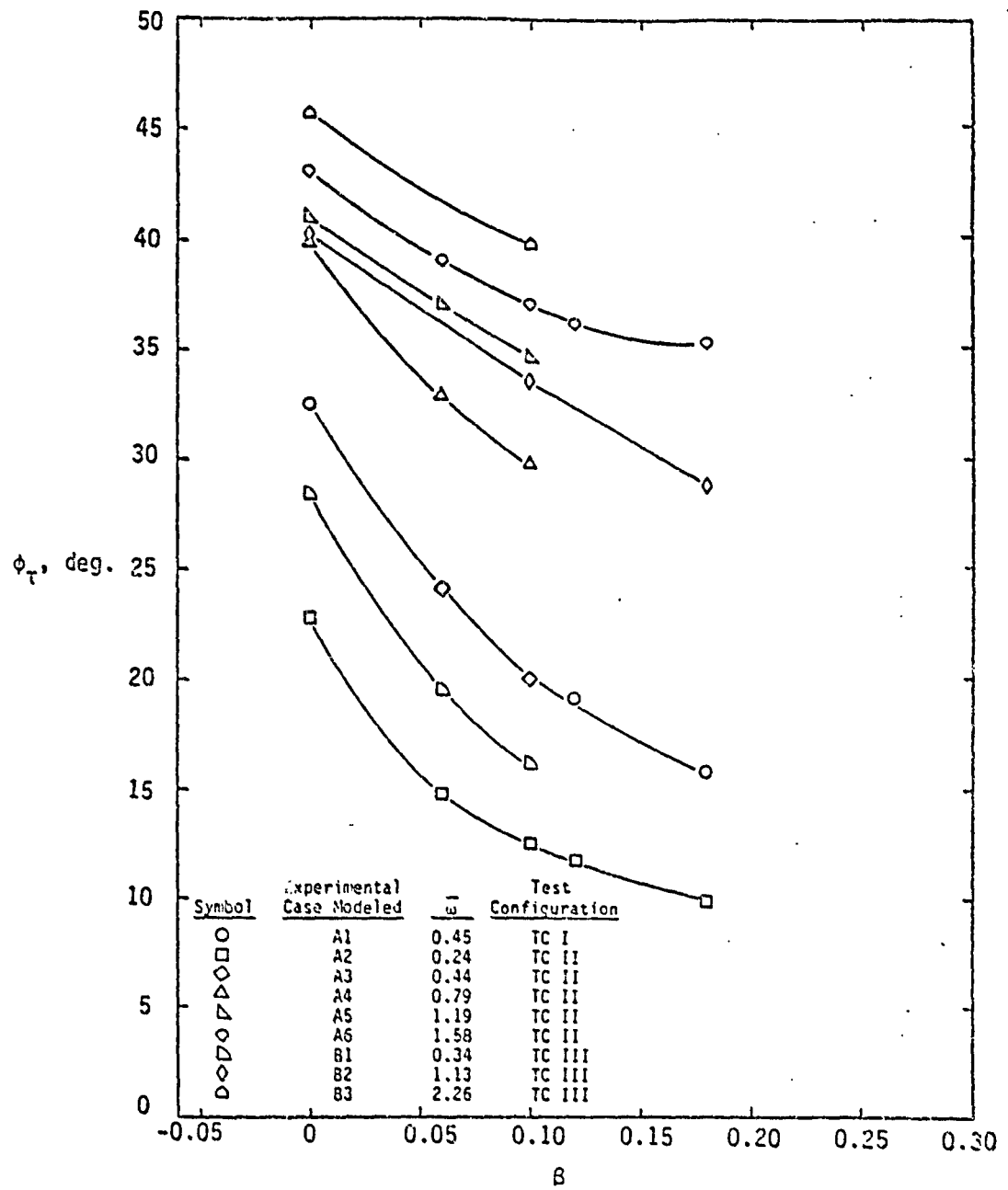
FIGURE 15. Numerical results of ϕ_τ vs β
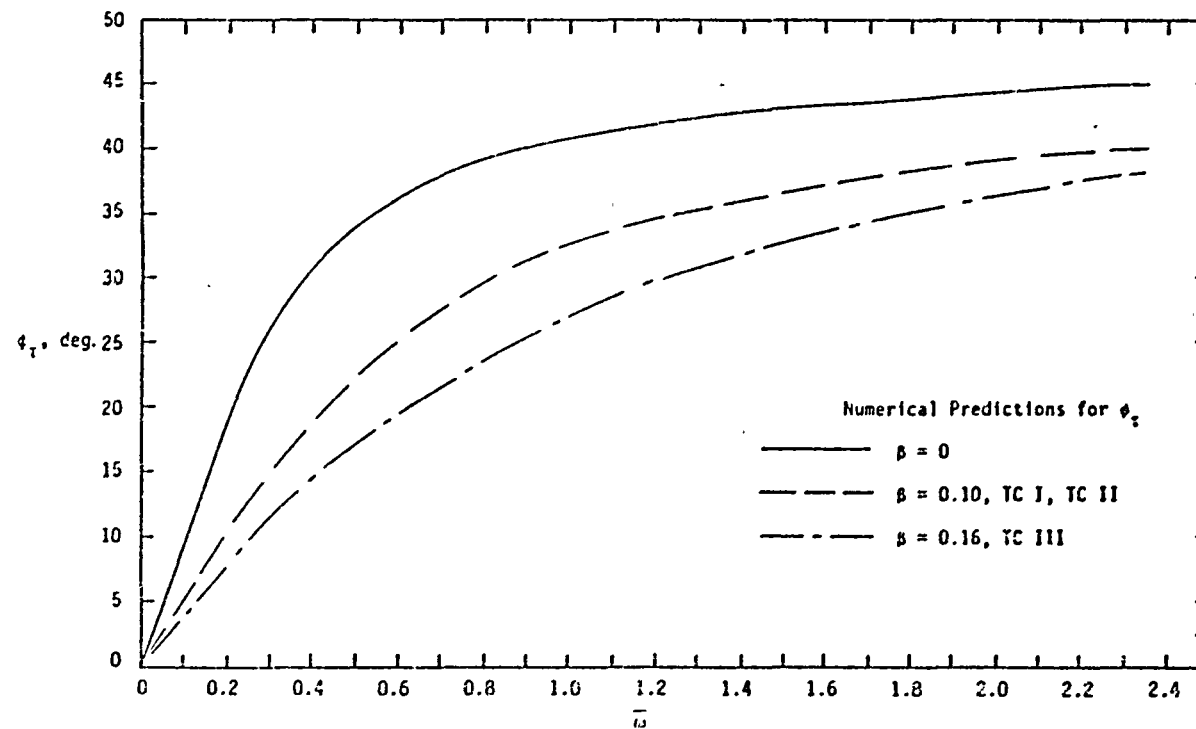
FIGURE 16. Numerical results of ϕ_τ vs $\bar{\omega}$ for test configurations TC I, TC II, and TC III

VI. DATA AQUISITION SYSTEM AND GAUGES FOR ϕ_τ MEASUREMENTS

This section describes the data aquisition system and gauges used to measure the wall shear stress phase angle ϕ_τ. Considerable time and effort was expended in determining a reliable method for measuring this quantity. Figure 17 describes the data acquisition system used. A Disa P14 hot wire probe in the freestream served as a reference. The freestream reference hot wire and hot element gauges were powered by a Disa single channel anemometer unit, the output signal of which was amplified and filtered by a Tektronix Model 3A10 transducer amplifier. The signal was then converted from analog to digital form by the A/D voltmeter and sent to the computer for processing.

Two types of flush mounted hot element gauges were used in this study and are described in Table 6. Each substrate element was contained in a 3.175 mm diameter stainless steel tube. One type of gauge used was the TSI model 1237 AU hot film gauge. This type is commercially available and consists of a thin platinum film deposited on a quartz substrate. The other type of gauge used was built by the Instruments Branch of the NASA Ames Research Center. This gauge contained a 10 μm wire buried flush with the surface of a polystyrene substrate. Buried wire gauges are described by Murthy and Rose [21]. Four gauges, two of each type, were used.

Mounting the hot element gauges was accomplished by passing them through the bottom of the test section and a hole in the flat plate. A flush fit with the top surface of the plate was obtained by visual

Hewlett
Packard
6296A DC
Power Supply

External trigger,
one per cycle

Signal from
hot wire
probe or
hot element
gauge

DISA Type 55D01
Anemometer
Main Unit

Tektronix 3A10
Transducer
Amplifier

Hewlett
Packard 3437A
A/D
Voltmeter

Commodore
Computer
System,
Machine
Language
Programmed

Oscilloscope

Probe positioning
mechanism

Test section
wall

DISA P14 Single-wire probe

Flow

Flat plate

Hot element gauge

FIGURE 17.   Data aquisition system for measuring ϕ_τ

68

TABLE 6. Hot element gauges tested (see Figure 4)

Designation	Type	Manufacture	Element L x W (mm)	Substrate	Substrate Diameter, mm
PF1	Platinum Film	TSI 1237 AU	1.000 x 0.152	Quartz	2.686
PF2	Platinum Film	TSI 1237 AU	1.000 x 0.152	Quartz	2.686
FW1	Flush Wire	NASA ARC[a]	1.753 x 0.010	Polystyrene	2.362
FW2	Flush Wire	NASA ARC	1.753 x 0.010	Polystyrene	2.362

[a]Instrument Branch of NASA Ames Research Center.

inspection using a low power magnifying glass. The orientation of the hot element was such that the longest dimension was perpendicular to the flow. See Figure 4.

A hot element gauge produces a signal with a large DC component on which is superposed a small oscillating component. Due to the small oscillating component it was necessary to use a virtually noise-free DC power supply to operate the constant temperature anemometer which powered both the hot element and hot wire probes. Since the DC component of the signal was not needed to determine the phase angle for either the freestream reference or the wall measurement, the Tektronix 3A10 transducer amplifier was AC coupled. This eliminated the DC component and resulted in a signal oscillating about a zero mean voltage. It was also necessary to amplify the oscillating signal to obtain an accurate measurement.

The same procedure for obtaining 20 ensemble averaged voltage readings per cycle as previously described for hot wire velocity measurements was used, but for this part of the study the 20 points contained both positive and negative voltages. A requirement of the fourier analysis was that all the voltages be positive, so a constant fictitious voltage was added to the 20 voltage values. The sum of the gauge voltage and the fictitious voltage will be referred to as the relative gauge output rather than voltage. Fitting a cosine wave to the 20 ensemble averaged relative gauge output values and an appropriate accounting of the freestream phase angle reference results in an equation of the same form as Equation (3). However, the values for τ_o and τ_1 are meaningless and only ϕ_τ has significance.

Now that a brief description has been given of how ϕ_τ was measured, the remaining part of this chapter will be devoted to describing some of the problems encountered and the steps taken to ensure that the errors in measuring ϕ_τ were minimized. One of these problems was to determine if the fourier analysis produced the correct value of ϕ_τ for given input information since the anemometer output signal was not linear with respect to the input signal. The freestream velocity present in the test section is sinusoidal, but the hot element or hot wire signal out of the anemometer main unit and Tektronix 3A10 transducer amplifier is not. This is due to the nonlinear relationship between the input and output signal which governs the operation of the anemometer. A linearizer was not used in conjunction with the small signals from the

hot element gauges because of electrical noise inherent to the instrument. Figure 18(a) shows an oscilioscope record of the nonlinear signal produced by a TSI gauge. Figure 18(b) shows the 20 ensemble averaged relative gauge output values and the cosine wave fit to the signal in Figure 18(a). Figure 18(b) illustrates the fact that the 20 ensemble averaged relative gauge output values do not directly fall on the cosine wave fit, but they do symmetrically fit it. It is because of this symmetry that the correct phase angle is measured. To experimentally prove that the correct phase angle is measured using a nonlinear signal, a comparison was made between the phase angles measured using a linear and nonlinear signal from a hot wire in the freestream. The nonlinear signal was obtained by using the instrumentation described in Figure 17 while the linear signal was obtained by using the same instrumentation but adding a Disa type 55D10 linearizer in series between the anemometer and the Tektronix 3A10 transducer amplifier. Three runs were taken using each instrumentation arrangement and the average of the three resulting phase angles was calculated. The difference between the average phase angles for the linear and nonlinear signals was less than one degree.

To eliminate the error caused by a phase shift within the data aquisition system, exactly the same experimental setup was used to process both the hot wire freestream reference and hot element gauge signals. Thus, any phase shift within the instrumentation system would not affect the value of ϕ_τ. This statement is true only if changes in
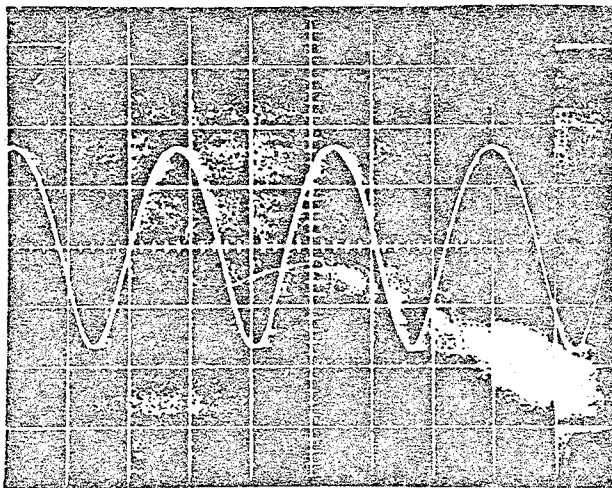
PF1
TC II
CRR = 1.18
f = 20 Hz

(a) Oscilloscope record of a hot element signal

FIGURE 18. Description of a hot element signal

PF1
TC II
f = 20 HZ
ORR = 1.18

* Ensemble-averaged experimental values
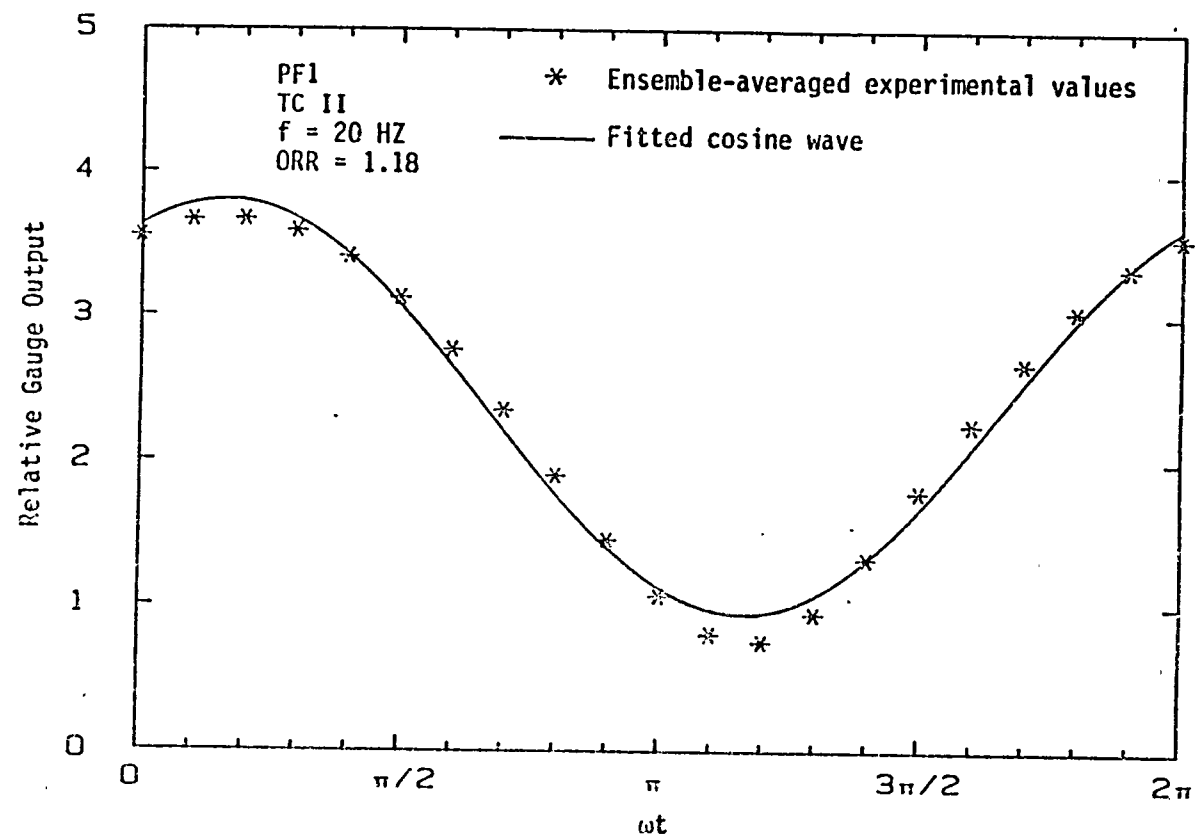
——— Fitted cosine wave

(b) Cosine wave fit to the 20 ensemble averaged relative
gauge output values

FIGURE 18. (Continued)

dial settings when switching from the freestream reference hot wire probe to the hot element gauge has no effect. There were several dial settings changed when switching between the freestream hot wire and the hot element gauges took place. Consequently, the effect of these changes on the phase angle measured needed to be investigated. The settings changed on the anemometer main unit were the capacitance and inductance settings required to stabilize the bridge and provide optimum frequency response. Only the amplification setting was altered on the Tektronix 3A10 amplifier. Gain settings of approximately 10 and 30 were required for the hot wire and hot element gauges respectively. Various gain settings were needed due to the difference in magnitude of the signal produced by the hot element and hot wire probes. Testing was done by changing dial settings one at a time, within reasonable limits, and observing the effect on the phase angle measured. Both the hot wire reference and the hot element gauges were used for these tests. Since the effect of ORR of the hot element gauges was one of the quantities to be varied in the hot element gauge response study, ORR was not changed during these tests. Upon completion of these tests, it was determined that these dial settings have no affect on the phase angle measured.

The effect of the ORR on the hot element gauges will be addressed in the next chapter. For this study, the ORR for the hot element gauges were varied over the range $1.02 \leq ORR \leq 1.33$. The ORR is a measure of the temperature at which the gauge operates at, with a higher ORR corresponding to a higher operating temperature. The upper limit was

estimated from information supplied with the TSI gauges. This range for the ORR was also applied to the flush wire gauges. However, values near the upper limit resulted in premature failure of the flush wire gauges. No problems were observed with the TSI gauges.

The Tektronix 5A10 amplifier has a low pass filter which was set at 100 Hz. Even though the filter setting was not changed when switching gauges, it was desired to determine if this setting eliminated any frequencies required for an accurate measurement of ϕ_τ. For this comparison, two filter settings were chosen 100 Hz and 10 kHz. When the ϕ_τ measurement for each setting was compared, the difference was negligible.

Tests showed that the protrusion or recession of the hot element gauges relative to the plate surface will alter the phase angle measured. Determining the change in the measured phase angle for a given change in gauge height is difficult and was not attempted in this study, but a TSI gauge was intentionally placed slightly above and below the plate surface to determine the influence of surface mismatch. This resulted in a change in ϕ_τ of several degrees. Consequently, extreme care was taken to mount the gauges flush with the top surface of the flat plate.

Several runs to measure ϕ_τ were made using a platinum film gauge with the longest dimension of the hot element oriented parallel to the flow (90 degrees to that shown in Figure 4). The average of the results for ϕ_τ from these runs was 8 degrees smaller than for the perpendicular

orientation. This indicated a rather pronounced sensitivity to hot element orientation. As a result, caution was exercised to ensure that the hot element orientation was 90 degrees to the flow direction each time a gauge was installed for testing.

To ensure that changes in the room temperature and pressure had as little effect as possible on measuring ϕ_τ, the freestream reference phase angle was obtained the same day as the corresponding wall measurements. Each freestream reference angle was taken as the average of 3 runs.

VII. RESULTS FOR ϕ_τ MEASUREMENTS

Results of the experimentally measured wall shear stress phase angle will be presented in this section. In addition, the experimental results will be compared to the numerical predictions.

As previously mentioned, two types of gauges were used to measure ϕ_τ. These are the hot film gauges produced by TSI and the buried wire gauges supplied by NASA Ames Research Center. Two gauges were used from each type for a total of four which enabled comparison between similar gauges and also between the two different types. There were no distinguishing features between the buried wire gauges but there was among the hot film gauges. PF1 (see gauge designation in Table 6) did not have the protective alumina covering over the platinum film that PF2 had. The absence of this covering will be discussed later in this chapter.

Preliminary tests revealed that the ORR affects the signal quality and amplitude of the voltage produced by the gauges. Increasing the ORR causes an increase in voltage and the signal quality is also improved up to an ORR of approximately 1.08. To illustrate the change in quality and amplitude of the signal, oscilloscope records at three values of ORR 1.02, 1.06, and 1.12 are shown in Figure 19. These pictures are typical of the response of all four gauges at all frequencies tested.

A list of the cases that were studied and a summary of the results is given in Table 7. Detailed results for the cases are tabulated in Appendix B. Each case contains the results for ϕ_τ vs ORR for a given

78

PF2
TC II
ORR = 1.02
f = 20 Hz

PF2
TC II
ORR = 1.06
f = 20 Hz

PF2
TC II
RR = 1.12
f = 20 Hz
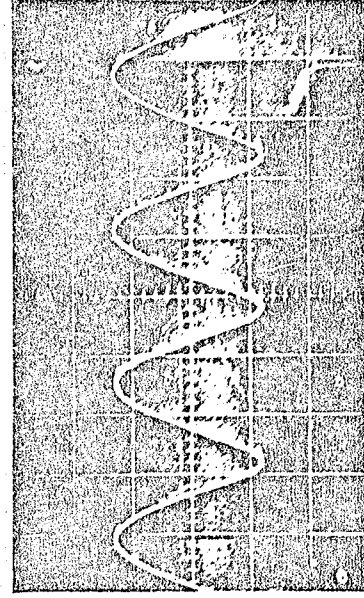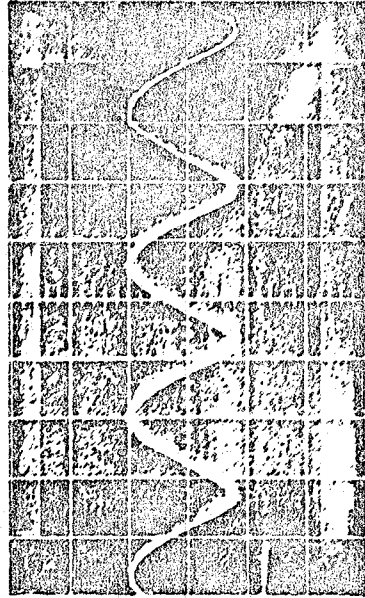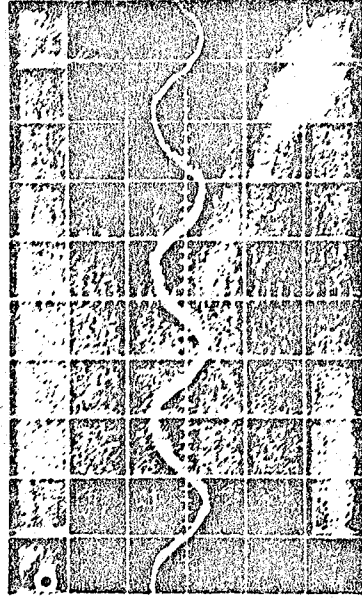
FIGURE 19. Oscilloscope records of a hot element output signal at three values of ORR

gauge, frequency, and test configuration. When calculating $\bar{u}$, only two values of U_o were used. These corresponded to the two wave generator section configurations (Table 2) and were 16.7 m/s for wave generator section configuration A and 11.7 m/s for wave generator section configuration B. This was required since the exact U_o was not measured the day each case was obtained, but the error introduced is not expected to be large since U_o remains relatively constant.

The results for the cases in Table 7 as tabulated in Appendix B are plotted in Figure 20(a) through Figure 20(d). Each data point in these figures represents a single run. The uncertainty in the measurements was estimated to be $\pm$ 1 degree. It is evident from these figures that the ORR affects the phase angle measured by both types of hot element gauges. For most of the cases, ϕ_τ increases with ORR until the ORR reaches about 1.15, after which ϕ_τ tends to remain constant as ORR increases. There are evident exceptions to this pattern. Because the wall phase angle measured by the gauges tends to become independent of ORR for high values, on average ϕ_τ for high ORR may be determined. This was accomplished by drawing curves through the experimental results. Once the curves were established, ϕ_τ for each case was determined from the flat portion of the curve where the measured phase angle is independent of ORR. If the curve was not flat the ϕ_τ was obtained at ORR = 1.30. Using the above method, the values of ϕ_τ at high ORR for all cases have been tabulated in Table 7.

TABLE 7. Experimental ϕ_r cases studied

CASE	TEST CONFIGURATION	f,Hz	$\bar{\omega}$	ϕ_r,deg[a]	$(\phi_{rn} - \phi_{ro})$[b]
PF1 A	TC I	10.00	0.45	15.3	5.2
PF1 B	TC II	20.00	1.66	25.8	11.6
PF2 A	TC I	3.00	0.14	-0.8	8.1
PF2 B	TC I	5.00	0.23	3.6	8.4
PF2 C	TC I	5.00	0.23	4.8	7.2
PF2 D	TC I	7.00	0.32	10.8	4.9
PF2 E	TC I	10.00	0.45	13.3	7.2
PF2 F	TC I	10.00	0.45	16.2	4.3
PF2 G	TC I	20.00	0.90	18.2	13.0
PF2 H	TC II	3.00	0.25	4.4	8.4
PF2 I	TC II	5.45	0.45	12.4	8.1
PF2 J	TC II	5.45	0.45	12.4	8.1
PF2 K	TC II	7.00	0.58	15.3	9.1
PF2 L	TC II	10.00	0.83	18.9	11.1
PF2 M	TC II	10.90	0.90	22.0	9.2
PF2 N	TC II	20.00	1.66	24.9	12.5
PF2 O	TC II	20.00	1.66	24.9	12.5
PF2 P	TC III	3.00	0.35	7.0	6.3
PF2 Q	TC III	10.00	1.18	17.9	11.7
PF2 R	TC III	20.00	2.36	22.0	16.5
FW1 A	TC I	5.00	0.23	-5.5	17.5
FW1 B	TC I	10.00	0.45	9.5	11.0
FW1 C	TC I	20.00	0.90	17.3	13.9
FW2 A	TC I	3.00	0.14	-3.2	10.5
FW2 B	TC I	5.00	0.23	-2.5	14.3
FW2 C	TC I	7.00	0.32	4.3	11.4
FW2 D	TC I	10.00	0.45	10.4	10.1

[a] ϕ_r was obtained from the curves in Figure 20 at ORR = 1.30.

[b] The difference between the numerical curves and the experimental data points in Figure 21.
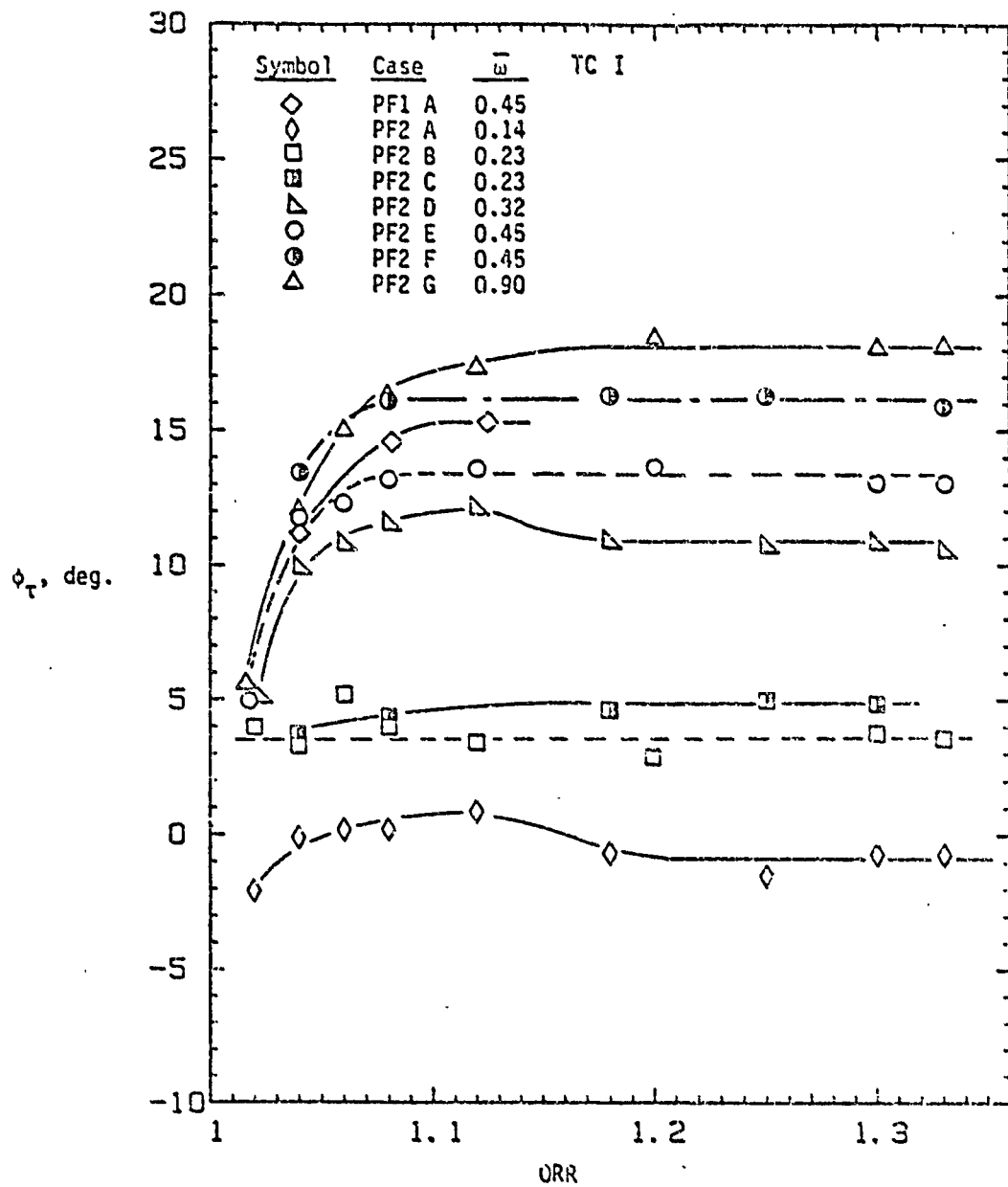
(a) Results for PF1 and PF2 gauges for TC I

FIGURE 20. Experimental results for ϕ_τ vs ORR

Symbol	Case	$\bar{\omega}$	TC II
◇	PF1 B	1.66	
◇	PF2 H	0.25	
⬥	PF2 I	0.45	
△	PF2 J	0.45	
◊	PF2 K	0.58	
○	PF2 L	0.83	
△	PF2 M	0.90	
△	PF2 N	1.66	
▲	PF2 O	1.66	
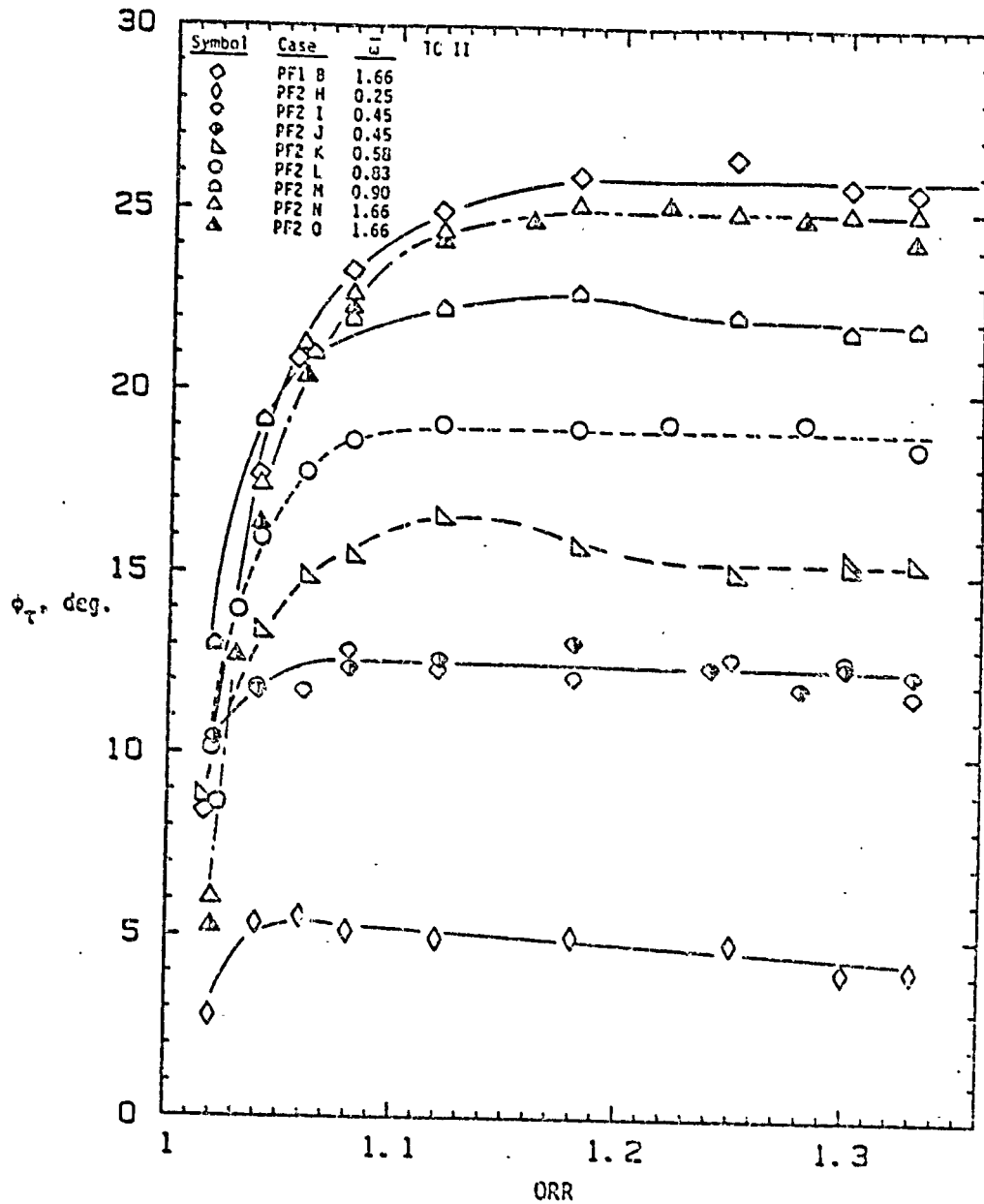
(b)   Results for PF1 and PF2 gauges for TC II

FIGURE 20.   (Continued)
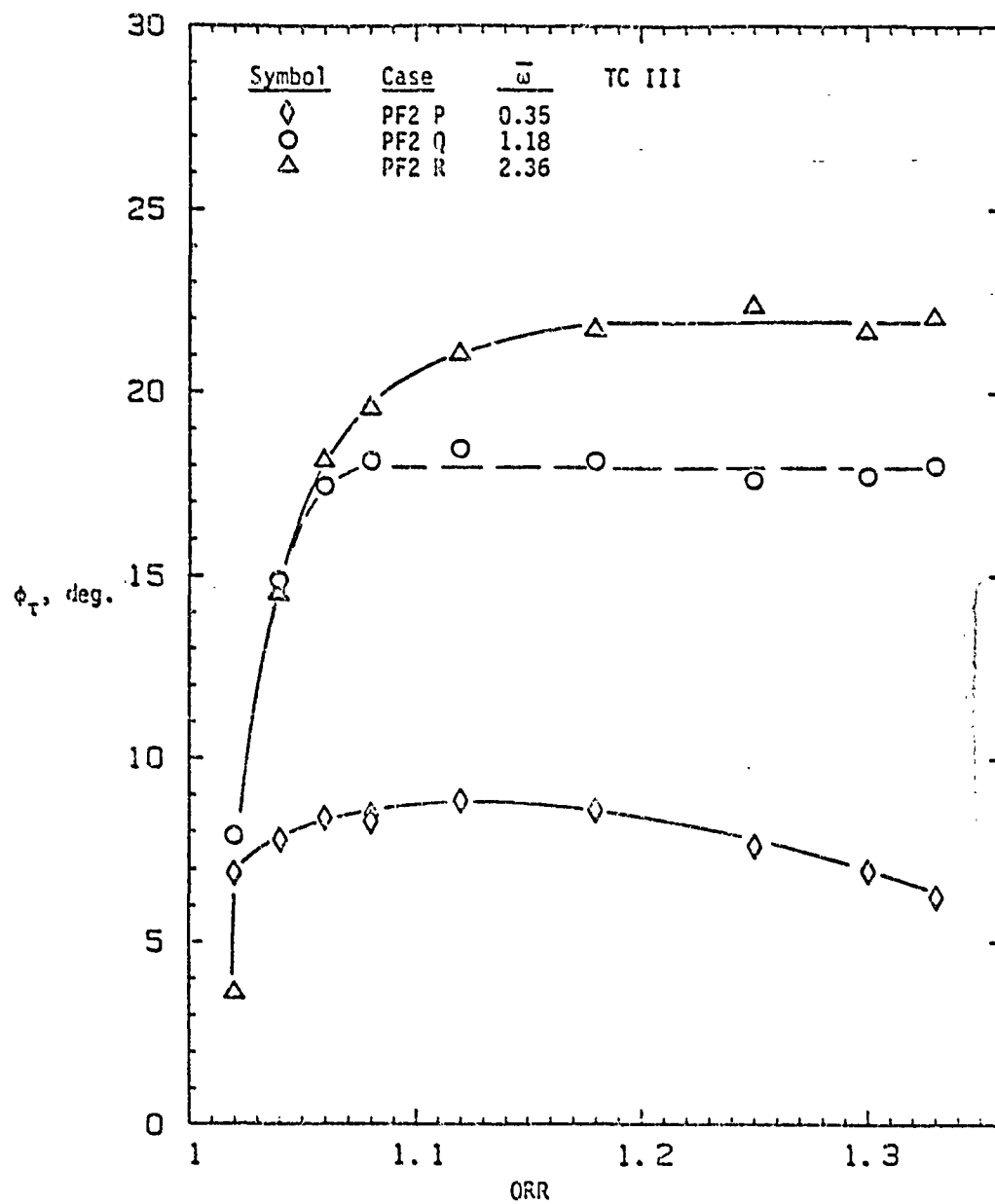
(c) Results for PF2 gauge for TC III

FIGURE 20. (Continued)
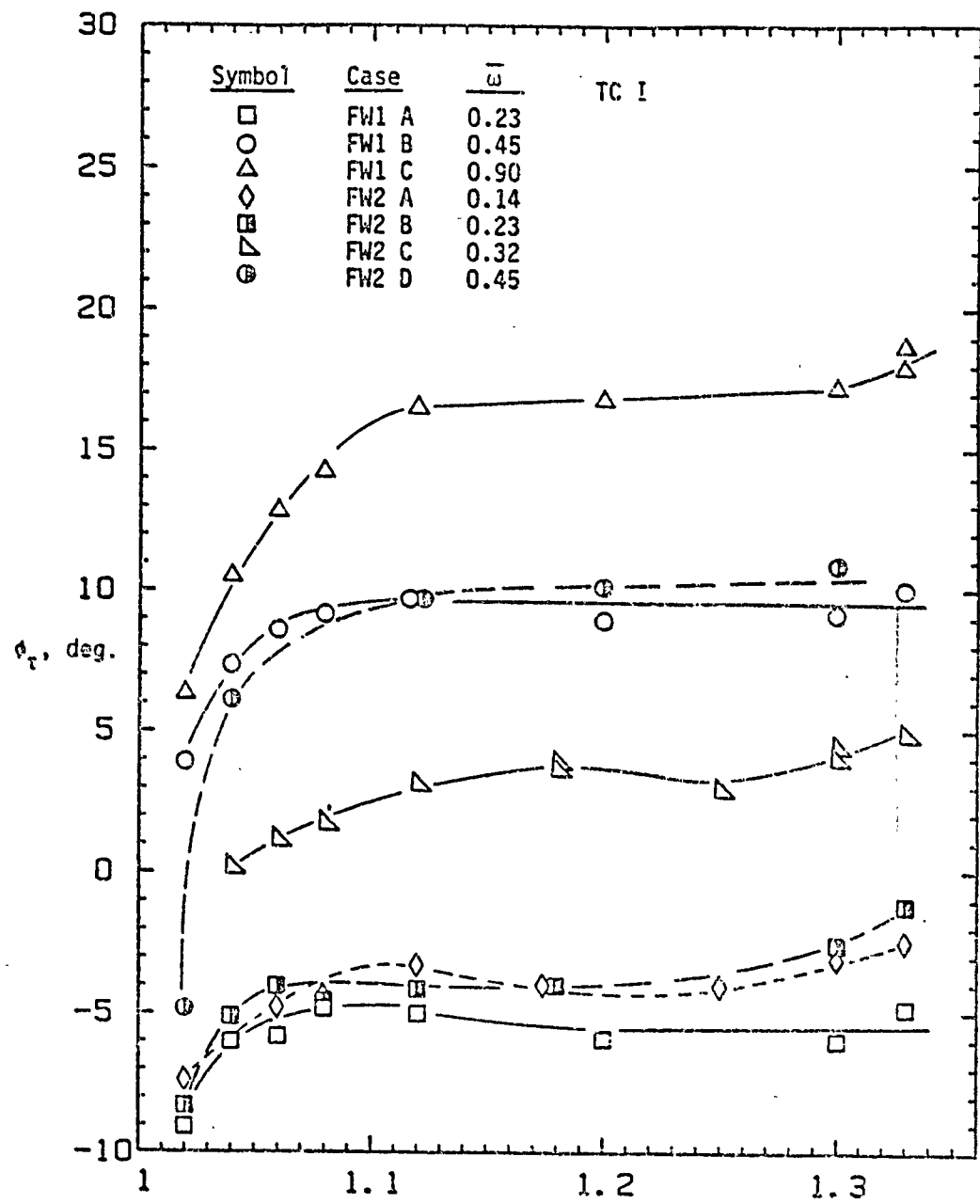
(d) Results for FW1 and FW2 gauges for TC I

FIGURE 20. (Continued)

A. Comparisons within the Experimental Results

There are several comparisons that can be made between results for the various gauges. A list of the comparisons performed is given below.

1. The repeatability of measuring ϕ_τ with the same gauge for different gauge installations.

2. Comparison between the same type of gauge.

3. Comparison between the two different types of gauges.

1. Comparison 1

The first comparison involves using the same gauge to check the repeatability of measuring ϕ_τ between various installations of the gauge. Installation refers to inserting the gauge in position for ϕ_τ measurements. Four comparisons were run using the PF2 gauge. A listing of these comparisons and the results are given in Table 8. The results show that there is some variation in measuring ϕ_τ for different installations of the gauge. This variation ranges from about 0 to 3 degrees.

2. Comparison 2

A comparison was made between gauges of the same type. In other words, the PF1 gauge was compared to the PF2 gauge and the same was done for the flush wire gauges. Table 9 lists the cases where a comparison is valid. For these cases, there was good agreement for similar types of gauges, with a range of about 1 to 3 degrees. This variation is within the difference obtained from Comparison 1 for repeatability.

TABLE 8. Comparison 1 - Checking for repeatability

CASE	TEST CONFIGURATION	f,Hz	$\bar{\omega}$	ϕ_τ,deg[a]	$\Delta\phi_\tau$,deg[b]
PF2 B	TC I	5.00	0.23	3.6	1.2
PF2 C	TC I	5.00	0.23	4.8	
PF2 E	TC I	10.00	0.45	13.3	2.9
PF2 F	TC I	10.00	0.45	16.2	
PF2 I	TC II	5.45	0.45	12.4	0
PF2 J	TC II	5.45	0.45	12.4	
PF2 N	TC II	20.00	1.66	24.9	0
PF2 O	TC II	20.00	20.00	24.9	

[a]At ORR = 1.30.

[b]$\Delta\phi_\tau$ is the difference between ϕ_τ for the cases being compared.

Thus, it can be assumed that gauges of the same type measure essentially the same ϕ_τ.

As previously noted, the PF1 gauge did not have the protective alumina coating over the film of platinum. The results given in Table 9 indicate that the coating does not affect the phase angle measured. This result probably could have been assumed since the gauges were not operating in a hostile environment and the coating is very thin.

3. Comparison 3

Now that the comparisons have been made between gauges of the same type, attention will be turned toward comparing the two different type

TABLE 9. Comparison 2 - Comparison between similar gauges under the same test conditions

CASE	TEST CONFIGURATION	f, Hz	$\bar{\omega}$	ϕ_τ, deg	$\Delta\phi_\tau$, deg
PF1 A	TC I	10.00	0.45	15.3	2.0
PF2 E	TC I	10.00	0.45	13.3	
PF1 A	TC I	10.00	0.45	15.3	0.9
PF2 F	TC I	10.00	0.45	16.2	
PF1 B	TC II	20.00	1.66	25.6	0.9
PF2 N	TC II	20.00	1.66	24.9	
PF1 B	TC II	20.00	1.66	25.8	0.9
PF2 O	TC II	20.00	1.66	24.9	
FW1 A	TC I	5.00	0.23	-5.5	3.0
FW2 B	TC I	5.00	0.23	-2.5	
FW1 B	TC I	10.00	0.45	9.5	0.9
FW2 D	TC I	10.00	0.45	10.4	

of gauges. Both types of gauges operate on the principle of heat transfer but differ in the kind of heating element and substrate used. The cases which may be compared are summarized in Table 10. It is evident from Table 10 and the results from the previous two comparisons that there is a larger variation in ϕ_τ measured by the two different types of gauges than among similar types. The variation between the flush wire gauges and the platinum film gauges ranged between approximately 1 to 8 degrees. Another noticeable aspect about the results in Table 10 is that for a given $\bar{\omega}$ the flush wire gauges measure

ϕ_τ consistently lower than the platinum film gauges. The angles are lower by approximately 1 to 8 degrees.

TABLE 10. Comparison 3 - Comparison between the two different type of gauges

CASE	TEST CONFIGURATION	f,Hz	$\bar{u}$	ϕ_τ,deg	$\Delta\phi_\tau$,deg[a]
PF2 A	TC I	3.00	0.14	-0.8	2.4
FW2 A	TC I	3.00	0.14	-3.2	
PF2 B	TC I	5.00	0.23	3.6	
PF2 C	TC I	5.00	0.23	4.8	5.2
FW1 A	TC I	5.00	0.23	-5.5	
FW2 B	TC I	5.00	0.23	-2.5	
PF2 D	TC I	7.00	0.32	10.8	6.5
FW2 C	TC I	7.00	0.32	4.3	
PF2 E	TC I	10.00	0.45	13.3	
PF2 F	TC I	10.00	0.45	16.2	
PF1 A	TC I	10.00	0.45	15.3	5.0
FW1 B	TC I	10.00	0.45	9.5	
FW2 D	TC I	10.00	0.45	10.4	
PF2 G	TC I	20.00	0.90	18.2	0.9
FW1 C	TC I	20.00	0.90	17.3	

[a] When more than one case has been run for the same type of gauge and run conditions the average of these cases is used to calculate $\Delta\phi_\tau$.

Comparisons will now be made between the experimental results for ϕ_τ and the numerical predictions.

B.   Comparison of Experimental Results and Numerical Predictions for ϕ_τ

The experimental results for ϕ_τ listed in Table 7 for high ORR have been plotted in Figure 21(a) through Figure 21(c) for test configurations TC I, TC II, and TC III, respectively. Also plotted in Figure 21 are the numerical results from Figure 16. It is clear from Figure 21 that the experimental results for ϕ_τ at a given $\bar{\omega}$ fall below the numerical predictions. This is true for all four gauges and all values of $\bar{\omega}$ at which data were taken. Figure 21(a) illustrates that ϕ_τ measured by the buried wire gauges are less than the ϕ_τ measurements of the platinum film gauges (as previously shown in Comparison 3).

To further illustrate the fact that all the experimental results for ϕ_τ are smaller than the numerical predictions, the difference between the experimental values $\phi_{\tau e}$ and the numerical predictions $\phi_{\tau n}$ in Figure 21 has been listed in Table 7 and are plotted in Figure 22. Figure 22 contains the results for all three test configurations and all four gauges. The buried wire gauges have a phase difference in the range of 10 to 18 degrees while the platinum film gauges have a phase difference in the range of 4 to 17 degrees.

There is some uncertainty in the phase difference $(\phi_{\tau n} - \phi_{\tau e})$. This comes from two sources. The first source is the uncertainty in the measurement of $\phi_{\tau e}$. As previously noted, this was estimated to be ± 1 degree. The second source is the uncertainty in determining the value of β for the numerical prediction of ϕ_τ. Based on experience with the profile matching procedure used it was estimated that the uncertainty in

TC I

Experimental results
for ϕ_τ at CRR = 1.30
(Table 7)

Symbol	Gauge
△	FH1
▣	FH2
▷	PF1
○	PF2

——— Numerical Prediction
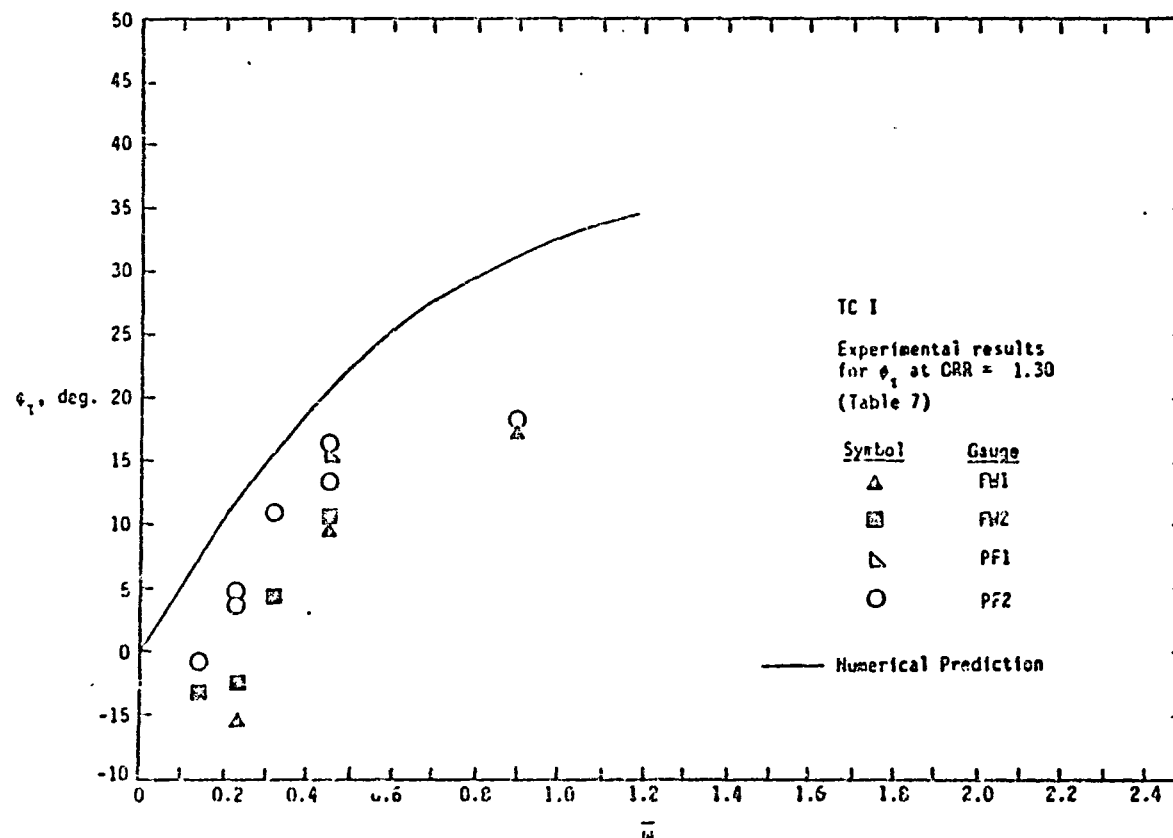
(a)   TC I

FIGURE 21.   Comparison of the experimental results for ϕ_τ with the
numerical predictions
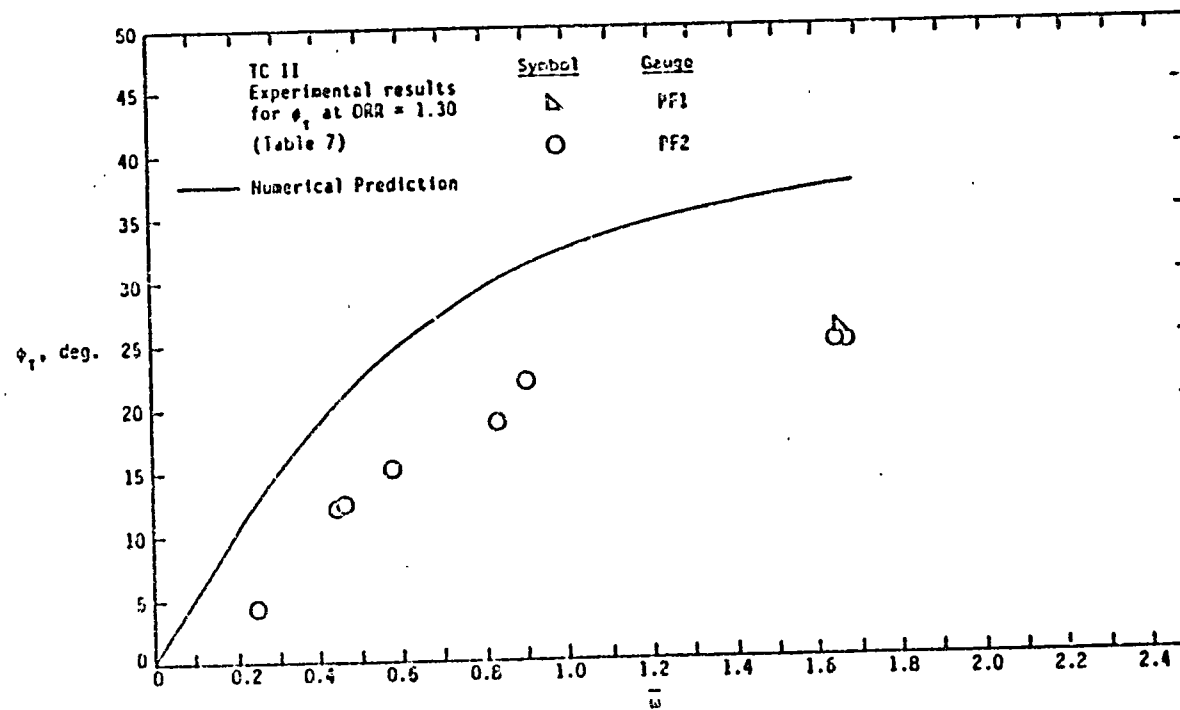
(b) TC II
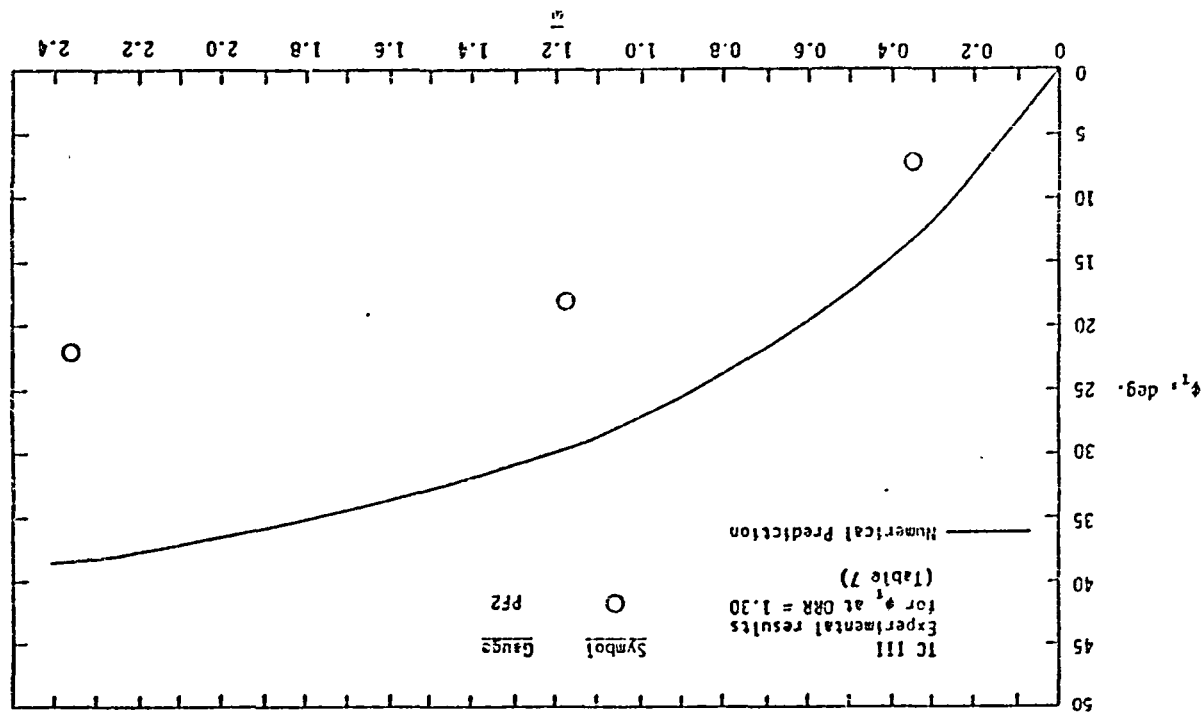
FIGURE 21. (Continued)

FIGURE 21. (Continued)

(c) TC III
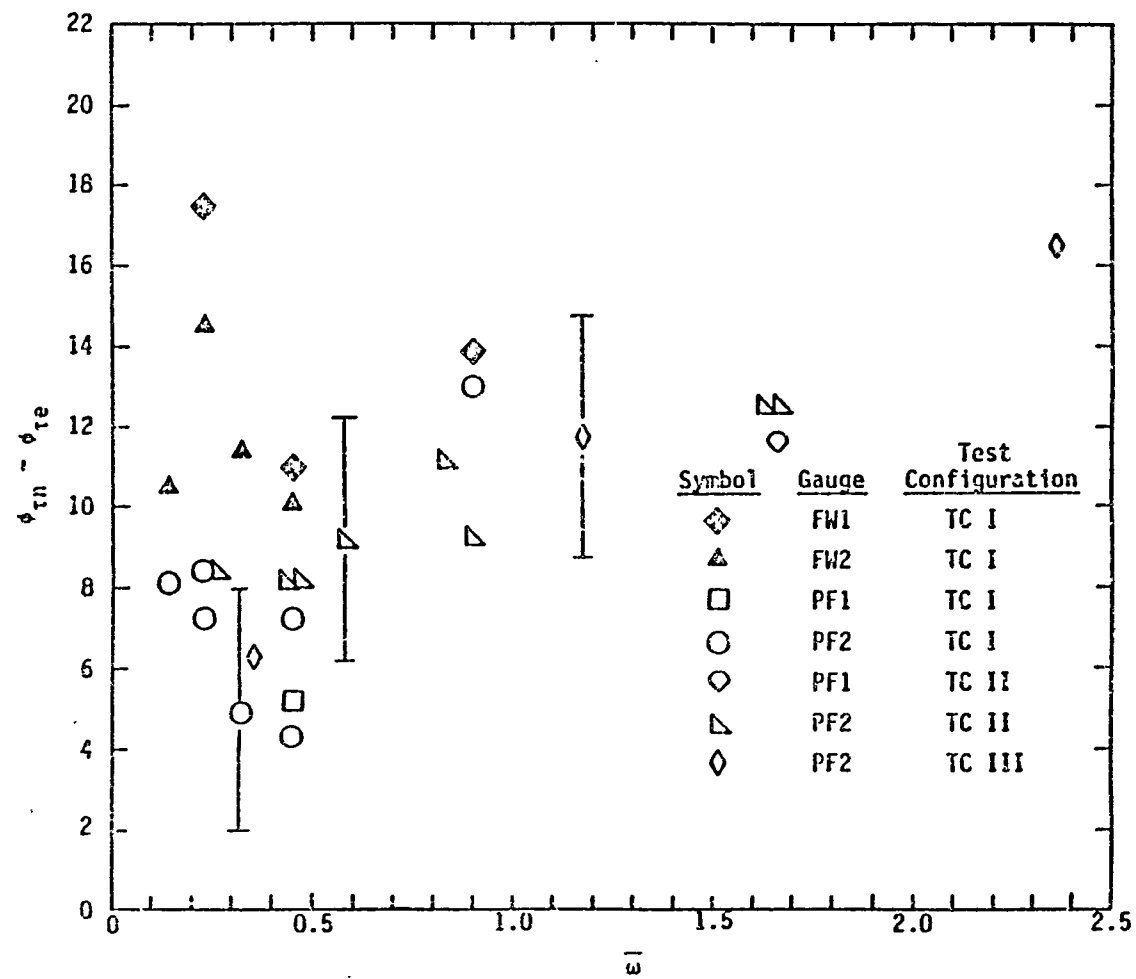
FIGURE 22. Difference between numerical predictions and experimental results for ϕ_r

β contributed an additional ± 2 degrees to the uncertainty in $\phi_{\tau n} - \phi_{\tau e}$.
Error bands of ± 3 degrees have been placed on several data points in
Figure 22.

An important observation from Figure 22 is that the results for the
platinum film gauges exhibit a trend toward larger values of $\phi_{\tau n} - \phi_{\tau e}$
with increasing $\bar{\omega}$. There are not enough experimental data for the flush
wire gauges to determine a trend. Figure 22 contains results for the
platinum film gauges for two values of β. There is no apparent
influence of β on $\phi_{\tau n} - \phi_{\tau e}$ for these gauges.

VIII. CONCLUSIONS

This study focused on an experimental investigation of the dynamic response of hot element gauges, because the ability of the gauges to correctly follow the wall shear stress fluctuations in a time dependent flow was under question. To test the gauges, the wall shear stress phase angle was measured in an oscillating laminar flow and then compared to numerical predictions. Before testing of the hot element gauges could be undertaken a study of the boundary layer was performed to verify that a laminar boundary layer was generated and that it was correctly modeled by the unsteady boundary layer computer code.

Two types of hot element gauges were tested. One had a thin platinum film deposited on a quartz substrate and the second type had a small diameter wire buried flush with a polystyrene substrate. Testing was done on a flat plate in a constant cross-sectional area test section. Two axial lengths along the plate and two mean freestream velocities were utilized along with a range of frequencies in order to produce a range of values for $\bar{\omega}$.

The results show that the repeatability of the hot element gauges is good. Several tests were repeated for different installations of the gauges. The variation was in the range of 3 degrees. This range is fairly small so it is concluded that the gauges will yield essentially the same ϕ_τ for similar runs.

A comparison was made between gauges of the same type and under the same run conditions. The variation in ϕ_τ measured for different gauges

but of the same type was approximately 3 degrees. Since the range for

the first comparison for repeatability was also 3 degrees it was

concluded that gauges of the same type measure the same value for ϕ_τ

within experimental error.

Comparison of the experimental results for ϕ_τ to the numerical

predictions show that both type of gauges measure a value for ϕ_τ lower

than the numerical predictions. The phase angle difference ($\phi_{\tau n} - \phi_{\tau e}$)

for the two type of gauges are also different. The buried wire gauges

have a phase difference in the range of 10 to 18 degrees while the thin

film gauges have a phase difference in the range of 4 to 17 degrees.

$\phi_{\tau n} - \phi_{\tau e}$ for the platinum film gauges tends to increase with $\bar{\omega}$. It is

not known why the two different types of gauges measure different ϕ_τ.

Apparently, the substrate material and heating element affect the gauge

response.

Since experimental and numerical results for ϕ_τ for the hot element

do not agree, it is concluded that the gauges do not faithfully follow

the shear stress fluctuations in oscillating laminar flow. This

seriously limits the usefulness of these gauges to measure surface shear

stress in time dependent laminar air flows. This also strongly suggests

that the gauges will not perform properly in unsteady turbulent air

flows.

The area of unsteady wall shear stress measurements is very

important, while at the same time very difficult. Based on the

understanding of the subject gained in this study, it appears that a

considerable amount of research possibly involving new measurement
techniques will be required before an accurate and reliable means of
measuring both the amplitude and phase relations for wall shear stress
is developed.

IX. BIBLIOGRAPHY

1. Cook, William J. _A Facility for Producing Periodic Subsonic Flows_. Iowa State University Engineering Research Institute Technical Report ISU-ERI-Ames-81117, 1980.

2. Cook, William J. and Yamaguchi, Yutaka _A Facility for Studying Turbulent Boundary Layers in Oscillating Flows_. Iowa State University Engineering Research Institute Technical Report ISU-ERI-Ames-82186, 1982.

3. Lighthill, M. J. "The Response of Laminar Skin Friction and Heat Transfer to Fluctuations in the Stream Velocity." _Proceedings of the Royal Society_, Series A, 224 (June 1954), 1-23.

4. Cousteix J., Houdeville, R. and Javelle, J. "Response of a Turbulent Boundary Layer to a Pulsation of the External Flow With and Without Adverse Pressure Gradient." _Unsteady Turbulent Shear Flows_. International Union of Theoretical and Applied Mechanics, Symposium, Toulouse, France, May 5-8, 1981. New York: Springer-Verlag, 1981.

5. Acharya, M., Bornstein, M. P. and Vokurka, V. "Development of a Floating Element for the Measurement of Surface Shear Stress." _AIAA Journal_, 23, no. 3 (1984), 410-415.

6. Kalumuck, Kenneth M. "A Theory for the Performance of Hot-Film Shear Stress Probes." Ph.D. Dissertation, Massachusetts Institute of Technology, 1983.

7. Ling, S. C. "Heat Transfer From a Small Isothermal Spanwise Strip on an Insulated Boundary." _Journal of Heat Transfer_, 85 (1963), 230-236.

8. Bellhouse, B. J. and Schultz, D. L. "Determination of Mean and Dynamic Skin Friction, Separation, and Transition in Low-Speed Flow With a Thin-Film Heated Element." _Journal of Fluid Mechanics_, 24 (1966), 379-400.

9. Kobashi, Y. and Hayakawa, M. "Structure of Turbulent Boundary Layer on an Oscillating Flat Plate." _Unsteady Turbulent Shear Flows_. International Union of Theoretical and Applied Mechanics, Symposium, Toulouse, France, May 5-8, 1981. New York: Springer-Verlag, 1981.

10. Ramaprian, B. R. and Tu, Shuen-Wei. "Study of Periodic Turbulent Pipe Flows." Iowa Institute of Hydraulic Research Report No. 238, 1982.

11. Personal communication with William J. Cook, Iowa State
    University regarding a study by Cook and F. K. Owen,
    Complere, Inc., Palo Alto, California, 1983.

12. Murphy, J. D. and Prenter, P. M. "A Hybrid Computing Scheme for
    Unsteady Turbulent Boundary Layers." Third Symposium on
    Turbulent Shear Flows, University of California, Davis,
    September 1981.

13. Karlsson, S. K. F. "An Unsteady Turbulent Boundary Layer."
    Journal of Fluid Mechanics, 5 (1959), 622-636.

14. Dewey, C. F. Jr. and Huber, P. W. "Measurement Methods for Fluid
    Shear Stress." Fluid Mechanics Laboratory Publications.
    Department of Mechanical Engineering, Massachusetts
    Institute of Technology, 1982.

15. Bellhouse, B. J. and Schultz, D. L. "The Measurement of
    Fluctuating Skin Friction in Air with Heated Thin-Film
    Gauges." Journal of Fluid Mechanics, 32, Part 4 (1968),
    675-680.

16. Lin, C. C. "Motion in the Boundary Layer With a Rapidly
    Oscillating External Flow." Ninth International Congress
    of Applied Mechanics, University of Brussels, Belgium,
    September, 1956.

17. Cebeci, T. and Carr, L. W. "A Computer Program for Calculating
    Laminar and Turbulent Boundary Layers for Two-Dimensional
    Time Dependent Flows." NASA TM-78470, March 1978.

18. Hill, P. G. and Stenning, A. H. "Laminar Boundary Layers in
    Oscillating Flows." Journal of Basic Engineering, 82
    (September 1960), 593-608.

19. White, Frank M. Fluid Mechanics. New York: McGraw-Hill, 1979.

20. White, Frank M. Viscous Fluid Flow. New York: McGraw-Hill,
    1974.

21. Murthy, V. S. and Rose, W. C. "Buried Wire Gage for Wall Shear
    Stress Measurements." AIAA 10th Aerodynamic Testing
    Conference, San Diego, California, April 19-21, 1978.

22. Kline, S. J. and McClintock, F. "Describing Uncertainties in
    Single-Sample Experiments." Mechanical Engineering, 75,
    no. 1, (Jan. 1953), 3-8.

X   APPENDIX A

TABLE 11. Tabulated results for case C1

$U_o = 16.35$ m/s, TC I		
y,in	η	u_o/U_o
0.0056	0.423	0.196
0.0114	0.869	0.389
0.0210	1.613	0.648
0.0278	2.133	0.787
0.0434	3.322	0.909
0.0472	3.619	0.964
0.0628	4.809	0.994
0.0744	5.701	0.996

TABLE 12. Tabulated results for case C2

$U_o = 16.49$ m/s, TC II		
y,in	η	u_o/U_o
0.0080	0.465	0.230
0.0130	0.751	0.364
0.0226	1.322	0.585
0.0326	1.893	0.745
0.0424	2.464	0.857
0.0522	3.035	0.931
0.0670	3.891	0.984
0.0866	5.033	1.000
0.1062	6.175	1.000

TABLE 13. Tabulated results for case A1

f = 10 Hz, $\bar{\omega}$ = 0.45, TC I
U_o = 16.58 m/s, U_1 = 2.295 m/s

y,in	η	u_o/U_o	u_1/U_1	ϕ_u,deg
0.0056	0.430	0.194	0.385	16.14
0.0114	0.879	0.391	0.688	9.00
0.0192	1.479	0.612	0.937	4.47
0.0260	2.004	0.760	1.067	1.64
0.0308	2.379	0.839	1.109	0.18
0.0366	2.829	0.908	1.124	0.21
0.0444	3.428	0.964	1.096	-0.15
0.0522	4.028	0.987	1.058	-0.32
0.0648	5.002	0.997	1.018	-0.71
0.0794	6.127	1.002	1.013	-0.22

TABLE 14. Tabulated results for case A2

f = 3 Hz, $\bar{\omega}$ = 0.25, TC II
U_o = 15.68 m/s, U_1 = 2.203 m/s

y,in	η	u_o/U_o	u_1/U_1	ϕ_u,deg
0.0076	0.431	0.211	0.401	7.029
0.0144	0.819	0.408	0.663	5.317
0.0212	1.207	0.562	0.847	3.368
0.0340	1.929	0.767	1.056	1.331
0.0486	2.761	0.913	1.122	0.670
0.0634	3.593	0.976	1.084	-1.103
0.0780	4.426	0.997	1.037	-0.164
0.0976	5.535	0.995	1.004	0.028
0.1172	6.645	0.993	0.996	-0.031

TABLE 15. Tabulated results for case A3

f = 5.58 Hz, $\bar{\omega}$ = 0.44, TC II
U_o = 16.77 m/s, U_1 = 2.241 m/s

y,in	η	u_o/U_c	u_1/U_1	ϕ_u,deg
0.0080	0.474	0.236	0.464	12.09
0.0130	0.759	0.369	0.651	8.92
0.0198	1.158	0.528	0.842	6.46
0.0296	1.729	0.704	1.025	2.71
0.0380	2.242	0.818	1.103	1.07
0.0456	2.698	0.884	1.108	0.05
0.0616	3.610	0.968	1.080	-0.27
0.0762	4.465	0.995	1.030	0.22
0.0908	5.321	0.999	1.007	0.55
0.1034	6.060	1.003	1.004	-0.56

TABLE 16. Tabulated results for case A4

f = 10 Hz, $\bar{\omega}$ = 0.78, TC II
U_o = 16.85 m/s, U_1 = 2.305 m/s

y,in	η	u_o/U_o	u_1/U_1	ϕ_u,deg
0.0080	0.476	0.233	0.509	16.67
0.0130	0.762	0.370	0.709	10.93
0.0198	1.163	0.526	0.895	6.65
0.0276	1.620	0.669	1.035	3.01
0.0372	2.192	0.798	1.123	-0.09
0.0490	2.879	0.903	1.127	-1.18
0.0656	3.851	0.971	1.066	-C.95
0.0810	4.766	0.990	1.017	-0.35
0.0976	5.739	0.993	0.998	-C.01

TABLE 17. Tabulated results for case A5

	$f = 15$ Hz, $\bar{\omega} = 1.18$, TC II $U_o = 16.73$ m/s, $U_1 = 2.469$ m/s			
y,in	η	u_o/U_o	u_1/U_1	ϕ_u,deg
0.0082	0.480	0.237	0.579	15.83
0.0082	0.479	0.257	0.575	15.91
0.0130	0.766	0.377	0.786	9.48
0.0150	0.882	0.421	0.842	7.77
0.0210	1.227	0.552	0.988	3.30
0.0278	1.630	0.673	1.095	-0.52
0.0356	2.090	0.782	1.151	-2.86
0.0456	2.665	0.882	1.152	-4.22
0.0572	3.355	0.953	1.102	-3.39
0.0720	4.217	0.993	1.039	-1.61
0.0868	5.080	1.002	1.005	-0.11
0.1014	5.942	1.000	0.998	-0.19
0.1114	6.517	0.998	0.986	-0.16

TABLE 18. Tabulated results for case A6

f = 20 Hz, $\bar{\omega}$ = 1.59, TC II
U_o = 16.60 m/s, U_1 = 2.698 m/s

y,in	η	u_o/U_o	u_1/U_1	ϕ_u,deg
0.0078	0.457	0.231	0.552	16.47
0.0126	0.739	0.369	0.744	7.77
0.0194	1.134	0.527	0.921	0.09
0.2823	1.642	0.682	1.055	-5.52
0.0368	2.150	0.801	1.108	-8.18
0.0484	2.827	0.910	1.106	-7.50
0.0640	3.730	0.977	1.054	-4.00
0.0804	4.689	0.997	1.014	-1.27
0.0968	5.649	1.000	1.002	0.12
0.1142	6.664	1.000	1.000	0.27

TABLE 19. Tabulated results for case B1

f = 3 Hz, $\bar{\omega}$ = 0.34, TC III
U_o = 11.69 m/s, U_1 = 2.227 m/s

y,in	η	u_o/U_o	u_1/U_1	ϕ_u,deg
0.0066	0.327	0.175	0.341	12.46
0.0134	0.663	0.351	0.605	8.80
0.0232	1.142	0.551	0.837	4.34
0.0330	1.622	0.700	0.984	2.51
0.0448	2.197	0.830	1.070	0.57
0.0586	2.868	0.924	1.099	0.33
0.0732	3.587	0.972	1.062	-0.77
0.0918	4.498	0.995	1.026	-1.11
0.1114	5.457	1.003	1.011	0.73
0.1310	6.416	0.999	1.000	0.40

TABLE 20. Tabulated results for case B2

	f = 10 Hz, $\bar{\omega}$ = 1.19, TC III U_o = 11.08 m/s, U_1 = 2.197 m/s			
y,in	η	u_o/U_o	u_1/U_1	ϕ_u,deg
.00661	0.315	0.174	0.473	20.86
0.0126	0.599	0.319	0.723	13.30
0.0184	0.878	0.450	0.878	7.96
0.0262	1.253	0.589	1.014	3.27
0.0370	1.768	0.735	1.120	-1.19
0.0478	2.284	0.842	1.143	-2.62
0.0626	2.987	0.933	1.119	-3.50
0.0774	3.689	0.975	1.060	-2.71
0.0970	4.627	0.993	1.011	-0.65
0.1168	5.564	0.999	1.001	0.03
0.1364	6.501	1.001	1.000	0.01

TABLE 21. Tabulated results for case B3

	f = 20 Hz, $\bar{\omega}$ = 2.38, TC III U_o = 11.11 m/s, U_1 = 2.442 m/s			
y,in	η	u_o/U_o	u_1/U_1	ϕ_u,deg
0.0064	0.308	0.176	0.576	24.49
0.0132	0.631	0.341	0.809	11.92
0.0210	1.001	0.500	0.927	3.17
0.0286	1.370	0.629	1.011	-3.00
0.0374	1.786	0.745	1.044	-7.24
0.0490	2.340	0.857	1.035	-8.29
0.0616	2.940	0.929	1.020	-6.43
0.0810	3.863	0.982	1.007	-2.38
0.1004	4.787	1.001	0.995	0.34
0.1196	5.710	0.993	1.004	0.25
0.1342	6.403	0.999	0.991	1.02

XI   APPENDIX B

TABLE 22. Tabulated results for case PF1 A

ORR	ϕ_τ, deg.
1.041	11.2
1.082	14.6
1.125	15.2

TABLE 23. Tabulated results for case PF1 B

ORR	ϕ_τ, deg.
1.02	8.6
1.04	17.7
1.06	20.9
1.08	23.3
1.12	24.9
1.18	25.9
1.25	26.4
1.30	25.7
1.33	25.6

TABLE 24. Tabulated results for case PF2 A

ORR	ϕ_τ, deg.
1.02	-2.1
1.04	-0.1
1.06	0.2
1.08	0.2
1.12	0.8
1.18	-0.7
1.25	-1.5
1.30	-0.7
1.33	-0.7

TABLE 25. Tabulated results for case PF2 B

ORR	ϕ_τ, deg.
1.02	4.0
1.04	3.3
1.06	5.2
1.08	4.0
1.12	3.4
1.20	2.9
1.30	3.8
1.33	3.6

TABLE 26. Tabulated results for case PF2 C

ORR	ϕ_τ, deg.
1.04	3.7
1.08	4.4
1.18	4.6
1.25	5.0
1.30	4.8

TABLE 27. Tabulated results for case PF2 D

ORR	ϕ_τ, deg.
1.02	5.1
1.04	9.8
1.06	10.7
1.08	11.5
1.12	12.1
1.18	10.8
1.25	10.7
1.30	10.8
1.33	10.5

TABLE 28. Tabulated results for case PF2 E

ORR	ϕ_τ, deg.
1.02	5.0
1.04	11.7
1.06	12.3
1.08	13.2
1.12	13.6
1.20	13.7
1.30	13.0
1.33	13.0

TABLE 29. Tabulated results for case PF2 F

ORR	ϕ_τ, deg.
1.04	13.5
1.08	16.1
1.18	16.3
1.25	16.2
1.33	15.8

TABLE 30. Tabulated results for case PF2 G

ORR	ϕ_τ, deg.
1.02	5.6
1.04	12.0
1.06	15.0
1.08	16.3
1.08	16.3
1.12	17.3
1.20	18.4
1.30	18.1
1.33	18.1

TABLE 31. Tabulated results for case PF2 H

ORR	ϕ_τ, deg.
1.02	2.8
1.04	5.4
1.06	.5.5
1.08	5.2
1.12	5.0
1.18	5.0
1.25	4.9
1.30	4.1
1.33	4.2

TABLE 32. Tabulated results for case PF2 I

ORR	ϕ_τ, deg.
1.02	8.5
1.04	11.9
1.06	.11.7
1.08	12.8
1.12	12.3
1.18	12.1
1.25	12.7
1.30	12.6
1.33	11.7

TABLE 33. Tabulated results for case PF2 J

ORR	ϕ_τ, deg.
1.02	10.4
1.04	11.7
1.06	.11.7
1.08	12.4
1.12	12.6
1.18	13.1
1.24	12.4
1.28	11.9
1.30	12.5
1.33	12.3

TABLE 34. Tabulated results for case PF2 K

ORR	ϕ_{τ},deg.
1.02	8.7
1.04	13.3
1.06	14.8
1.08	15.4
1.12	16.4
1.18	15.7
1.25	14.9
1.30	15.2
1.30	15.4
1.33	15.3

TABLE 35. Tabulated results for case PF2 L

ORR	ϕ_{τ},deg.
1.02	10.2
1.03	13.9
1.04	15.9
1.06	17.7
1.08	18.5
1.12	19.0
1.18	18.9
1.22	19.1
1.28	19.1
1.33	18.5

TABLE 36. Tabulated results for case PF2 M

ORR	ϕ_τ, deg.
1.02	13.0
1.04	19.1
1.06	21.1
1.08	22.0
1.12	22.2
1.18	22.7
1.25	22.0
1.30	21.7
1.33	21.8

TABLE 37. Tabulated results for case PF2 N

ORR	ϕ_τ, deg.
1.02	6.0
1.04	17.4
1.06	21.3
1.08	22.7
1.12	24.4
1.18	25.1
1.25	24.9
1.30	24.9
1.33	24.9

TABLE 38. Tabulated results for case PF2 O

ORR	ϕ_τ, deg.
1.02	5.2
1.03	12.7
1.04	16.3
1.06	20.3
1.08	22.3
1.12	24.1
1.16	24.7
1.22	25.1
1.28	24.8
1.33	24.2

TABLE 39. Tabulated results for case PF2 P

ORR	ϕ_τ, deg.
1.02	6.9
1.04	7.8
1.06	8.4
1.08	8.5
1.08	8.3
1.12	8.9
1.18	8.6
1.25	7.6
1.30	6.9
1.33	6.3

TABLE 40. Tabulated results for case PF2 Q

ORR	ϕ_τ, deg.
1.02	7.9
1.04	14.9
1.06	17.4
1.08	18.2
1.12	18.5
1.18	18.2
1.25	17.6
1.30	17.7
1.33	18.0

TABLE 41. Tabulated results for case PF2 R

ORR	ϕ_τ, deg.
1.02	3.6
1.04	14.5
1.06	18.1
1.08	19.6
1.12	21.0
1.18	21.7
1.25	22.3
1.30	21.6
1.33	22.1

TABLE 42. Tabulated results for case FW1 A

ORR	ϕ_τ, deg.
1.02	-9.1
1.04	-6.0
1.06	-5.8
1.08	-4.8
1.12	-5.0
1.20	-5.9
1.30	-6.0
1.33	-4.8

TABLE 43. Tabulated results for case FW1 B

ORR	ϕ_τ, deg.
1.02	3.8
1.04	7.3
1.06	8.6
1.08	9.1
1.12	9.7
1.20	8.9
1.30	9.1
1.33	10.0

TABLE 44. Tabulated results for case FW1 C

ORR	ϕ_τ, deg.
1.02	6.3
1.04	10.5
1.06	12.8
1.08	14.2
1.12	16.5
1.20	16.8
1.30	17.2
1.33	18.0
1.33	18.7

TABLE 45. Tabulated results for case FW2 A

ORR	ϕ_τ, deg.
1.02	-7.4
1.04	-4.8
1.06	-4.8
1.08	-4.4
1.12	-3.3
1.18	-4.0
1.25	-4.1
1.30	-3.1
1.33	-2.4

TABLE 46. Tabulated results for case FW2 B

ORR	ϕ_τ,deg.
1.02	-8.3
1.04	-5.1
1.06	-4.0
1.08	-4.5
1.12	-4.1
1.18	-4.1
1.25	-4.0
1.30	-2.5
1.33	-1.2

TABLE 47. Tabulated results for case FW2 C

ORR	ϕ_τ,deg.
1.02	-4 9
1.04	0.1
1.06	1.1
1.08	1.7
1.12	3.1
1.18	3.8
1.18	3.6
1.25	2.9
1.30	4.4
1.30	4.0
1.33	4.9

TABLE 48. Tabulated results for case FW2 D

ORR	ϕ_τ, deg.
1.04	6.0
1.12	9.7
1.20	10.0
1.30	10.8

XII   APPENDIX C

This section estimates the uncertainty in the η ($\eta = y\sqrt{U_o/\nu x}$)
measurements using the method of Kline and McClintock [22]. The
uncertainty interval λ_R, in the results is given by

$$\lambda_R = \left[\left(\frac{\partial R}{\partial \vartheta_1} \lambda_1\right)^2 + \left(\frac{\partial R}{\partial \vartheta_2} \lambda_2\right)^2 + \ldots \left(\frac{\partial R}{\partial \vartheta_n} \lambda_n\right)^2 \right]^{1/2} \qquad (12)$$

where R is .the result of a single-sample experiment, ϑ is an independent
variable, n is the total number of independent variables, and λ_i is the
uncertainty interval for each variable. Since the uncertainty interval
for each variable is generally not statistically known, it is necessary
to estimate it to specified odds. The values of λ_i to be presented have
been estimated based on 10 to 1 odds. Since ν is a function of pressure
and temperature an uncertainty analysis was carried out for ν. The
uncertainty interval for ν was very small so it was excluded from the
following calculations for λ_η. The results in Table 49 are for a y
location close to the plate surface.

From the calculation in Table 49 $\lambda_\eta = 0.069$. The value of η
computed using the values in Table 49 is 0.691. Thus, for a typical run
for a y location near the plate surface

$$\eta = 0.691 \pm 0.069$$

TABLE 49. Uncertainty analysis for η

Variable	Nominal Value	λ_i	$\partial\eta/\partial\vartheta_i$	$(\lambda_i \partial\eta/\partial\vartheta_i)^2$
x	0.21 m	$\pm$ 0.25 cm	-1.671	1.745×10^{-4}
U_o	16.7 m/s	$\pm$ 0.25 m/s	0.021	2.759×10^{-5}
y	0.03 cm	$\pm$ 0.003 cm	23.025	4.771×10^{-3}
				4.816×10^{-3}

$$\lambda_\eta = \pm (4.816 \times 10^{-3})^{1/2}$$

$$\lambda_\eta = \pm 0.069$$

End of Document